9-17-2019 3:30 PM

Ni and Fe isotope fractionation during weathering and the formation of Ni laterite ore deposits in the Philippines

Congxi Zhu, *The University of Western Ontario*

© Congxi Zhu 2019

Abstract

Weathering processes on Ni-rich ultramafic rocks in tropical areas produce laterites that become exploitable for Ni mining. To better understand these processes, samples were collected stratigraphically with water samples from several Ni mines in the Philippines and studied for Ni and Fe isotope compositions. This study found that Ni isotope fractionation takes place during the formation of Ni-enriched minerals (goethite), when light Ni isotopes are preferentially incorporated into new minerals formed, leaving heavy Ni isotopes in groundwater. The $\Delta^{60}Ni_{\text{Limonite-Bedrock}}$ is up to -0.19 ± 0.32‰. Even though Fe is partitioned with redox state change during these reactions, Fe isotope fractionation was not detected within our analytical precision. In complement, iron meteorites were analyzed for their $\delta^{57}Fe$ to shed light on the origin of Lovina ataxite. This study supports other reports that Lovina has instead a terrestrial origin.

Keywords

Summary for Lay Audience

Nickel (Ni) is a metal that is widely used, most notably in the alloy industry. Lateritic ore deposits host 60% to 70% of the world Ni resources, and they provide 40% of world Ni production. Nickel is very enriched in ultramafic rocks, and weathering processes on ultramafic rocks in tropical areas lead to high grade concentrations of Ni, which becomes valuable for the mining industry. To better understand laterite formation and assess the potential of Ni isotopes as tracers of weathering processes, Ni and Fe isotope compositions of bedrock, saprolite, limonite, topsoil, and mineralization collected stratigraphically, as well as water samples from four Ni mines in Zambales and Palawan ophiolite zones in the Philippines, were studied. Nickel is primarily hosted in olivine and pyroxene before being leached into the groundwater. This study found that the replacement of Fe and Mg in the Fe- and Mg-oxide minerals by Ni might be the controlling mechanisms of Ni fractionation during weathering processes in tropical area laterite profiles. Light Ni isotopes are preferentially incorporated into the newly-formed minerals, leaving heavy Ni isotopes in water. The heavy Ni-rich groundwater can result to heavy Ni isotope compositions in mineralized samples. In addition, Fe isotopes show very little isotopic variation among rocks existing in five different zones, which might be a result of low mobilization of Fe^{3+}. In complement, iron meteorites were analyzed for their Fe isotopic composition to shed new light on the origin of the Lovina ataxite ungrouped meteorite. Based on its chemical composition and heavy Fe isotope composition compared to iron meteorites analyzed so far, this study supports previous findings that Lovina has a terrestrial origin but remains enigmatic in its formation process.

Co-Authorship Statement

Dr. Christian Schardt (University of Minnesota in Duluth) collected and provided the samples and XRD analyses. Dr. Blair Gibson carried out the XRF analyses. Dr. Laura Wasylenki and Dr. Shuijiong Wang (Indiana University) both carried out the measurement of Ni isotopic ratios. Dr. Dominique Weis and Kathy Gordon (Pacific Centre for Isotopic and Geochemical Research at the University of British Columbia) aided in the measurement of Fe isotopic ratios which I attended. The elemental compositions of water samples were analyzed by Actlabs.

Acknowledgments

Table of Contents

List of Tables

List of Figures

<h1>Chapter 1</h1>

<h1>1   Introduction</h1>

Nickel (Ni) is an important metal in modern society. It is widely used in the stainless steel, alloy and battery industries (Ratié et al. 2016). Nickel in the form of metal, ferronickel and oxides enhances the corrosion resistance and strength of a number of alloys. About 88% of Ni produced in 2018 was used for stainless steel industry and in the alloy industry for nonferrous alloys and superalloys (US Geological Survey. 2019). Among all Ni applications, superalloys for aerospace applications cannot have Ni replaced by another metal (Roskill Information Services 1981). Demand for Ni has increased as modern industry developed. The world Ni production increased from 1,400,000 t to 2,100,000 t over the last 16 years (Figure 1) (US Geological Survey. 2019).
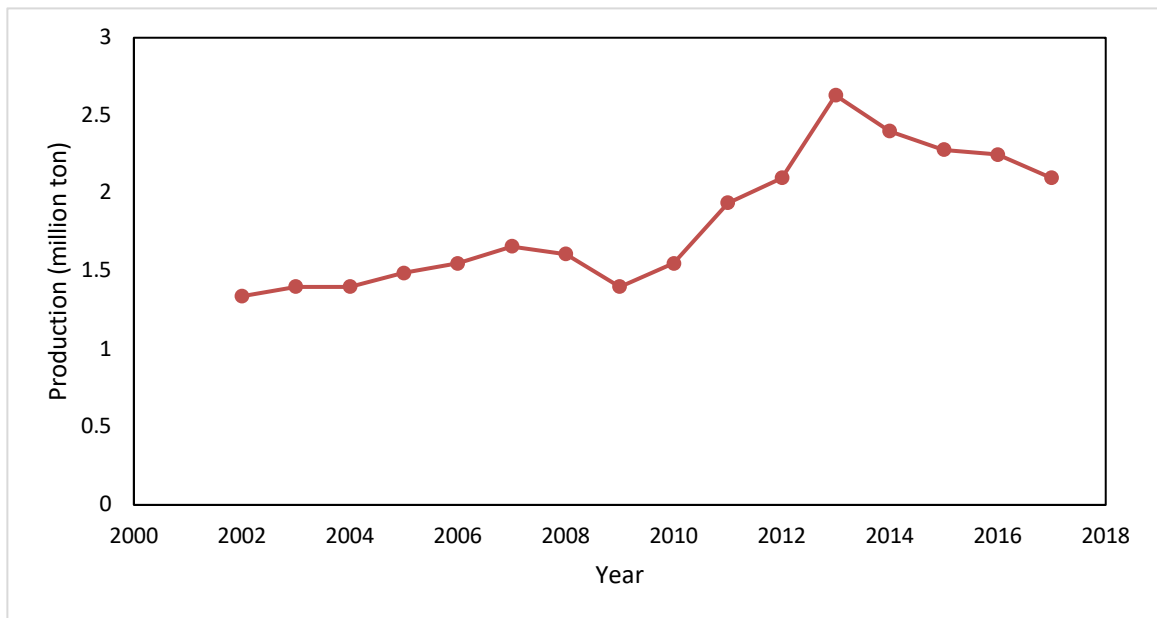
Figure 1 World Ni production since 2002 (US Geological Survey 2019).

1.1 Nickel as a resource

There are two main types of nickel ores, sulfide and lateritic. The most common Ni-rich mineral in sulfide ores is pentlandite, $(Ni,Fe)_9S_8$. It has been suggested that most sulfide Ni deposits were derived from sulfide-undersaturated magmas (Arndt et al. 2005; Keays 1995; Naldrett 2004), and sulfide-rich sediments provided sulfur to reach sulfide saturation (Bekker et al. 2009; Lesher 1989; Lesher and Burnham 2001; Naldrett 2013). The solubility of sulfide in silicate magma is very low, typically < 2000 ppm (Smythe et al. 2017; Lesher 2019). Once the magma reaches sulfide saturation, the sulfide will start to segregate. Cooling also contributes to reaching sulfide saturation in magmas. Once dissolved sulfide reaches saturation in a silicate magma, sulfide droplets become immiscible. Thus, sulfide liquid might crystalize and concentrate siderophile and chalcophile elements including Ni, Cu, Co and PGE. These metals are then redistributed as a result of later post-consolidation processes (Rajamani and Naldrett, 1978).
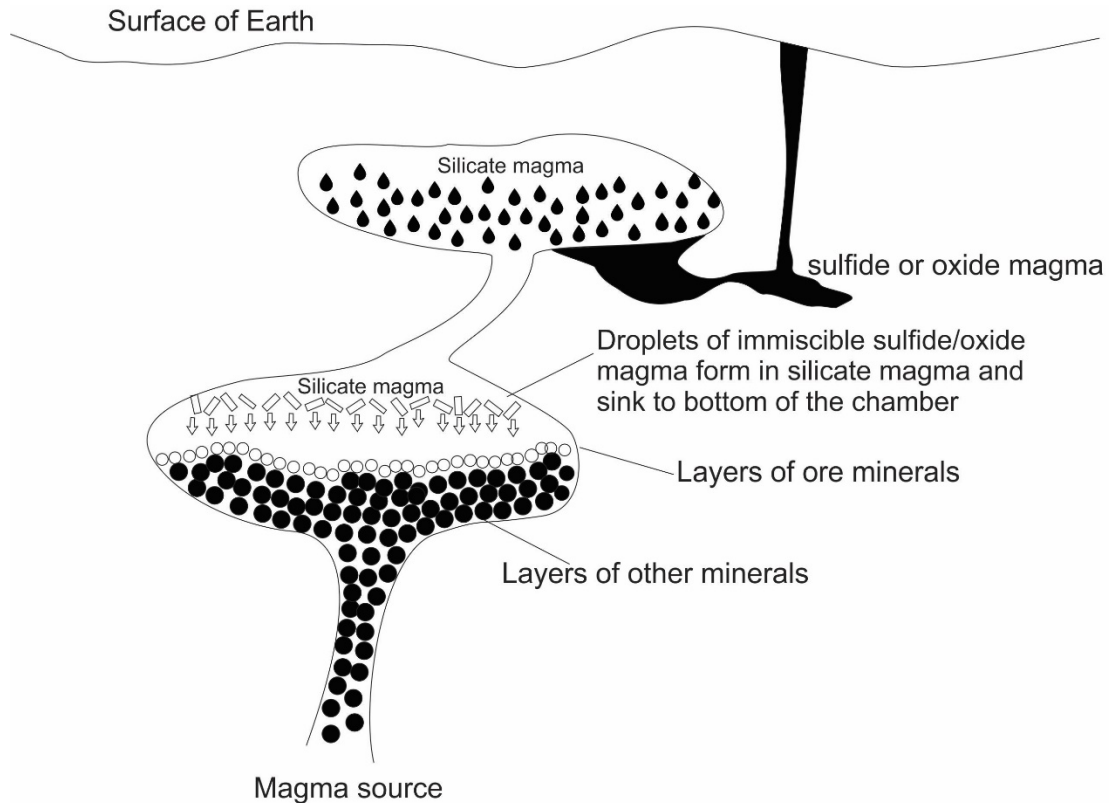
Figure 2 The diagram of magmatic mineral deposits forming processes (modified from (Kesler et al. 2015).

Lateritic ores host 60% to 70% of the world nickel resources, but they only constitute 40% of world nickel production (Butt and Cluzel 2013; Elias 2002). Laterites are the weathering products of surface ultramafic rocks in tropical areas. Ultramafic rocks are enriched in Ni which exists in olivine, spinel, amphibole, serpentine and pentlandite (Ratié et al. 2015). Nickel is released by weathering processes from these minerals to groundwater. Then, new Ni-enriched minerals form in other parts of the same profile under tropical climate. To solve the problem of diminishing reserves of sulfide Ni ores and increasing global demand, lateritic Ni ore mining technology must be further developed.

In this study, twenty-two solid samples through four stratigraphic sections (Table 1) and eight river water (Table 9) samples were collected in the Zambales Ophiolite Zone and Palawan Ophiolite Zone of the Philippines. The Philippines is a major Ni producer in the

world. This project investigated lateritic Ni-mineralization that occurred in the Palawan Ophiolite Complex (POC) and Zambales Ophiolite Complex (ZOC), which are located in the southern Palawan and western Luzon islands, Philippines, respectively. Since this study had access to stratigraphic samples, fractionation processes along the laterization processes could be studied with the aim of understanding the natural Ni cycle system, which would be useful knowledge for improving strategy and methods for Ni mineral exploration and mining.

Deposit/Location	Sample	Type
G-pit Gunitalunan (Palawan Ophiolite Zone)	G-M-1	laterite + mineralization
	G-M-2	bedrock + mineralization
	G-M-2A	bedrock + mineralization
	G-L-3	laterite
	G-L-4A	laterite
	G-L-4B	laterite
M-pit Mangingidong (Palawan Ophiolite Zone)	M-M-5	bedrock + mineralization
	M-L-6	laterite
	M-B-7	bedrock
	M-L-8	laterite
	PH-W-2	water
Eramen Minerals (Zambales Ophiolite Zone)	E-B-9	bedrock
	E-L-10A	laterite
	E-S-10B	saprolite
	E-B-10C	bedrock
	E-B-10D	bedrock
Benguet Mining Corp. (Zambales Ophiolite Zone)	B-S-11A	saprolite
	B-S-11B	saprolite
	B-SO-12	soil
	B-L-13	laterite
	B-S-14	saprolite
	B-B-15A	bedrock
	B-B-15B	bedrock

Table 1 A summary of sample locations and types. The first part of the sample name (G, M, E, B) indicates location (G-pit Gunitalunan, M-pit Mangingidong, Eramen Mineral, Benguet Mining Corp). The second part (M, SO, L, S, B) indicates sample type: mineralization, soil, laterite, saprolite, and bedrock respectively.

1.2 Geological Setting of the Palawan Ophiolite Complex and Zambales Ophiolite Complex
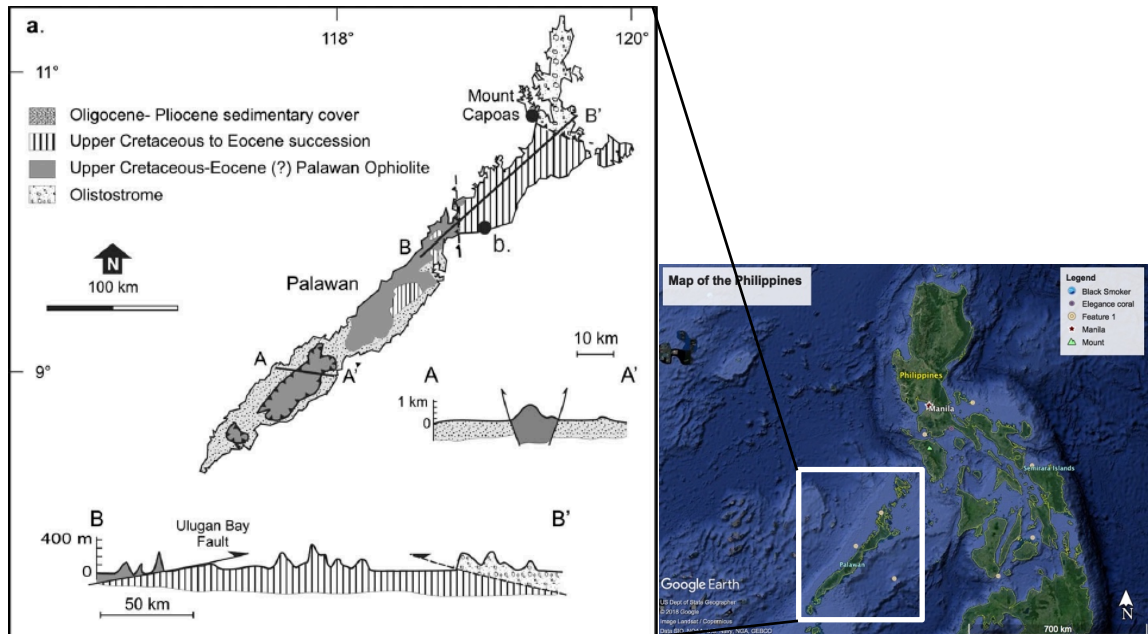
Figure 3 Location of Palawan Island, Philippines (Yumul et al. 2009).

Palawan island is located in the western part of the Philippines (Figure 3). It belongs to the Luzon region, lies between Sulu Sea and South China Sea, and is northeast-southwest trending. Holloway (1982) studied the origin of Palawan Ophiolite Complex (POC) and proposed that the North Palawan Block and the South Palawan Block have different origins. The North Palawan Block formed in the Late Paleozoic to the Mid Mesozoic and moved southeast from mainland Asia (Holloway 1982). It consists of continent-derived sedimentary rocks, such as quartz-rich sandstone, pebbly mudstones, turbidites and mudstones, and metamorphic rocks, such as schists, phyllites, quartzites and slates (Yumul et al. 2008). The South Palawan Block was formed during the Late Mesozoic to Paleozoic (Holloway 1982). It is made up of ocean-derived rocks including the POC (Yumul et al. 2008) where the research samples for this study were collected. The Palawan Ophiolite Complex has been formed from Late Cretaceous to Eocene according to the radiolarians extracted from the chert (Raschka et al. 1985). The Palawan Ophiolite Complex is a supra-subduction zone which experienced a high degree of partial melting (Yumul et al. 2008). Encarnación and Mukasa (1997) carried out U-Pb dating of

monazite from Palawan Island. [206]Pb and [207]Pb are daughter isotopes of [238]U and [235]U, respectively. By measuring U and Pb isotope ratios and knowing the half-life, the result indicates a mean age of 13.4 ± 0.4 Ma for crystallization of granite. The authors attributed this age to the post-rifting, non-collisional magmatism stage. The mainland Philippines migrated northwest as the result of the subduction along the Asian continental margin, and Palawan subsequently collided with northwest moving Philippines (Yumul et al. 2008). A period between 16 to 20 Ma for the major collision between Palawan Island and Philippine mobile belt was further proposed (Yumul et al. 2009).
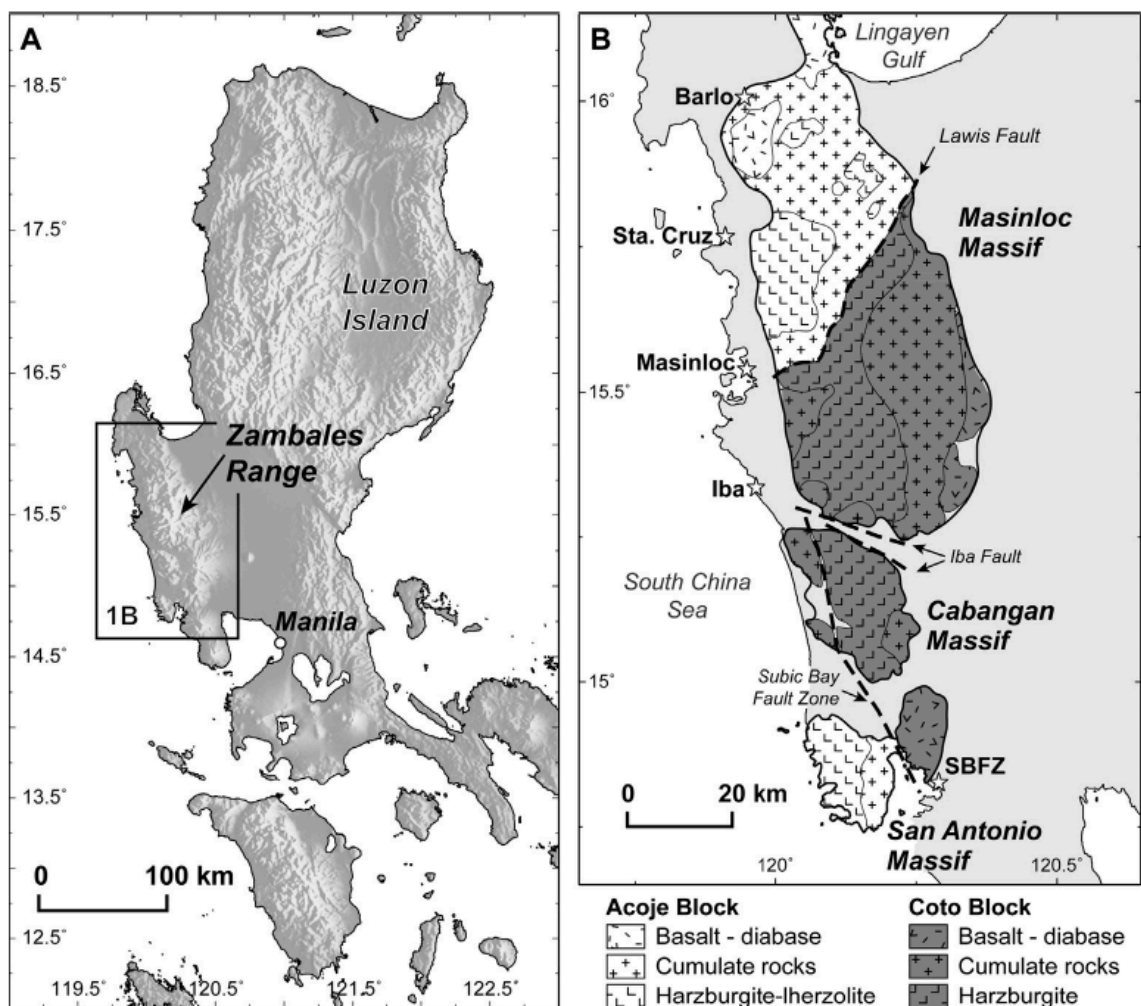
Figure 4 Location of Zambales Ophiolite Complex (Dimalanta et al. 2015 modified from Yumul et al. 1998).

The Zambales Ophiolite Complex (ZOC) is located in western Luzon island, the Philippines, and trends north-south (Figure 4). There are two distinct parts of the ZOC, the Acoje and Coto blocks. The Acoje Block is located in the northwest part of the ZOC, and the Coto Block is located in the southeastern area. Rossman et al. (1989) studied the detailed geological settings of the ZOC and proposed that it was a tectonically combination of an island arc and a back-arc. The Acoje Block is made up of arc-tholeiite series rocks from intra-island arcs, while the Coto block consists of back-arc basin rock series (Hawkins and Evans 1983, Rossman et al. 1989). A marine basaltic flow is the uppermost rock. Under the uppermost basaltic flow, there is a diabasic dyke, followed by a tabular gabbro unit underneath. In the Coto block, the tabular gabbro is made up of olivine gabbro. In the Acoje Block, the tabular gabbro is made up of norite. A 250-meter-thick serpentinized dunitic zone is underlying the gabbro unit. Afterwards, there is a 1 km deep harzburgite zone where chromite deposits occur. Gneissic banding usually shows in the harzburgite zone, chromite deposits, dunite zone and many gabbro zones. The ZOC was exposed because of uplifting of the island arc. It formed during the late Eocene, and the uplifting took place during the middle to late Oligocene. Erosion occurred during the early Miocene and exposed the ultramafic rocks (Schweller et al. 1983).

The parent rocks of weathered profiles are peridotites and gabbros. There are two divisions of the gabbroic rocks in the ZOC, norite and olivine gabbros. Norite appears in the Acoje Block and the top of Dalayap Hill in the Coto Block, while olivine gabbro makes up the remaining gabbro in the Coto Block (Rossman et al. 1989). According to Rossman et al. (1989), the interlayering of serpentine and gabbro at the lower contact of the olivine gabbro and the serpentinized dunite is due to the differential movement during the uplifting process. A previous Ni project conducted at Palawan island reported that the lateritic Ni-Co mineralization was developed in the residual regolith overlying serpentinized cumulates of the Mt. Beaufort ultramafic rocks (Fourie et al. 2009). Their target areas for Ni mining activities are moderated by topographic relief with abundant faulting or fracturing because laterite profiles are easily developed there and water, which is the main requirement for ore formation, can penetrate (Fourie et al. 2009).

1.3 Laterization process

Nickel laterites host most of the Ni resources in the world. They are weathering products of surface ultramafic rocks in humid conditions. Some minerals are not stable when interacting with water, breaking down into new stable minerals. Ni-rich laterite formed because of laterization of Mg-rich or ultramafic rocks, and the primary Ni concentration of the rock ranges from 0.2 to 0.4% (Golightly 1981). The Ni mining project conducted at Palawan island reports that the laterization process enriched Ni concentrations from 0.2% to 0.25% for bedrock and from 0.5% to 3% Ni in laterites (Fourie et al. 2009). Although Ni contents of ultramafic rocks are higher than other rocks, laterization can still enrich Ni contents by 3 to 30 times (Elias 2002). The parent rocks of Ni laterite usually are dunite, harzburgite or peridotite, and to a lesser extent, komatiite or layered mafic to ultramafic intrusive rocks in cratonic platform environments (Brand et al. 1998). Cratonic setting is where laterites are formed in the komatiites and the ultramafic phases of layered mafic complex of any period from Archaean to the Paleozoic. Another tectonic setting where laterites are usually found is accretionary settings. The Philippines is a typical example of accretionary settings. It is associated with a tectonically active area, including oceanic and continental plate boundaries and collision zones. The formation of such laterites can range from Cretaceous to the late Tertiary (Brand et al. 1998).

Initially, weathering processes occurred at the contacts between minerals and boundaries of fractures and faults. At this stage, most of the rocks were still bedrocks. As time passed, a larger portion of primary rocks were altered but the primary rock fabric was still preserved. Afterwards, most of the minerals would become altered, and the primary rock fabric disappeared. The vertical diagram of a laterite profile (Figure 5) shows the laterization process result. The lowest zone represents the beginning stage, while the uppermost zone represents the most altered stage. At the top of the profile, a nodular fabric zone called ferricrete or iron crust develops in the limonite zone, which is an indurated crust as the nodules coalesce and harden. During the laterization processes, olivine, pyroxene and serpentine are broken down and Mg, Ni, Mn and Co are leached to groundwater. Groundwater brings leached elements to a deeper zone. New minerals, such as goethite and smectite, form and are enriched in Ni contents (Elias 2002). Iron and Al

are less soluble, so they are enriched in zones which are shallower than the Ni- and Mg-enriched zones (Brand et al. 1998). In the vertical laterite profile, Fe and Al-rich secondary minerals form in the upper limonite zone, while Ni-rich phyllosilicate minerals form in the underlying saprolite or clay zones (Elias 2002; Fan and Gerson 2011). Different laterite formations may show variations in their laterite profiles because there are several factors controlling the profile development, including climate, topography, drainage, tectonics, parent rocks and geology structure (Elias 2002; Dalvi et al. 2004).
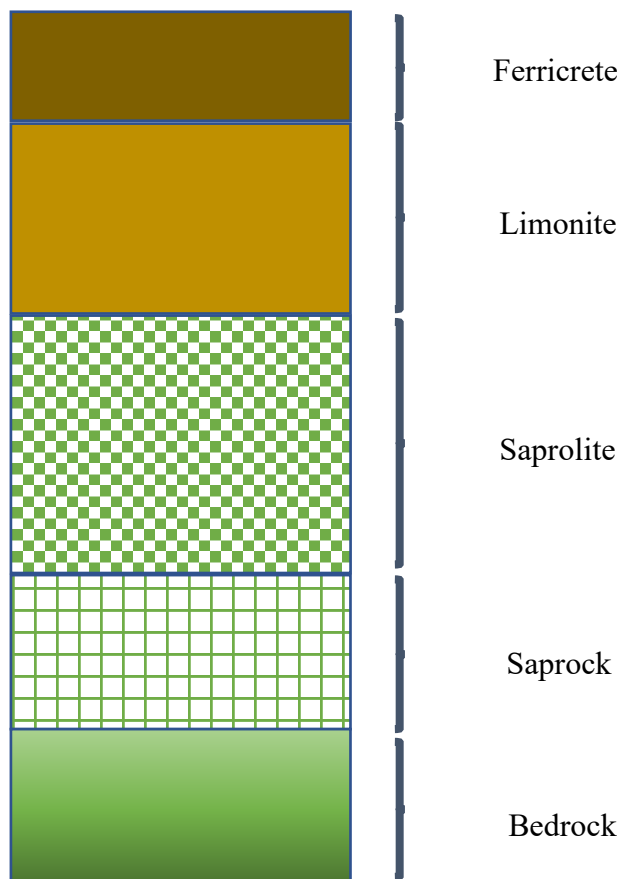
Figure 5 A schematic diagram of laterite profile (Modified from Elias 2002).

Despite the variations in the controlling factors, there are three types of laterite, including oxide laterite, clay laterite and silicate laterite (Brand et al. 1998). Oxide laterite, which is the most common final product of laterization of ultramafic rocks, is made up of Fe

oxides and Mn oxides in the upper zone in the vertical laterite profile (Elias 2002; Fan and Gerson 2011). Nickel exists in goethite and Mn-oxides in oxide laterite (Manceau et al. 2000). Primary minerals, such as olivine, serpentine and pyroxene, break down because of the presence of groundwater. Nearly all of the Mg and most of the Si are leached to groundwater. Ferric iron and ferrous iron are also released to groundwater but re-precipitated as Fe hydroxides.

Mineral development during laterization (Butt and Cluzel 2013):

The breakdown of olivine to form serpentine is described by the reaction

$$3 \ Mg_2SiO_4 + SiO_2 \ (aq) + 4 \ H_2O \ \rightleftharpoons 2 \ Mg_3Si_2O_5(OH)_4$$
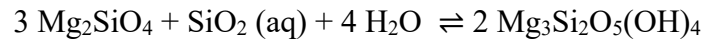
During serpentinization, the Fe_2SiO_4 component of olivine is oxidized to form goethite:

$$Fe_2SiO_4 + 2 \ H_2O \rightleftharpoons 2 \ Fe(O)(OH) + SiO_2 \ (aq) + H_2$$
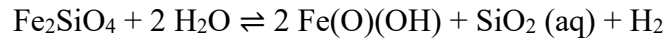
Serpentine breaks down to saponite, leaching Mg to water:

$$2 \ Mg_3Si_2O_5(OH)_4 \rightleftharpoons Mg_3Si_4O_{10}(OH)_2 + 3 \ MgO \ (aq) + 3 \ H_2O$$
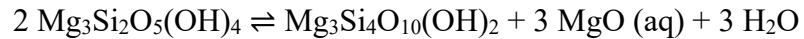
The $Fe_3Si_2O_5(OH)_4$ component of serpentine forms goethite, again by oxidation:

$$2 \ Fe_3Si_2O_5(OH)_4 + 2 \ H_2O \rightleftharpoons 6 \ Fe(O)(OH) + 4 \ SiO_2 \ (aq) + 3 \ H_2$$

As Ni and Co are released as well, they become incorporated into the newly formed Fe hydroxides (Elias 2002). Formation of clay laterite occurs in less severe weathering condition than oxides laterite. It also preferentially happens in places with low topographic relief and restricted groundwater movement (Golightly 1981). Nickel incorporates into nontronite instead of Fe hydroxides (Brand et al. 1998). Silica is not leached as in oxides but used to form nontronite and opaline or chalcedonic nodules in the clay (Elias 2002). The third category, silicate laterite, forms at deeper zones than oxide laterite under a long period of weathering processes, slow uplifting processes and a low water table environment (Fan and Gerson 2011; Golightly 1981; Elias 2002). Nickel contents are enriched in the saprolite zone, which consists of secondary serpentine,

goethite, smectite and garnierite (Elias 2002). Pelletier (1996) reported that the secondary serpentine could contain up to 5% Ni, and Ni contents could be up to 20% in garnierite. Most of the currently mined Ni ores are silicate laterites.

Leaching and Ni-exchange reactions:

Ni-adsorbed goethite releases Ni to groundwater:

$$Fe(O)(OH)(Ni)(OH)_2 + 2\ H^+ \rightleftharpoons Fe(O)(OH) + Ni^{2+} + 2\ H_2O.$$
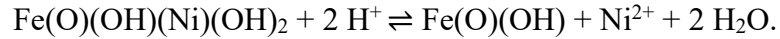
Serpentine and saponite incorporate Ni, which can be described by exchange reactions:

$$Mg_3Si_2O_5(OH)_4 + 3\ Ni^{2+} \rightleftharpoons Ni_3Si_2O_5(OH)_4 + 3\ Mg^{2+}$$
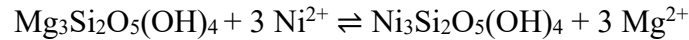
(Ni reacts with lizardite during uplift), and

$$Mg_3Si_4O_{10}(OH)_2 + 3\ Ni^{2+} \rightleftharpoons Ni_3Si_4O_{10}(OH)_2 + 3\ Mg^{2+},$$
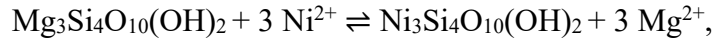
where $Mg_3Si_2O_5(OH)_4$ and $Ni_3Si_2O_5(OH)_4$ are the Mg and Ni components of the serpentine phase, and $Mg_3Si_4O_{10}(OH)_2$ and $Ni_3Si_4O_{10}(OH)_2$ are the Mg- and Ni-rich components of the saponite phase.

Since little research has been done on Ni isotope fractionation processes in tropical regions, limited information is available about the mineralogical form and isotope behaviour of Ni in the mining area in the Philippines. This research aims to study Ni content and Ni isotopic compositions in stratigraphic order of deposit materials to trace the Ni pathway. Firstly, this study aims to characterize the selected materials for their mineralogy and elemental geochemistry for ZOC and POC formations. Then, analyses were carried out to obtain the isotopic compositions of Ni from stratigraphic materials to waters and establish the isotopic fractionation factors based on their Ni isotopic compositions. The long-term goals of this research are to obtain a knowledge of how Ni fractionation along with the weathering processes taking place in lateritic Ni ores in tropical areas. This work may have further application to identify weathering processes in planetary materials such as soil samples which are planned to be brought back from Mars

in the near future. Finding new ways to identify aqueous weathering processes is particularly important when the mineralogy may not always be an evidence for these.

1.4   On the notation of Ni isotope

Nickel is the 28th element in the periodic table. There are five natural and stable Ni isotopes, ^{58}Ni, ^{60}Ni, ^{61}Ni, ^{62}Ni and ^{64}Ni. Among these naturally stable Ni isotopes, ^{58}Ni is the most abundant one with 68.08% abundance. ^{60}Ni, ^{61}Ni, ^{62}Ni and ^{64}Ni have abundances of 26.22%, 1.14%, 3.64% and 0.93%, respectively (Gramlich et al. 1989).

Ni isotope fractionation is reported as isotopic ratio (R), fractionation factor (α), delta value (δ) and big delta (Δ). Isotopic ratio (R) is the ratio of the abundance of the heavy to light isotope.

$Ni^{60/58}$ = Atomic abundance of ^{60}Ni/ Atomic abundance of ^{58}Ni.

Instead of using the absolute isotopic composition of a sample which varies between laboratories because of instrumental mass bias, isotopic compositions are normalized to an international standard measurement measured in-between samples (standard bracketing). The Ni isotopic composition is expressed as a delta notation (δ) which is the deviation of the sample from the standard average composition (measured before and after the sample) in per mil (‰):

$\delta^{60/58}Ni$ (‰) = $(R^{60/58}_{x}/R^{60/58}_{std}-1) \times 1000$, where x is the unknown sample, std is an abbreviation for isotopic standard reference material. For Ni isotopic composition analysis, the National Institute of Standards and Technology Standard Reference Material (NIST SRM) 986 Ni metal is used as standard material for inter-laboratory comparisons. Isotopic data can thus be compared between laboratories. A positive delta value means that the ratio of heavy isotope to light isotope of the unknown sample is higher than the ratio in the standard material (NIST SRM 986). The sample has thus a heavier isotopic composition. A negative delta value means that the ratio of the heavy isotope to light isotope of the unknown sample is lower than the ratio in the standard material. The sample has thus a lighter isotopic composition.

Fractionation factor (α) is the ratio of the isotopic compositions of any two substances. It can be expressed as:

α (Ni)metal-silicate$^{60/58}$ = R$_{metal}$$^{60/58}$/R$_{silicate}$$^{60/58}$.

The fractionation factor measures the fractionation between two phases such as metal and silicate.

Big delta (Δ) is the difference of delta values of two substances. It generally has linear relationship with fractionation factor, so it can be used to approximate the value of fractionation factor. Big delta can be expressed as:

ΔNi$_{metal-silicate}$= $\delta^{60/58}$Ni$_{metal}$ - $\delta^{60/58}$Ni$_{silicate}$

Δ_{a-b} =1000$ln\alpha_{a-b}$

In order to study Ni isotope compositions of rock and water samples, Gueguen et al. (2013) developed a two-stage ion-exchange chromatography column chemistry procedure adapted from previous works by Cameron et al. (2009) and Cook et al. (2007). They reported Ni isotopic compositions relative to NIST SRM 986 of a variety of geological materials, including a lot of geological reference materials, mafic and ultramafic rocks, and ore deposits. Partial melting and fractional crystallization processes have shown to produce little influence on Ni isotope fractionation. As most of the terrestrial Ni (>99%) resides in the mantle, average compositions of mantle rocks thus define the Ni isotope composition of the BSE (See Section 1.5.2 for further details). Based on the value of common basalts and mantle-derived rocks, Gueguen et al. (2013) determined a δ^{60}Ni of Bulk Silicate Earth (BSE) of 0.05 ± 0.05‰. However, Cameron et al. (2009), Steele et al. (2011) and Gall et al. (2017) suggested a heavier Ni isotope composition for BSE, but each suggesting a relatively homogeneous mantle Ni isotopic composition (δ^{60}Ni$_{BSE}$ =0.23 ± 0.06‰ reported by Gall et al. 2017; δ^{60}Ni$_{BSE}$ =0.18 ± 0.04‰ reported by Steele et al. 2011; δ^{60}Ni$_{BSE}$ =0.15 ± 0.24‰ reported by Cameron et al. 2009).

1.5   Ni isotopic fractionation

1.5.1   Ni isotope fractionation in laterite profile

So far, limited research has been conducted studying the Ni isotopic fractionation
processes in laterite profiles which is a major form of Ni ores. One study conducted by
Ratié et al. (2015) investigated the Ni isotope fractionation effects during tropical
weathering of ultramafic rocks in Brazil, and another study by Spivak-Birndorf (2018)
studied the driving mechanism of Ni isotopic variation along lateritic profile in the
Philippines.

Ratié et al. (2015) investigated Ni isotope fractionation during tropical weathering of
ultramafic rocks. They investigated Ni isotope signature as an environmental tracer rather
than its pathway from initial high temperature magma to the final weathering products.
Their research is based on samples collected from an ultramafic complex of Barro Alto in
the Goias State, Brazil. The Brazilian bedrock, soil and ore deposit samples showed
increasing Ni contents, and they have Ni concentrations ranging from 0.22% to 0.28%,
1.27% to 1.94%, 1.68% to 2.56% respectively (Ratié et al. 2015). Nickel concentrations
in ultramafic rocks and soils developed from ultramafic rocks are elevated. Bedrock
samples display isotopic compositions which average at δ^{60}Ni of 0.28 ± 0.08‰, ore
samples display δ^{60}Ni from −0.60‰ to 0.30‰, and soil samples display δ^{60}Ni from −0.19
to −0.02‰ (Ratié et al. 2015). Their results suggest that there is a depletion in heavy Ni
isotopes in solid phases during weathering processes (Δ^{60}Ni$_{Soil-Bedrock}$ = −0.47‰) (Ratié et
al. 2015). Low δ^{60}Ni values may be associated with Ni isotope fractionation during
mineralization and weathering processes. Thus, nickel isotopic fractionation may help
trace Ni deposits and become helpful for Ni exploration.

Spivak-Birndorf (2018) discussed several potential mechanisms controlling Ni
fractionation processes of lateritic profiles. To verify if the Ni leaching process caused Ni
isotope fractionation, Spivak-Birndorf (2018) carried out a leaching experiment. Their
experiment results indicated that the primary release of Ni from bedrock to solution did
not result in Ni isotopic variation. It is the incorporation and sorption of Ni to Fe-oxides
which have the most effects on Ni isotopic fractionation. However, they did not study the

Ni isotopic variations within a vertical pathway behavior along the laterite profile. The goals of this thesis are to investigate the Ni isotope fractionation behaviour from the ultramafic bedrocks to final weathering products to better understand laterization process in tropical areas.

The reported Ni isotopic variations observed in lateritic profiles draws attention to low temperature fractionation effects for Ni. So far, a δ^{60}Ni range of crust sourced materials from -0.1‰ to 0.3‰ and range of mantle sourced materials from 0.08‰ to 0.28‰ have been reported (Cameron et al. 2009; Gall et al. 2012; Gall et al. 2013; Gall et al. 2017; Steele et al. 2011; Gueguen et al. 2013; Chernonozhkin et al. 2015; Estrade et al. 2015; Ratié et al. 2015). However; Cameron and Vance (2014) reported a heavier and wider range of river water δ^{60}Ni, which is from 0.29‰ to 1.34‰. Their samples were collected close to banks worldwide, including Amazon, Brahmaputra, Nile, Chang Jiang, Ottawa and Volga. The up to 1‰ difference indicates the existence of a complex Ni transformation system. Seawater δ^{60}Ni value is even higher than river water, with the average δ^{60}Ni of 1.44 ± 0.15‰ (two standard deviations, 2SD). The reason for the difference between seawater and river water Ni isotopic composition is either heavier input or lighter output than river, but it remains unknown so far. The fact that heavy isotopes are enriched in the dissolved phase while light isotope are enriched in the solid phase does not only exist in the Ni system, but also other transitional metals systems, including Cu and Mo (Archer and Vance 2008; Vance et al. 2008). The fractionation could happen in a number of natural processes, such as leaching from primary minerals to groundwater, sorption to minerals, or co-precipitation with secondary minerals. Wasylenki et al. (2015) did the experiments to study the Ni isotopic fractionation during the adsorption and co-precipitation from dissolved phase and they observed an average $\Delta^{60/58}$Ni$_{\text{dissolved-sorbed}}$ = +0.35 ± 0.10‰ (1 SD). It is suggested that light Ni isotopes were preferentially incorporated into solid phase, while leaving heavy Ni isotopes in the dissolved phase. In addition, Ni isotopic fractionation during the leaching process is indistinguishable according to the experiments carried out by Spivak-Birndorf et al. (2018). Thus, it is necessary to study other weathering processes controlling Ni fractionation system under low temperature environments.

1.5.2   Ni isotope fractionation in igneous systems

While Ni mines are of large value, little attention has been paid to Ni isotopic fractionation in magmatic systems as a tool to understand their formation. Redox related changes can result in large mass-dependent isotope fractionations (Elliott and Steele 2017). Mass-dependent Ni isotope fractionation in igneous systems received little attention so far maybe because of the lack of redox variability of Ni in silicates on Earth. Larger Ni isotopic variations than those found in terrestrial mantle rocks have recently been reported in lunar samples which confirms that redox conditions are another important parameter to understand the partitioning behaviour of Ni during high-temperature igneous processes (Sanders et al., 2018).

Most research that has been carried out to study the Ni isotope chemistry under high temperature has been focused on mantle rocks (Cameron et al., 2009; Steele et al., 2011; Gall et al., 2012; 2013; Gueguen et al., 2013; Chernonozhkin et al., 2015; Estrade et al., 2015; Ratié et al., 2015). Earth's upper mantle hosts more than 99% of the Earth's Ni (Gall et al. 2017). Nickel concentration of the mantle is up to 1960 ppm (McDonough and Sun 1995). The most recent estimate of $\delta^{60}Ni_{mantle}$ is 0.23 ± 0.06‰ (2SD), which also defines the Ni isotope composition of Bulk Silicate Earth (BSE) (Gall et al. 2017).

The difference between $\delta^{60}Ni$ value of BSE and chondrite meteorite is insignificant (Figure 6), which indicates a hypothesis that little Ni mass-dependent isotope fractionation occurred during core formation (Cameron et al., 2009; Chernonozhkin et al., 2015; Gall et al. 2017).

Small but resolvable variations in Ni isotope composition variations have been recently identified between mantle rocks, and explained by variations of mantle mineral compositions and their modal abundances (e.g. olivine, orthopyroxene, clinopyroxene, garnet) (Gall et al. 2017). Ultramafic rocks range from 0.15 ± 0.07‰ to 0.36 ± 0.08‰, with olivine-rich showing lighter isotope compositions than komatiite, lherzolite and pyroxenite samples (Gall et al. 2017). Experimental constraints would be helpful in interpreting the fractionation effects found in various igneous mantle minerals as they

may be associated with Ni coordination and its electronic bonding environment and vary with redox, pressure and temperature conditions.

The Ni isotope variation in terrestrial samples may also be explained by recycling of basaltic materials throughout subduction, leaving light Ni as a signature. Thus, investigating the Ni fractionation processes in surface systems such as laterites is important to provide constraints on the Ni behavior from mantle rocks to surface reservoirs to better understand the mantle-crust system. Our study will provide compositions of reservoirs which can be used for tracing and interpreting the variation found in igneous rocks formed within different tectonic environments.
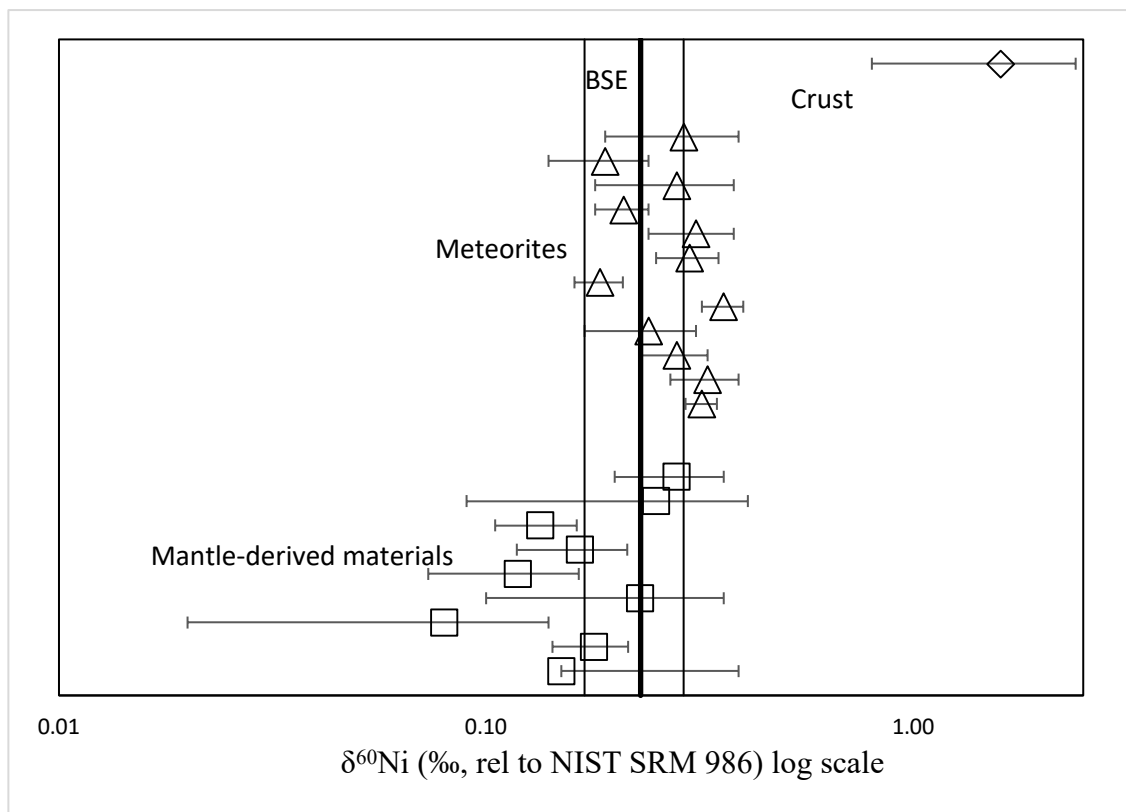
Figure 6 Summary of δ^{60}Ni values from literature studies (Cameron et al., 2009; Steele et al., 2011; Steele et al., 2012; Gall et al., 2013; 2017; Gueguen et al., 2013; Chernonozhkin et al., 2015; Estrade et al., 2015; Ratié et al., 2015).

Ni sulfides are a major form of Ni ores, and they are formed by sulfide saturation from assimilation of country rocks. The cooling process of komatiite magma can assimilate 10% of a country rock which contains 6% sulfur could result in 0.6% increase of sulfur content in the magma (Huppert et al. 1984). One example is that Ni sulfide ores are found at the base of magmatic flow at Kambalda, Western Australia (Huppert et al. 1984). The sulfide is mainly from the assimilation of country rocks while Ni is mainly from the mantle-derived magma. Enrichment in sulfur makes the sulfur liquid immiscible, so it extracts Ni from the magma, and finally segregates. Significant Ni isotopic fractionation occurs when Ni-sulfides form from a silicate magma (Elliot and Steele 2017). Nickel sulfides from komatiitic magmas have a wide range of $\delta^{60}Ni$, which is from -0.3 to -1‰ (Steele et al. 2011; Gueguen et al. 2013; Hofmann et al. 2014). The Ni isotopic compositions of magmatic sulfides are relatively light compared with other lithology, e.g. organic-rich marine sediments ($\delta^{60}Ni$ = 0.20‰ to 2.50‰) (Gueguen et al. 2013; Hofmann et al. 2014; Estrade et al. 2015). Thus, it is inferred that the interaction of ultramafic magma and country rock sulfides will result in low $\delta^{60}Ni$ (Bleeker and Macerk 1996).

Constraints on equilibrium Ni isotope fractionation between metal and silicate at high temperature reported the equilibrium fractionation of Ni isotopes between metal and talc under magmatic temperature and pressure ($\Delta^{62/58}Ni_{metal-silicate}=0.25\pm0.02 \times 10^{6}/T^{2}$) (Lazar et al. 2012). Light Ni is preferentially concentrated in metal rather than silicate (Lazar et al. 2012). However, few studies have focused on Ni isotope composition of igneous, metamorphic rocks, and ore deposits.

Among all the rock types, Gall et al. (2013) suggested that ferromanganese crusts which were represented by samples collected from several ocean basins have significantly heavier Ni isotope compositions than other rocks reported so far. In addition, the difference between Ni isotope compositions of crusts from Atlantic, Indian and Pacific Oceans is very little. The constant Ni isotope compositions of oceanic crusts indicated that the heavy Ni isotope composition in the ocean is derived from input from continental weathering and also from hydrothermal fluids.

1.5.3   Ni stable isotope application in the petroleum industry

There are a number of elements in crude oil, including major elements (e.g. carbon, hydrogen, minor elements (e.g. nitrogen, sulfur) and trace elements (e.g. vanadium, nickel, iron, molybdenum) (Ventura et al. 2015). Recently, studies have shown that trace metal concentration and isotopic composition are of great value in petroleum system exploration. For example, trace metals concentration and isotopic data in crude oil could reveal geochemical features of the source rocks and are useful in oil-source correlation, which determines if a genetic relationship between oil reservation and source rock exists (Dreyfus et al. 2005). Nowadays, studies on V and Ni, which are the most abundant trace metal elements in crude oil, have been done, and they are used in correlation and fingerprinting, and to determine redox conditions during source rock deposition (Archer et al., 2012). Ventura et al. (2015) displayed a narrow Ni isotope signature of crude oils which is similar to Ni isotope compositions of carbonaceous shales. Combined with V and Mo stable isotope systems, Ni could be developed as a tool to study the formation and preservation of oil source rocks.

1.6   Fe isotopic fractionation

Iron is a transition metal and is the 26th element in the periodic table. Iron has the electronic configuration $[Ar]3d^6 4s^2$, and it has four stable isotopes, ^{54}Fe, ^{56}Fe, ^{57}Fe and ^{58}Fe with natural atom abundance of 5.8%, 91.8%, 2.1% and 0.3% respectively (Berglund and Wieser 2011). Iron is the fourth most abundant element in the continental crust and presents high abundance in laterite profile. Figure 7 shows $\delta^{56}Fe$ values of some terrestrial samples and meteorites. Redox reaction and soil formation processes can result in Fe isotope fractionation; thus, iron is extremely important in understanding laterization processes (Chapman et al. 2009; Li et al. 2017).
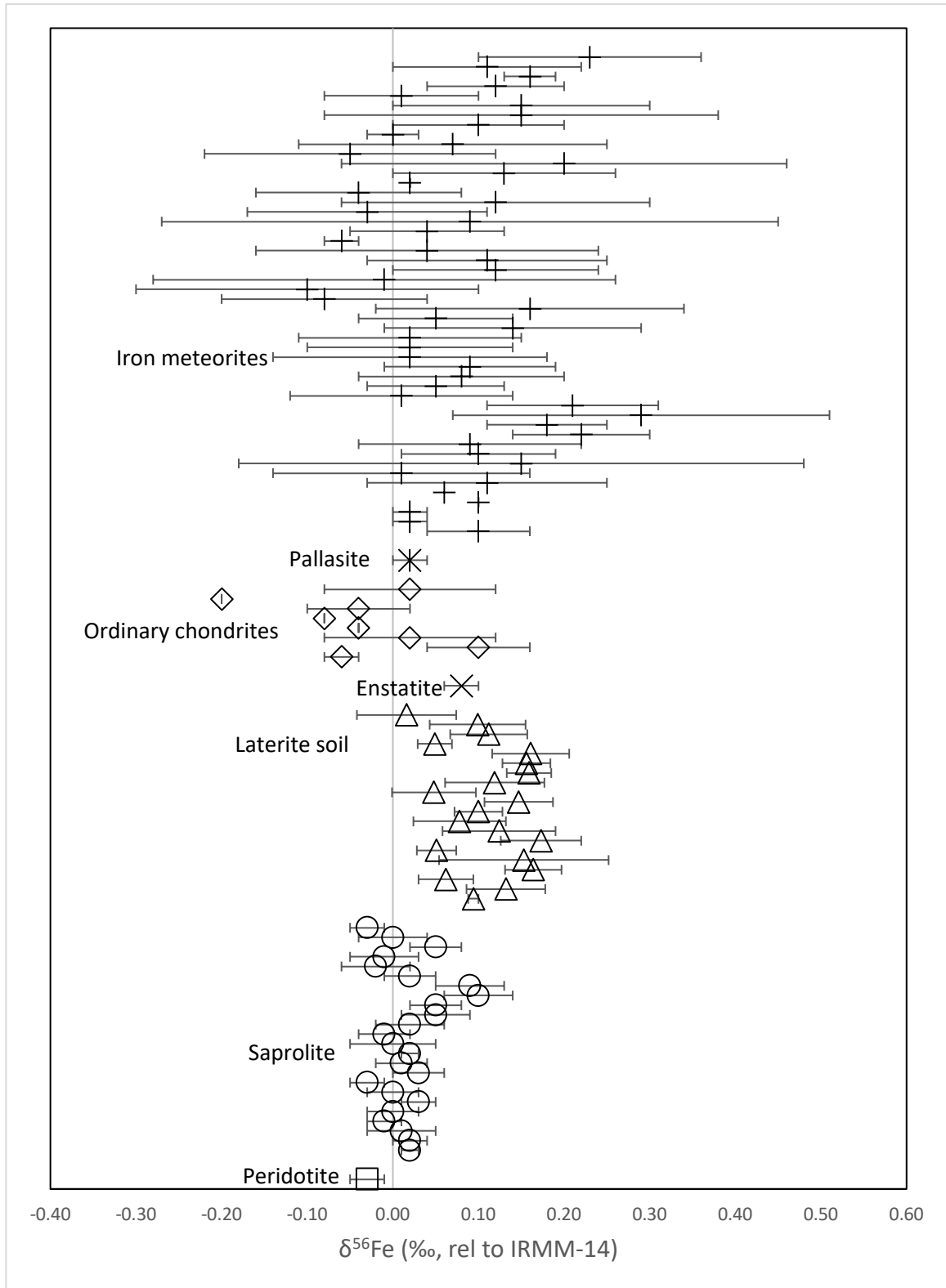
Figure 7 Range of δ⁵⁶Fe in bulk soil, peridotite, saprolite and meteorite samples from worldwide Data are compiled from Zhu et al. 2001; Moynier et al. 2007; Khem

et al. 2003; Poitrasson et al. 2004, 2005, 2008; Mullane et al. 2005; Weyer et al. 2005; Williams et al. 2006; Li et al. 2017; Liu et al. 2014.

Goethite is a major host of Ni in laterite profiles, and it is also a Fe-bearing mineral. Iron isotope fractionation may happen during the Ni adsorption and Fe release. Iron isotopic compositions may provide important information on Ni-Cu-PGE formation pathway, such as reservoir effects and partial Fe equilibrium (Dauphas, John and Rouxel 2017). Hofmann et al. (2014) suggested Fe isotopic fractionation is very narrow (less than 0.2 ‰) between Ni sulfides and silicates under high temperature magma processes. Many studies found large Fe isotope fractionation based on other soil samples showing $\delta^{56}Fe$ from −0.62‰ to +0.72‰ (Fantle and DePaolo 2004; Emmanuel et al. 2005; Thompson et al. 2007; Wiederhold et al. 2007; Yamaguchi et al. 2007), However, Li et al. (2017) reported very limited $\delta^{56}Fe$ variation (−0.03 ± 0.02‰ to 0.10 ± 0.04‰) in laterite soil samples. Thus, it is important to study Fe isotope fractionation along with laterization processes.

1.7   Lovina, ungrouped iron meteorite or a terrestrial metal?

As a secondary project to fulfill the requirements of the collaborative program in Planetary Science, this study conducted a series of trace element analyses and Fe isotopic data of selected samples.

Iron is the most abundant element in the planetary cores, and it is a major element on the silicate portion of planets. Thus, Fe isotope compositions might be helpful with studying differentiation of silicate reservoirs of planets, core formation and accretion history (Weyer et al. 2005). Many studies have provided new information in the perspective of Fe stable isotopes (Zhu et al. 2001; Poitrasson et al. 2005; Kehm et al. 2002; Weyer et al. 2005; Moynier et al. 2007; Barrat et al. 2015). Iron isotope fractionation is limited among iron meteorites groups. With the development of analytical methods and measurement instruments, investigating Fe isotope compositions between different groups of meteorites can help classify their groups. Eight iron meteorites elemental abundance and Fe isotope data can be found in the Results Chapter.

Lovina is an ungrouped iron meteorite found on the beach in Indonesia. Nishiizumi and Caffee (2011) raised a doubt over whether Lovina is a meteorite or a highly exotic form of oxidized slag. Its cm-sized pyramidal projections or ziggurats with mm-spaced ribs on the surface is remarkable. Researchers found magnetite with awaruite, but they did not observe any kamacite in it. Micro-XRD results of both weathered and fresh surface indicated there was massive taenite with minor troilite, which suggested that Lovina was an ataxite. Its high Ni and low Ir contents confirm its similarity to some ungrouped ataxites, but its high Ge and Ga contents do not agree with those ungrouped ataxites (Flemming et al. 2009). Lovina also shows dendritic structures which are similar to those found in IIE meteorites. Teplyakova (2011) suggested that Lovina underwent similar cooling processes to IIE meteorites leading to similar crystallization texture. This study aims to provide chemical compositions and Fe isotope information on Lovina and seven other grouped and ungrouped Fe meteorites. This study will use the Fe isotopic measurements to identify iron meteorite groups and discuss the potential terrestrial origin of Lovina meteorite, the meteoritical Society repository specimen of which is present at the Western Meteorite Collection.

Chapter 2

2   Methods

Prior to isotopic analysis by MC-ICPMS, elemental abundances in all of the soil, mineralized bedrock and saprolite, laterite, saprolite, bedrock and water samples were analyzed by Quadrupole ICPMS Thermo iCAP at Western University.

2.1   Terrestrial samples

All the rock, soil, and water samples were provided by Dr. Christian Schardt from University of Minnesota, Duluth. They were collected from 4 different locations or deposits from June 9th to June 12th, 2016. There are four samples containing Ni mineralization (in the form of goethite and garnierite, determined by the sample provider), seven laterite samples (in the limonite zone), six bedrock samples, four saprolite samples, one soil sample, and eight water samples collected from the Ni mining

areas in the Philippines (Table 1 and Table 9). Mineralized samples are defined as samples containing visible goethite or garnierite minerals. Three mineralized samples are altered peridotite, while the other one is highly altered saprolite. The mineralized product is garnierite, which is an Mg-Ni silicate mineral that is common in hydrous Mg silicate ore. The host rocks are saprolite, which is a phyllosilicate-rich rock retaining the original structure of the parent rock after alteration, and peridotite, which is an Mg-rich ultramafic rock containing olivine and pyroxene. Laterite samples are from the limonite zone of a laterite profile. These samples are either laterite or limonite. Bedrock samples are peridotite, including the least-altered one, highly altered ones, and serpentinized fresh one. The saprolite zone may comprise up to 80% of the thickness of a laterite profile (Butt and Cruzel, 2013). The four samples collected from saprolite zones are earthy, soft, decomposed clay-rich limonitic rocks. The soil sample was collected from the overburden of the limonitic zone. Mineral and rock standards (BIR-1, BHVO-1, DTS-1 and San Carlos olivine) were processed by the same dissolution and purification methods and measured together with the samples for inter-laboratory comparison.

2.2   Selected iron meteorite samples

	Group
KE-MC 201709-01	Iron, IIIAB
KE-MC 201709-02	Iron, IIIAB
KE-MA 201709-03	Iron, IAB
KE-MA 201709-04	Iron, IIAB
KE-MA 201709-05	Iron, IIIAB
NWA 12881	Iron, IAB
Lovina	Iron, ungrouped
Gheriat 004	Iron, IID
Filomena	Iron, IIAB

Table 2 A summary showing all the Fe meteorite samples analyzed in this study.

This study also analyzed 8 iron meteorite samples plus Filomena as a reference material. All the dissolution and chemistry processes were conducted in the GEOMETRIC Lab at Western. The Fe purification column chemistry protocol for meteorite samples was used

the same as for terrestrial samples (adapted from a combination of methods from Maréchal et al. 1999, Loss et al. 1990, and Chapman et al. 2006).

2.3 Instrumentation and laboratories

Bulk chemical compositions were analyzed by quadrupole ICP-MS Thermo iCAP at Western University. An In 10ppb solution was used as an internal standard during the measurement. Indium has two naturally occurred isotopes, ^{113}In and ^{115}In. Ni isotopic compositions were analyzed using a Multi-Collector ICP-MS Nu Plasma II in the SESAME Lab at Indiana University. Delta notation (δ) is given by

$\delta\ ^{60/58}$Ni (‰) = ($R^{60/58}_x$/$R^{60/58}_{NIST\ SRM\ 986}$-1) × 1000, where x is the unknown sample.

In addition to the laterite samples, BIR-1, BHVO-1, and DTS-1 international rock standard powders were used to monitor inter-laboratory accuracy and reproducibility of our chemistry and mass spectrometry methods.

Iron isotopic analyses were performed at the Pacific Centre for Isotopic and Geochemical Research at the University of British Columbia. A Nu Plasma 1700 MC-ICP-MS was used for Fe isotopic composition analysis.

Delta values (δ) for Fe are given by

δ^{56}Fe (‰) = ($R^{56/54}_x$/$R^{56/54}_{IRMM-014}$-1) × 1000, where x is the unknown sample.

The XRD analyses were conducted using a Phillips X'pert powder X-ray diffractometer at the Research Instruments Laboratory at University of Minnesota (UMN) in Duluth. A 1-degree divergence slit and 1-degree anti-scatter slit were used for the slit components. The scan settings used a range of 5-65 degrees, X-ray settings of 40 kV and 40 mA, step size of 0.01 degrees, dwell time of 0.45 seconds, programmable receiving slit set to 0.1 mm, with 30 kV and 10 mA X-ray settings for post-scan settings. The mineral proportions are estimated using Jade software by comparing the intensities of the measured reflections with those in reference patterns (Hubbard and Snyder, 1988).

Major and minor element oxide compositions of whole rock powders were analyzed by using a PANalytical PW2400 X-Ray Fluorescence (XRF) wavelength dispersive spectrometer at the Geoanalytical Lab at Western. A fused glass disc for each sample was made using loss on ignition (LOI) determination and Li-borate alkaline fusion method. XRF analysis of the fused glass discs using the spectrometer followed methods similar to those described in Norrish and Hutton (1969). Each fused glass disc was analyzed once, and the long-term average elemental precision is better than ±1% of reported values (Table 7).

Acid-washed Savillex® PFA Teflon beakers and plastic supplies (pipette tips, centrifuge tubes etc), 18.2 mΩ resistivity grade water purified by Millipore®, USA Advantage 10 and Q-POD Element purification systems, trace-metal grade acetone and acetic acid, in-house distilled trace-metal grade $HClO_4$, HNO_3 and HCl acids were used during all the dissolution and column chemistry processes in the GEOMETRIC Lab metal-free ULPA-filtered exhaust cabinets (Class 10) at Western University.

2.4   Sample preparation

All the solid samples were crushed into homogenized powders before chemistry processing. Prior to purification column chemistry and analyses, samples were dissolved.

2.4.1   Terrestrial sample preparation

Sample powders between 0.02 and 0.56 g were weighed and transferred to pre-cleaned 7 ml or 15 ml Teflon PFA beakers, depending on the powder weight. Concentrated HNO_3 (15M) and HF (29M) were added to the beakers in 1:10 proportions to dissolve the ultramafic silicate rock powders. Because of the absence of refractory minerals (e.g. zircons) in ultramafic rocks, the beakers were placed capped on a hotplate without pressured vessels, set to 120°C, for at least two days to completely dissolve sample powder. After two or more days, the HNO_3-HF acid mixture dried down. The fluoride residues were treated in perchloric acid ($HClO_4$) to break down fluoride phases and transform these to chlorides. The boiling point of $HClO_4$ is 203 °C, so the hotplate was set between 160 °C and 180 °C to slowly evaporate $HClO_4$. Several uptakes and dry

down steps were then performed in 6M HCl dissolution to fully dry the samples and ensure that they were fully dissolved and transformed into a chloride form prior to column chemistry. Afterwards, samples were dissolved and stored in 5 ml or 10 ml 6M HCl.

2.4.2   Fe meteorite sample preparation

About 30-100 mg of each Fe meteorite was stored in a pre-cleaned 15ml Savillex Teflon beaker firstly. Clean acetone was added to remove potential contaminants from the meteorite cut surfaces and samples were sonicated for at least 5 minutes. The same sonicating method was repeated again with QPOD clean water for three times. The dry and clean meteorite cuts were weighed in the balance room. For dissolution of metals, an aqua regia (HCl to HNO_3 ratio of around 3:1) mixture was added into sample beakers. Beakers were capped and placed on an 80 °C hotplate until the samples were dissolved. Then, the samples were dried off and re-dissolved with 2 ml 7M HNO_3 per 50-100 mg. The 7M HNO_3 dissolution-dryness step was repeated three times. Finally, 4 ml 7M HNO_3 per 50-100 mg was added to prepare the final stock solution for dilution or storing samples.

2.5   Ni purification column chemistry

For terrestrial samples Ni isotopic measurements, 2 µg of Ni are required for high-precision analysis. The masses of samples required were calculated according to the Ni whole-rock or water concentrations. In addition, 4 µg of ^{61}Ni-^{62}Ni of the double spike was added to samples (spike: sample 2:1) for correcting instrumental mass fractionation. Once elemental concentrations were measured, 4 µg of ^{61}Ni-^{62}Ni spike was added to sample aliquots and homogenized together. Spiked samples were ready for Ni purification column chemistry. The chemical purification of Ni consists of at least two sets of ion-exchange column chemistry in order to get rid of other matrix elements, especially iron which interferes directly with Ni isotopic masses, to minimize matrix effects on the Ni isotopic measurements.

Nickel purification column chemistry adapted for this study was modified from Wasylenki et al. (2015). Bio-Rad® polypropylene columns, which were cleaned in advance using 20% HCl, were filled with 2 ml pre-cleaned 200-400 mesh AG50W-X8 cation exchange resin. The resin is analytical grade resin which is certified to contain less than 100 microorganisms per gram of resin. The resin was cleaned and conditioned prior to Ni purification column chemistry. Prior to the column chemistry, samples were dissolved in 1~2 ml 10M HCl and dried down. Then, 200 μg 10M HCl was added to the sample aliquots, followed by 800 μl high-purity acetone once the samples had dissolved and right before column chemistry. The aliquots were centrifuged to check for and separate precipitates. Firstly, ~10 ml 6M HCl was added to the polypropylene columns. When all the 6M HCl passed, ~10 ml Q-POD clean water was added to further clean the resin. The cleaning steps were followed by conditioning with a mixture of 4 ml acetone and 10M HCl (20% 10M HCl and 80% acetone). After the acetone and 10M HCl conditioning mixture, samples were loaded to the column. A portion of Fe, Co, Cu and Zn would be eluted during loading the samples. A mixture of 6 ml acetone and 10M HCl (20% 10M HCl and 80% acetone) was added to the column to get rid of most of the V, Cr, Mn, Fe, Co, Cu, Zn when the loading is finished. Nickel was eluted by 6 ml of 6M HCl in new pre-cleaned Teflon beakers. The Ni cuts were dried down (in 6 ml 6M HCl) at 120°C on the hotplate, followed by a treatment with 10~15 drops of concentrated HNO_3 to get rid of organic acetone residues. The dried Ni cuts were topped up with 150 μl of 10M HCl and 850 μl of acetic acid just before the second column. The resin was washed with 10 ml 6M HCl first, followed by 10 ml of water. The conditioning step in the second column used 4 ml of a mixture of 15% 10M HCl and 85% acetic acid. The sample are loaded in 1 ml 10M HCl-acetic acid mixed solution. Nickel was eluted by 15 ml of a mixture of 15% 10M HCl and 85% acetic acid. The Ni cut from the second column was dried off and treated with 10~15 drops of concentrated HNO_3 again.

Resin:AG50W-X8 (200-400 mesh)	Reagents	Volume	Goal
First column			
Spike	Add 4 μg ^{61}Ni-^{62}Ni spike		
Dry up with 1-2 mL of 10M HCl at 130 °C			
Re-dissolve	10M HCl	200 μl	
	High purity acetone	800 μl	
Resin cleaning	6M HCl	10 ml	
	QPOD water	10 ml	
Conditioning	acetone	3.2 ml	
	10M HCl	0.8 ml	
Loading	re-dissolved sample aliquot	1 ml	Load all elements to resin. A portion of Fe, Co, Cu and Zn would be eluted.
Matrices	acetone	4.8 ml	To get rid of most of the V, Cr, Mn, Fe, Co, Cu, Zn
	10M HCl	1.2 ml	
Ni Elution	6M HCl	6 ml	To collect Ni
Dry up			
HNO$_3$ Treatment	concentrated HNO$_3$	10~15 drops	To get rid of organic matter imported by acetone
Second column			
Re-dissolution	10M HCl	150 μl	
	acetic acid	850 μl	
Resin cleaning	6M HCl	10 ml	
	QPOD water	10 ml	
Conditioning	acetic acid	3.4 ml	
	10M HCl	0.6 ml	
Loading	re-dissolved sample aliquot	1 ml	Load all elements left in the 1st column to resin.
Ni Elution	acetic acid	12.75 ml	To collect Ni
	10M HCl	2.25 ml	
Dry up			

			To get rid of organic matter imported by acetone
HNO$_3$ Treatment	concentrated HNO$_3$	10~15 drops	

Table 3 Summary of Ni elemental purification ion-exchange chromatography procedure.

Because the laterite samples have a high matrix of Ti, Cr, and Mn, two rounds of the two columns had to be run in order to meet the requirement for multi-collector ICPMS analysis. Due to the limit of precision, isobaric interferences on Ni isotope measurement (^{58}Fe on ^{58}Ni, ^{64}Zn on ^{64}Ni) have to be monitored and corrected. Tests carried out by Cook et al. (2006) displayed that Fe interference correction was effective at Fe/Ni ratio of 0.1 and lower. However, when Zn/Ni was equal to or larger than 0.01, Zn interference correction was not effective. Their tests emphasize the importance of chemical Ni separation.

Once the total of four columns finished, the final Ni cuts were dissolved in 5 ml of 2% HNO$_3$. 5% of (0.25 ml from the 5 ml of 2% HNO$_3$) the Ni cuts were taken out and diluted with 2% HNO$_3$ for elemental analysis by qICPMS at Western to check the Ni recovery and background matrix. Nickel recoveries of at least 84% to 100% for this study are calculated based on the qICP-MS analysis result of Ni cuts and Ni contents of rock powders which were conducted in the GEOMETRIC lab at Western. Together, the instrumental and dilution factor error is estimated to ±5-10%. USGS rock and mineral standards were processed with the same dissolution and purification protocol as samples, and Ni isotope analysis shows that little Ni isotope fractionation occurred during the chemistry processes (see Figure 16).

Figure 8 and 9 show the Ni column calibration result using QCS-26, which contains equal concentrations of geologically abundant matrix elements, and BCR-2 (Figure 10 and 11), which is a USGS standard basalt from Columbia River. When the sample solution goes through the resin, most elements stick to the resin while a portion of some elements will leave the resin directly. Then, when the acid strength is changed, particular elements are released from the resin while all other elements remain on the resin. Within the first column Ni cut, a large fraction of the Mg, Al, Ti, V, Cr remain together with Ni.

Thus, the second column is needed to further remove these elements. However, even though the samples are passed through two different columns, a large amount of V and Cr is left in the Ni cuts, and this may affect the Ni isotopic analysis. For this reason, two rounds of each of the two columns were carried out.
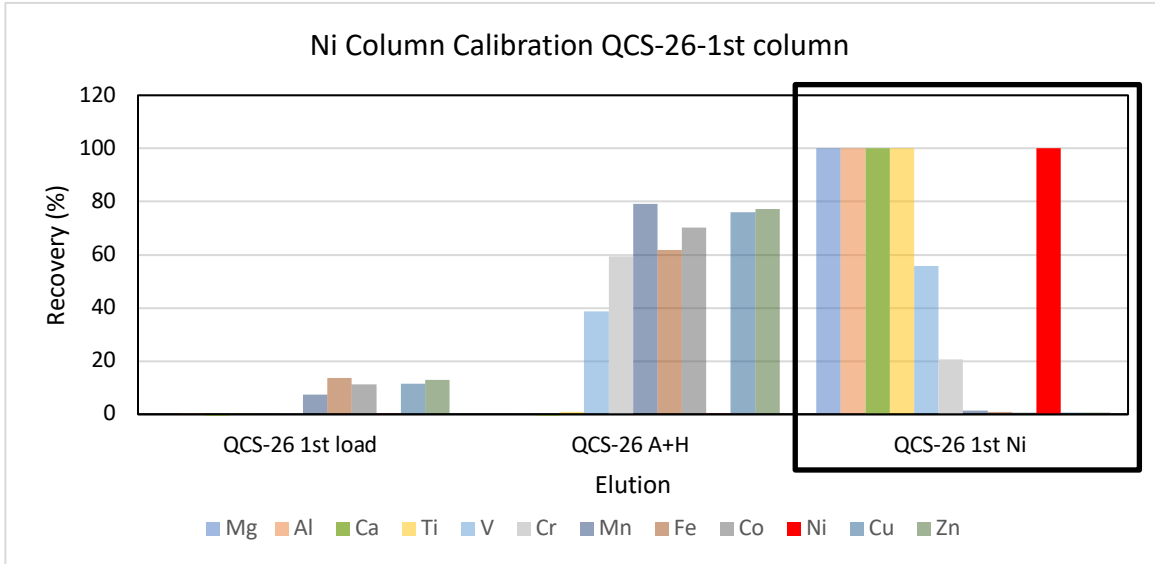
Figure 8 Ni purification 1st column chemistry calibration figure using QCS-26. QCS-26 has equal abundance of elements in the solution. 2 μg of all the elements are taken for the Ni column calibration. A+H stands for acetone + HCl step elution.
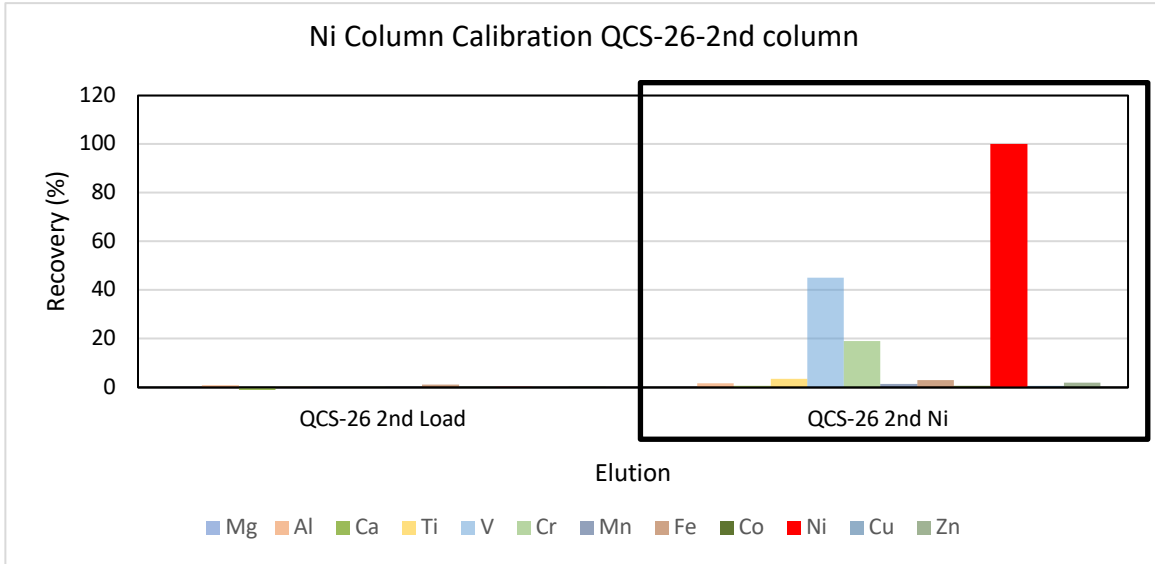
Figure 9 Ni purification 2nd column chemistry calibration figure using QCS-26. QCS-26 has equal abundance of elements in the solution. 2 µg of all the elements are taken for the Ni column calibration. A+H stands for acetone + HCl step elution.
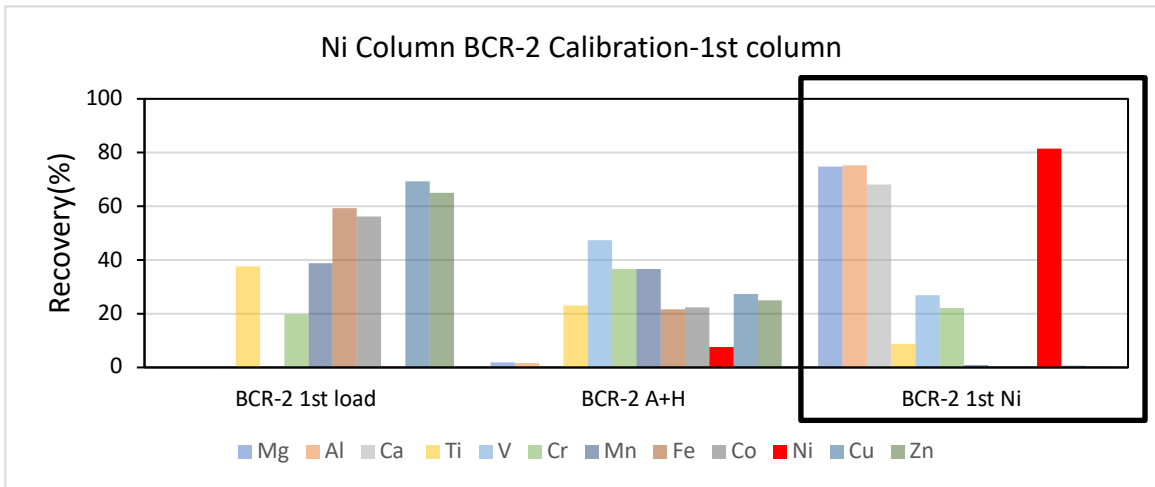
Figure 10 Ni purification 1st column chemistry calibration figure using BCR-2. BCR-2 is a USGS rock standard (basalt). 2 µg of Ni is taken for the Ni column calibration.
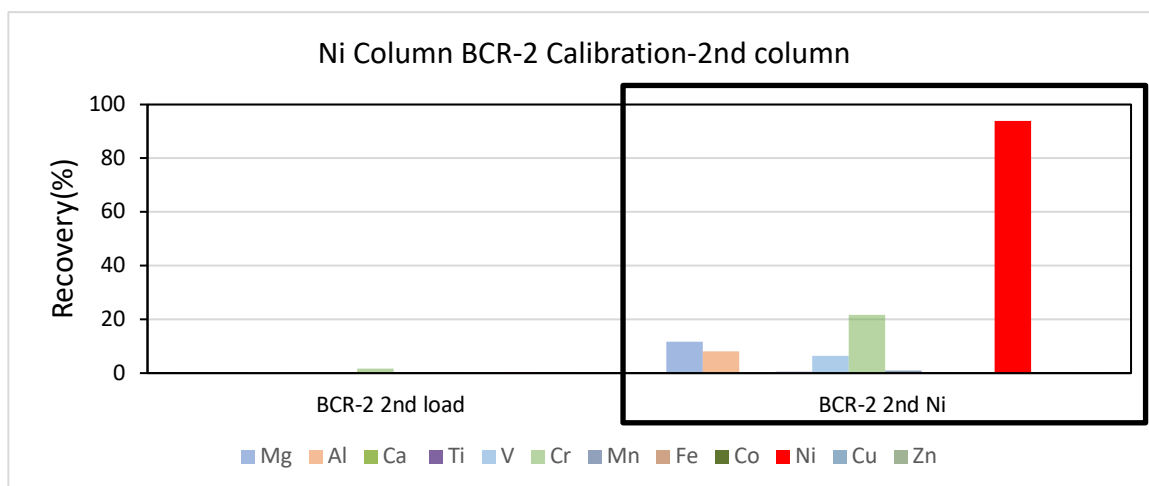
Figure 11 Ni purification 2nd column chemistry calibration figure using BCR-2. BCR-2 is a USGS rock standard (basalt). 2 μg of Ni is taken for the Ni column calibration.

2.6 Ni isotope mass spectrometry analysis

A ^{61}Ni-^{62}Ni double spike method was used in this study during the Ni purification chemistry. This double spike method was described in other Ni isotope studies carried out at the SESAME Lab (e.g., Spivak-Birndorf et al. 2018). The double spike method is used to correct for instrumental mass bias and other Ni isotopic fractionation that may occur during the Ni purification chemistry processes (Cameron et al. 2009; Spivak-Birndorf et al. 2018).

According to the statistical approach reported by Rudge et al. (2009), the best spike composition should contain ~41% ^{61}Ni and ~54% ^{62}Ni with the other 5% composed of ^{60}Ni and ^{58}Ni (Spivak-Birndorf et al. 2018). The ^{61}Ni-^{62}Ni double spike material was provided by the SEASAME Lab at Indiana University. A previous study (Gall et al., 2013) chose double spike composition based on the natural abundance of ^{61}Ni and ^{62}Ni. ^{61}Ni has a natural abundance of 1.1399%, and ^{62}Ni has a natural abundance of 3.6345%. Thus, their double spike is a mixture of 25% ^{61}Ni and 75% ^{62}Ni.

The Ni isotopic compositions were analyzed using a Nu Plasma II Multicollector ICP-MS at SESAME Laboratory at the Indiana University. The bracketing standard being used

during the isotopic measurement was NIST SRM 986. Thus, Ni isotope ratios are reported relative to NIST SRM 986 and the δ^{60}Ni of NIST SRM 986 is taken to be 0 ‰. Two aliquots of NIST SRM 986 were taken and experienced the same Ni purification chemistry as the other samples to verify that there is no fractionation during the column chemistry. Mineral and rock standards were measured for inter-laboratory comparison. Each sample was measured 4 to 5 times with measurement interval of bracketing standard NIST SRM 986.

2.7 Iron purification column chemistry

All terrestrial and meteorite samples were performed through the same Fe purification column chemistry. Iron purification column chemistry was adapted from a combination of methods from Maréchal et al. (1999), Loss et al. (1990), and Chapman et al. (2006). All acids and water used in the Cu and Fe purification column chemistry were purified by the same distillation and filtration methods as for Ni column chemistry. Bio-Rad® polypropylene columns, which were cleaned with 20% HCl previously, were filled with 2 ml pre-cleaned Bio-Rad®100-200 mesh AG MP-1M cation exchange resin. The purification protocol is described in Table 4. Purified Fe cuts were treated with 10~15 drops of concentrated 15M HNO_3, followed by uptake by 5 ml 2% HNO_3. About 2% of Fe cuts were pipetted out for ICP-MS analysis to control the Fe recovery individually.

Resin: AG MP-1M (100-200 mesh)	Reagents	Volume
Dry up the aliquots		
Re-dissolve	7M HCl	1 ml
Resin cleaning	7M HCl	10 ml
	Milli-Q water	10 ml
Conditioning	7M HCl	6 ml
Loading	re-dissolved sample aliquot	1 ml
Matrices	7M HCl	8 ml
Cu Elution	7M HCl	25 ml
Fe Elution	2M HCl	20 ml
Dry up		
HNO_3 Treatment	concentrated HNO_3	10~15 drops

Table 4 Summary of Cu and Fe elemental purification ion-exchange chromatography procedure.

The elemental analysis was conducted in the GEOMETRIC Lab at Western. The Fe recoveries are all more than 87%. The instrumental and dilution factor error is estimated to ±5-10%. USGS rock standard BIR-1 was processed with the same dissolution and purification protocol as samples, and Fe isotope analysis shows that little Fe isotope fractionation occurred during the chemistry (Figure 18).
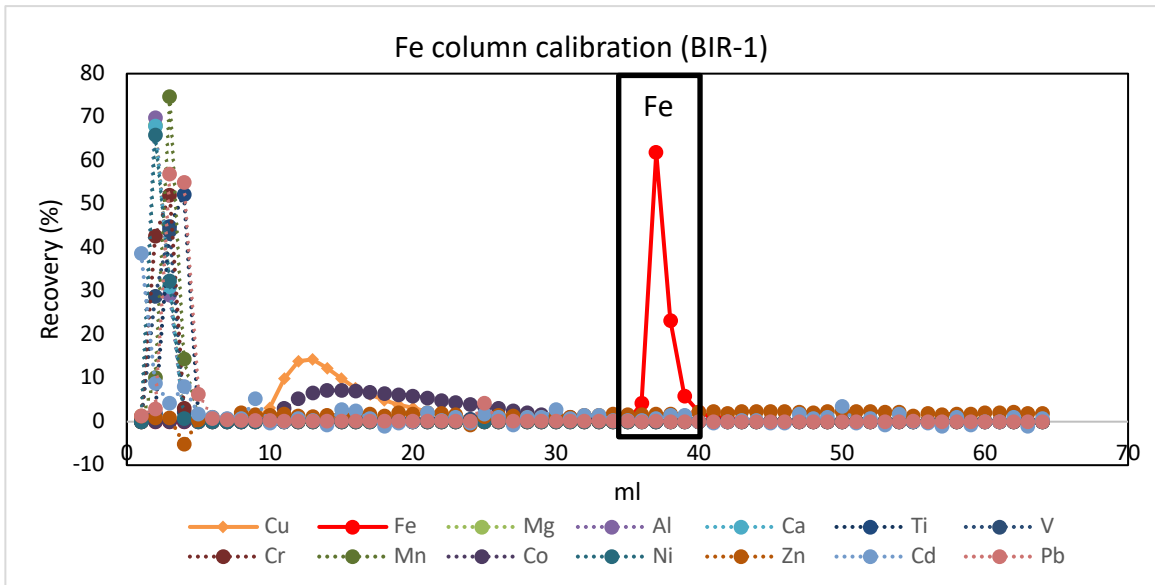
Figure 12 Calibration figure using BIR-1. BIR-1 is a USGS rock standard (basalt). One μg to 2 μg of Cu is taken for the Cu Fe purification column calibration. Solids line are representing Fe and Cu, while other elements are represented by dash lines. On the x-axis, the first ml represents the loading aliquot; 2 ml ~ 9 ml represents the matrix elution; 10 ml ~ 34 ml represents Cu elution; 35 ml ~ 54 ml represents Fe elution. Cu is eluted out in the duration of 10 ml to 25 ml, while Fe is eluted out in the duration of 35 ml to 45 ml. Co and Cu elution durations covered each other, which means these two elements are very difficult to separate completely using this column chemistry procedure. The calibration curve also shows that this column chemistry procedure can separate Fe very well.

Chapter 3

3 Results

3.1 Sample description

The 22 solid samples types vary from laterite, bedrock, saprolite, soil to mineralized bedrock and saprolite. Samples were collected and classified by Dr. Christian Schardt. Sample G-M-1, G-M-2, G-M-2A, G-L-3, G-L-4A, G-L-4B were from G-pit Gunitalunan, which is located at the southwest part of Palawan Island. M-M-5, M-L-6, M-B-7, and M-L-8 were collected from M-pit Mangingidong, which is located at the middle part of Palawan Island. E-B-9, E-L-10A, E-S-10B, E-B-10C, E-B-10D were collected from Eramen Mineral, which is located at the northern part of Zambales province. B-S-11A, B-S-11B, B-SO-12, B-L-13, B-S-14, B-B-15A, B-B-15B were collected from a deposit belonging to Benguet Mining Corp. The first letter (G, M, E, B) stands for location (G-pit Gunitalunan, M-pit Mangingidong, Eramen Mineral, Benguet Mining Corp). The second letter M, SO, L, S, B stand for sample type: mineralization, soil, laterite, saprolite, and bedrock respectively.

Deposit/Location	Sample	Type	Description
G-pit Gunitalunan	G-M-1	laterite + mineralization	Highly-altered saprolite with garnierite
	G-M-2	bedrock + mineralization	Least altered peridotite
	G-M-2A	bedrock + mineralization	Highly-altered peridotite with garnierite filling-in fractures
	G-L-3	laterite	Limonite, partially oolitic
	G-L-4A	laterite	Laterite
	G-L-4B	laterite	Limonite
M-pit Mangingidong	M-M-5	bedrock + mineralization	High-grade garnierite + altered peridotite
	M-L-6	laterite	Limonite
	M-B-7	bedrock	Least-altered bedrock
	M-L-8	laterite	Laterite
Eramen Minerals Profile taken (A-D)	E-B-9	bedrock	Highly chloritized peridotite next to W-4 (no laterite/saprolite cover)
	E-L-10A	laterite	Laterite
	E-S-10B	saprolite	Saprolite
	E-B-10C	bedrock	Peridotite, highly altered
	E-B-10D	bedrock	Peridotite, less altered
Benguet Mining Corp.	B-S-11A	saprolite	Earthy saprolite, limonitic
	B-S-11B	saprolite	Earthy saprolite, saprolitic
	B-SO-12	soil	Topsoil/overburden (limonite zone)
	B-L-13	laterite	Limonite zone; close to host rock
	B-S-14	saprolite	Saprolite
	B-B-15A	bedrock	Fresh host rock; next to altered saprolite
	B-B-15B	bedrock	Fresh host rock; serpentinized

Table 5 Summary of the detailed locations and descriptions of the 22 solid samples and one water sample of this study (sample provider and describer: Dr. Christian Schardt). The first letter indicates the sampling locations, and second letter M, SO, L, S, or B indicates the sample type: mineralization, soil, laterite, saprolite, and bedrock respectively.

3.2 XRD mineral analysis

Detailed XRD analytical method was described in Section 2.3. Sample M-M-5 is a bedrock of altered peridotite with high-grade garnierite (3.46% Ni). Dr. Christian Schardt provided the sample description based on the visible green Ni ore in peridotite. The XRD analysis indicates that the rock consists of mostly antigorite and some lizardite. Antigorite is a serpentine group mineral, which is an alteration product of olivine. Lizardite is also a serpentine group mineral but under lower alteration temperature than antigorite. Sample M-L-6 primarily existed in the limonite section of a laterite profile. It consists of mostly goethite and a small portion of quartz. E-L-10A is from a limonite section of a laterite profile. It consists of mostly goethite, indicating a Fe-oxide mineralization zone in the deposit and some hematite, kaolinite and quartz. E-S-10B is collected from the saprolite section of a laterite profile. Its XRD analysis result indicates that it consists mainly of nacrite, clinochlore, antigorite and lizardite. The presence of secondary minerals from the serpentine and chlorite groups indicate that they have replaced the primary olivine and pyroxene, but that they were not entirely replaced by Fe-oxides (goethite). It suggests that this sample was collected from an intermediate weathered zone of a laterite profile, which matches the characteristic of a saprolite zone. B-B-15 is a representative of bedrock. It consists of mostly forsterite (the best least-squares software match suggests 26.9% forsterite and 25.4% Co-forsterite, but the latter does not occur naturally), some enstatite and lizardite, which indicates that the protolith of the laterite consists of pyroxene, Mg-rich olivine, and lizardite serpentine.

3.3 Whole rock geochemical analysis
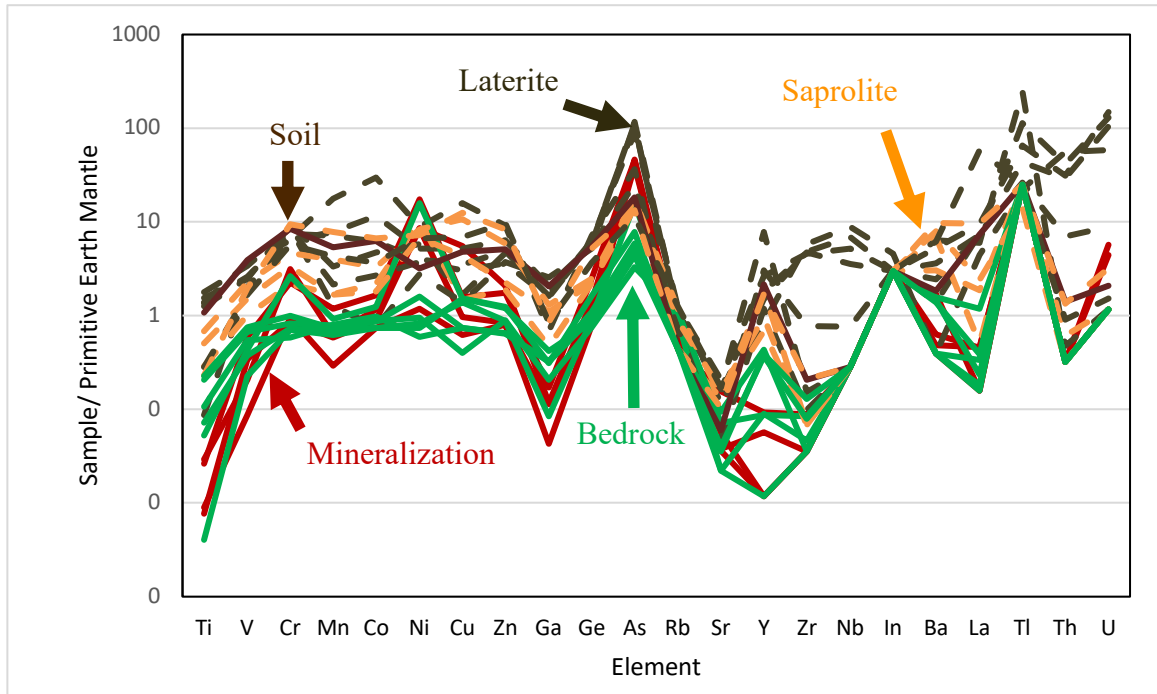
Figure 13 Whole-rock elemental analysis of solid samples conducted by qICPMS at Western University. Elemental concentrations are normalized to Primitive Earth Mantle.

The major and minor element oxide compositions of solid samples are summarized in Table 7, and their major and minor elemental analysis results are summarized in Table 8. Concentrations of Ni, Cu and Fe_2O_3 in different types of samples are summarized in Table 6 and Figure 14. Six unmineralized bedrock samples from 3 locations (M-pit Mangingidong, Eramen Mineral, Benguet Mining Corp.) exhibit high MgO concentrations (from 33.9 to 41.1%), low Fe_2O_3 concentrations (from 6.2 to 10.9%), low Cu concentrations (from 10 to 38 ppm), and extremely low Cr concentrations (0.15 to 0.70 ppm). Ni concentrations in unmineralized bedrocks are quite low, mostly ranging from 0.12 to 0.32% with an exception of 3.1% (E-B-10C).

Compared to bedrock samples, four saprolite samples collected from 2 locations (Eramen Mineral, Benguet Mining Corp.) have low MgO concentrations (from 1.8% to 27.5%), relatively high Fe_2O_3 concentrations (from 18.3 to 67.3%), high Cu concentrations (from

37 to 312 ppm), and relatively high Cr concentrations (0.57 to 2.5 ppm). Nickel concentrations of saprolite samples (1.4 to 2.1%) are constant and higher than those of bedrock samples.

Seven laterite samples collected from 4 locations (G-pit Gunitalunan, M-pit Mangingidong, Eramen Mineral, Benguet Mining Corp.) display very low MgO concentrations (0.5 to 13.2%), high Fe_2O_3 concentrations (58.9 to 73.8%), variable Cu concentrations (34 to 397 ppm) and relatively high Cr concentrations (1.5 to 2.5 ppm). Nickel concentrations of laterite samples (0.55 to 1.75%) are intermediate between those of bedrock and saprolite. High field strength elements (HFSE), such as Zr, Nb, La, Th and U, are enriched in laterite samples from limonite zones compared to other zones (See concentrations in Table 8).

The only topsoil sample collected from Benguet Mining Corp. has a Ni concentration of 0.63%, low MgO (1.1%), high Fe_2O_3 (62.2%), intermediate Cu (120 ppm), and high Cr (2.3 ppm) concentrations, which are similar to those of laterite samples.

Four samples, which came from 2 locations (G-pit Gunitalunan, M-pit Mangingidong), contain Ni mineralization. One is a laterite + mineralization, while the other 3 are bedrock + mineralization. The composition of mineralized samples is intermediate among other sample types. The MgO concentrations are between 28.3% and 38.5%. The Fe_2O_3 concentrations are between 6.0% and 15.7%. Their Cu concentrations range from 16 to 138 ppm, while its Cr concentrations range from 0.23 to 0.83 ppm. Nickel concentrations of these 4 samples vary from 0.24 to 3.46%.

As shown in Table 6A, nickel contents decrease in sequence from mineralized bedrock and saprolite, saprolite to limonite, unmineralized bedrock, soil, to groundwater. Copper contents decrease in the sequence from saprolite, limonite, soil, to mineralized bedrock and saprolite, and unmineralized bedrock. Iron contents decrease in sequence from soil, limonite, saprolite, mineralized bedrock and saprolite, and unmineralized bedrocks. In addition, samples that were collected from the same zone but different ophiolites (ZOC and POC) displayed consistent Ni, Cu, and Fe concentration ranges.
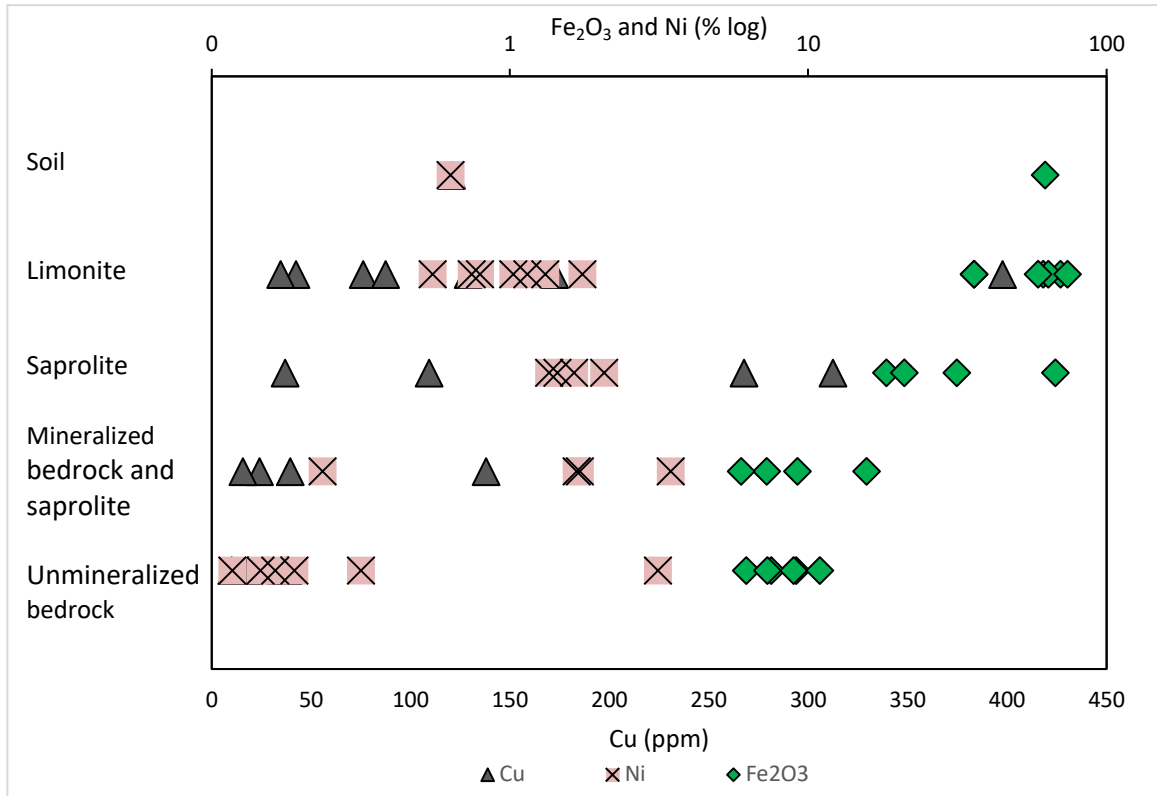
Figure 14 Summary of Ni, Cu and Fe₂O₃ concentrations ordered by sample types.

	Cu (ppm)	Fe₂O₃ (%)	Ni (%)
River water	1.5	NA	0.01
Soil	120	62	0.63
Limonite	34-397	37-74	0.55-1.8
Saprolite	36-312	18-67	1. 4-2.1
Bedrock containing mineralization	16-138	6-16	0.2-3.5
Bedrock	10-38	6-11	0.12-3.1

Table 6 A summary of chemical compositions of laterite profiles (this study).

Table 7 Summary of oxide compositions obtained by XRF analysis (elemental precision is better than ±1%, see Chapter 2 for Methods).

		SiO_2	TiO_2	Al_2O_3	Fe_2O_3	MnO	MgO	Cr_2O_3	L.O.I.	Total
		in wt %	ppm	in wt %	in wt %	in wt %	in wt %	in wt %	in wt %	in wt %
Mineralization	G-M-1	37.6	60	0.3	7.2	0.1	38.1	0.3	16.8	100.4
	G-M-2	41.8	70	0.1	9.2	0.1	32.2	1.1	16.2	100.7
	G-M-2A	40.0	70	< 0.01	6.0	<d.l.	38.5	0.4	15.9	100.7
	M-M-5	37.0	100	0.7	15.7	0.2	28.3	0.8	17.3	100.0
Laterite	G-L-3	13.7	2990	7.1	61.3	0.3	0.9	3.2	12.8	99.6
	G-L-4A	7.8	2550	6.6	70.1	0.8	0.5	2.7	11.2	100.0
	G-L-4B	11.7	2460	6.8	63.9	0.5	0.8	3.5	12.4	99.8
	M-L-6	4.5	190	3.3	73.8	1.9	1.2	2.3	12.9	99.8
	B-L-13	29.9	650	3.4	36.0	0.5	13.2	2.2	14.5	99.8
	M-L-8	1.3	3360	9.7	70.5	0.2	0.7	3.2	13.9	99.9
	E-L-10A	9.4	2770	12.3	58.9	0.8	1.3	2.3	14.5	99.7
Bedrock	M-B-7	36.8	30	0.1	6.2	0.1	41.1	0.3	16.4	100.9
	E-B-9	36.0	200	1.7	9.1	0.1	40.9	0.2	12.7	100.7
	E-B-10C	37.1	100	0.8	10.9	0.1	33.9	0.9	16.9	100.6
	E-B-10D	37.3	130	0.7	7.5	0.1	38.3	0.3	16.0	100.2
	B-B-15A	37.4	430	2.2	7.3	0.1	39.6	0.4	10.9	97.9
	B-B-15B	40.1	370	1.7	8.9	0.1	40.0	0.4	7.7	99.0
Saprolite	E-S-10B	36.1	610	2.5	18.3	0.2	27.5	0.7	15.4	100.8
	B-S-11A	30.6	1300	8.0	31.5	0.4	13.9	1.6	13.4	99.6
	B-S-14	10.8	520	2.4	67.3	0.9	1.8	3.5	13.4	100.2
	B-S-11B	35.8	990	5.8	21.0	0.2	18.1	1.2	17.2	99.4
Soil	B-SO-12	5.7	2250	12.5	62.2	0.6	1.1	3.1	14.4	99.8

Table 8 Elemental (minor and trace) compositions of 22 samples obtained by qICPMS (± 5% error on average, see Chapter 2 for Methods).

		Ni in wt%	Cu in ppm	Ti in ppm	V in ppm	Cr in wt %	Mn in wt%	Co in ppm	Zn in ppm	Ga in ppm	Ge in ppm	As in ppm
Mineralization	G-M-1	1.67	24	7	25	0.23	0.06	94	49	0.48	1.16	1.95
	G-M-2	1.71	138	28	15	0.83	0.06	122	121	0.49	1.63	2.22
	G-M-2A	0.24	16	8	6	0.25	0.03	78	46	0.18	0.90	2.31
	M-M-5	3.46	39	25	44	0.59	0.12	172	102	0.72	2.83	2.27
Laterites	G-L-3	0.74	76	1461	187	2.29	0.22	281	211	6.54	7.02	5.33
	G-L-4A	0.79	87	1285	193	1.96	0.72	645	282	6.85	6.80	5.88
	G-L-4B	1.15	42	1196	183	2.52	0.34	500	270	7.28	7.16	4.44
	M-L-6	1.75	397	82	149	1.78	1.79	3135	528	2.86	8.15	1.82
	B-L-13	1.32	172	268	124	1.52	0.44	388	568	3.56	4.22	0.57
	M-L-8	0.55	34	1699	253	2.26	0.13	79	218	10.75	5.93	5.60
	E-L-10A	1.02	129	1315	268	1.68	0.80	1207	367	8.80	6.42	1.25
Bedrocks	M-B-7	0.16	35	4	17	0.19	0.06	78	51	0.35	1.06	0.26
	E-B-9	0.12	18	101	41	0.15	0.08	102	37	1.36	1.09	0.78
	E-B-10C	3.13	38	50	32	0.70	0.09	130	72	1.31	1.86	0.39
	E-B-10D	0.19	10	69	28	0.19	0.07	92	52	0.87	0.86	0.17
	B-B-15A	0.15	38	215	56	0.26	0.07	77	69	1.77	0.98	0.22
	B-B-15B	0.32	18	195	50	0.22	0.08	91	37	1.37	1.26	0.30
Saprolites	E-S-10B	2.06	37	273	75	0.57	0.17	229	110	1.96	2.56	0.70
	B-S-11A	1.64	267	648	167	1.23	0.40	343	343	5.49	2.83	0.88
	B-S-14	1.44	312	219	146	2.50	0.79	700	484	3.57	5.92	0.67
	B-S-11B	1.35	109	483	113	0.89	0.17	189	131	4.57	2.56	0.89
Soil	B-SO-12	0.63	120	1019	287	2.25	0.55	661	297	8.60	6.29	0.92

	All in ppm	Rb	Sr	Y	Zr	Nb	Ba	La	Tl	Th	U
Mineralization	G-M-1	0.3	0.9	< 0.04	< 0.3	< 0.1	8.7	< 0.1	< 0.1	< 0.02	< 0.02
	G-M-2	< 0.2	2.5	0.3	0.7	< 0.1	2.5	0.2	< 0.1	< 0.02	0.1
	G-M-2A	0.3	0.6	< 0.04	< 0.3	< 0.1	< 2	< 0.08	< 0.1	< 0.02	0.1
	M-M-5	< 0.2	0.6	0.2	< 0.3	< 0.1	3.2	0.2	< 0.1	< 0.02	< 0.02
Laterites	G-L-3	0.5	2.6	6.1	40.0	1.6	12.4	3.5	0.1	1.8	1.8
	G-L-4A	0.5	2.4	5.0	40.3	3.2	18.3	3.7	0.2	2.6	2.2
	G-L-4B	0.5	3.3	8.8	38.6	2.4	26.9	4.8	0.1	2.0	2.6
	M-L-6	< 0.2	0.7	4.0	0.8	< 0.1	32.2	3.0	0.5	0.0	< 0.02
	B-L-13	0.6	2.7	26.5	1.3	< 0.1	31.6	29.5	< 0.1	0.1	0.0
	M-L-8	0.3	1.9	2.8	49.1	4.1	< 2	2.2	0.0	3.5	1.0
	E-L-10A	0.3	1.5	10.3	6.6	0.3	7.1	3.8	0.1	0.4	0.2
Bedrocks	M-B-7	< 0.2	< 0.4	< 0.04	< 0.3	< 0.1	< 2	< 0.08	< 0.1	< 0.02	< 0.02
	E-B-9	0.4	< 0.4	0.3	0.4	< 0.1	< 2	0.1	< 0.1	< 0.02	< 0.02
	E-B-10C	< 0.2	1.5	1.5	< 0.3	< 0.1	7.9	0.6	< 0.1	< 0.02	< 0.02
	E-B-10D	0.5	1.1	0.3	0.7	< 0.1	7.4	0.1	< 0.1	< 0.02	< 0.02
	B-B-15A	< 0.2	0.6	1.3	1.1	< 0.1	< 2	0.2	< 0.1	< 0.02	< 0.02
	B-B-15B	< 0.2	0.6	1.2	0.7	< 0.1	7.0	0.2	< 0.1	< 0.02	< 0.02
Saprolites	E-S-10B	< 0.2	2.1	2.3	0.6	< 0.1	15.4	0.9	< 0.1	0.0	< 0.02
	B-S-11A	0.5	2.1	6.1	0.6	< 0.1	40.1	1.2	0.0	< 0.02	< 0.02
	B-S-14	< 0.2	1.6	5.8	1.8	< 0.1	49.6	4.9	< 0.1	0.1	0.1
	B-S-11B	0.4	2.5	3.2	0.6	< 0.1	34.7	0.3	< 0.1	< 0.02	< 0.02
Soil	B-SO-12	< 0.2	0.9	7.3	1.7	< 0.1	9.4	3.7	0.1	0.1	0.0

3.4 Water Sample Analysis

Eight water samples were sent to Actlabs (www.actlabs.com) for hydrogeochemistry ICP-OES elemental analysis. These are natural waters with low total dissolved solid content. Samples were analyzed on the supernatant portion of water acidified to pH<2 without filtration or digestion. Sulfate content of water samples was also measured by Ion Chromatography at Actlabs.

Sample name	Type		Locations
PH-W-1	River water	water	M-pit, Mangingidong
PH-W-2	River water	water	M-pit, Mangingidong
PH-W-3	Seepage water from laterite	water	M-pit, Mangingidong
PH-W-4	Seepage water within heavily altered peridotite	water	Eramen Minerals
PH-W-5	River water	water	Eramen Minerals
PH-W-6	Seepage water	water	Benguet Mining Corp.
PH-R-1	Rainwater from catchment	water	M-pit, Mangingidong
PH-WG-1		solids in water	Eramen Minerals

Table 9 Summary of water sample types and locations. PH stands for Philippines; W stands for water; R stands for rainwater; WG stands for water with solids.

Figure 15 shows the sulfate concentrations of 8 water samples (detailed data are summarized in Table 10). The rainwater sample (PH-R-1) and water sample containing solids (PH-WG-1) have extremely low sulfate concentrations (<1.6 mg/L), and their Ni concentrations are below detection limits of ICP-OES (< 5 µg/L). Thus, they are not shown in Figure 15. The river water sample collected from M-pit (PH-W-2) has very high sulfate concentration (222 mg/L) and Ni concentration (79 µg/L). Other samples show constant sulfate concentrations (6.9 to 22 mg/L). Due to the low Ni concentrations of most water samples and limited volume available, PH-W-2 was the only one water sample which could be selected for Ni isotope analysis.
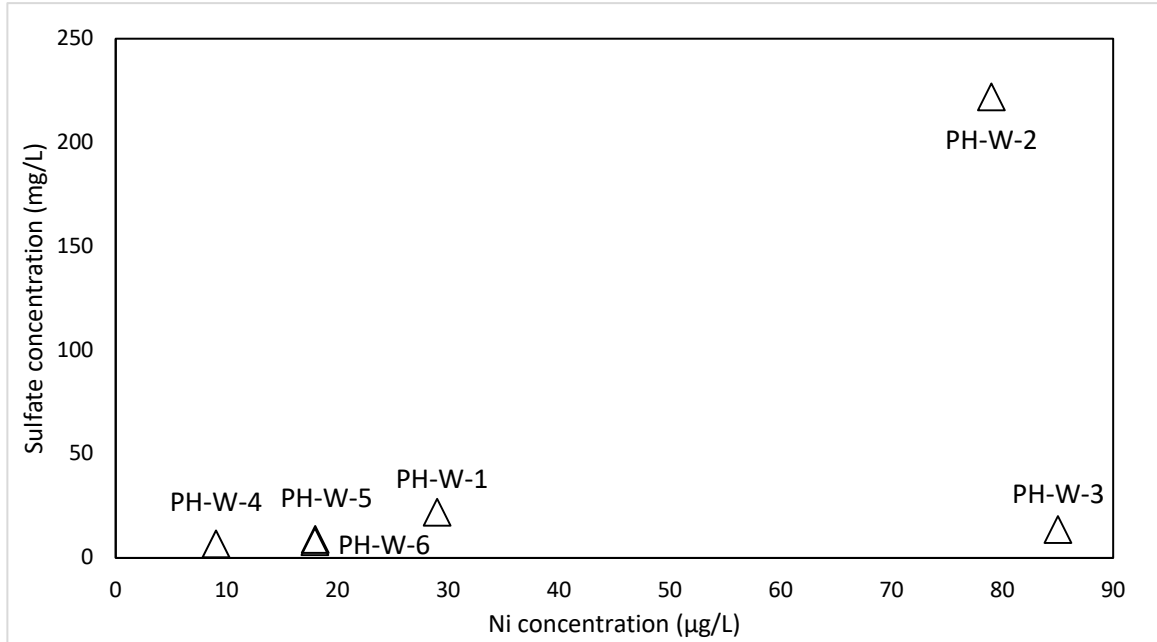
Figure 15 Sulfate concentrations (detection limit of 0.03 mg/L) against Ni concentrations (detection limit of 5 µg/L) of water samples. PH-R-1 and PH-WG-1 have too low Ni and Fe contents to be detected by the instrument.

Analyte Symbol	Unit	Detection Limit	Analysis Method	PH-W-1 M-pit	PH-W-2 M-pit	PH-W-3 M-pit	PH-W-4 Eramen Minerals	PH-W-5 Eramen Minerals	PH-W-6 Benguet Mining Corp.	PH-R-1 M-pit	PH-WG-1 Eramen Minerals
K	mg/L	0.1	ICP-OES	0.2	1.8	0.6	0.1	0.6	< 0.1	0.4	0.4
Mg	mg/L	0.1	ICP-OES	34.3	47.1	28.9	24.5	31.9	14.1	2.2	2.2
Mn	mg/L	0.01	ICP-OES	< 0.01	0.27	< 0.01	< 0.01	0.01	< 0.01	< 0.01	< 0.01
Si	mg/L	0.1	ICP-OES	24.3	13.5	12	16.6	16.7	12.1	0.9	0.9
Ca	mg/L	0.1	ICP-OES	0.4	67.8	0.8	0.8	2.8	1.2	6.3	6.4
Co	µg/L	2	ICP-OES	< 2	6	< 2	< 2	< 2	< 2	< 2	< 2
Cr	µg/L	20	ICP-OES	100	< 20	20	30	< 20	< 20	< 20	< 20
Fe	mg/L	0.01	ICP-OES	0.17	0.16	0.06	0.02	0.05	0.03	< 0.01	< 0.01
Cu	µg/L	2	ICP-OES	< 2	< 2	< 2	< 2	2	< 2	< 2	< 2
Na	mg/L	0.1	ICP-OES	2.3	33.7	1.2	1	2.6	1.2	< 0.1	< 0.1
Ni	µg/L	5	ICP-OES	29	79	85	9	18	18	< 5	< 5
P	mg/L	0.02	ICP-OES	< 0.02	0.04	< 0.02	< 0.02	< 0.02	< 0.02	< 0.02	< 0.02
S	mg/L	1	ICP-OES	5	71	3	2	2	2	< 1	< 1
Sr	µg/L	10	ICP-OES	< 10	400	< 10	< 10	< 10	< 10	20	20
Zn	µg/L	5	ICP-OES	17	19	11	< 5	6	92	198	204
SO4	mg/L	0.03	IC	22	222	13.6	6.89	9	7.69	0.66	1.59

Table 10 Summary of locations and elemental compositions and sulfate concentrations of 8 water samples collected around the Ni lateritic mines.

3.5 Ni isotopic data

3.5.1 Standards
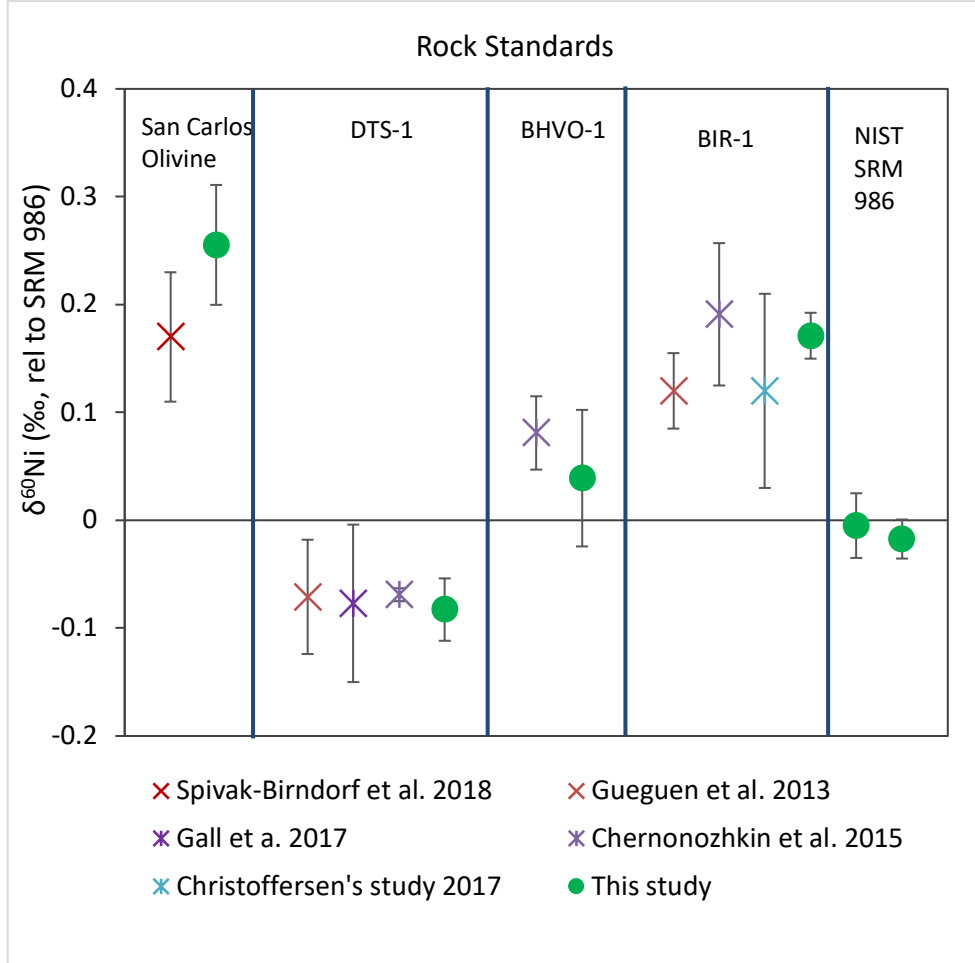
Figure 16 Ni isotopic compositions of NIST SRM 986 and rock and mineral standards from this study and literature. Error bars are 2SD for the average of repeated measurements (see text for further details).

Mineral and rock standards (San Carlos olivine, DTS-1, BHVO-1, and BIR-1) were analyzed for their Ni isotopic compositions. For inter-laboratory comparison, a compilation of literature reports and results from this study are presented together in Figure 16.

San Carlos olivine was prepared from a mantle peridotite xenolith collected in Arizona, USA. It has a δ^{60}Ni of 0.23 ± 0.07‰ (average and error bars are 2SD calculated from n=4 repeated measurements) which overlaps within error bars with the only published value of 0.17 ± 0.06‰ (Spivak-Birndorf et al., 2018).

We find δ^{60}Ni of -0.08 ± 0.03‰ (n=5) for DTS-1 which is in agreement with -0.08 ± 0.07‰ to -0.07 ± 0.01‰ reported by Gall et al. (2017), Chernonozhkin et al. (2015), and Gueguen et al. (2013).

Standard BHVO-1 has δ^{60}Ni of 0.04 ± 0.06‰ (n=5) which agrees well with 0.08 ± 0.03‰ reported by Chernonozhkin et al. (2015), and finally BIR-1 has δ^{60}Ni of 0.17 ± 0.02‰ which is also in agreement with 0.12 ± 0.09‰ to 0.19 ± 0.07‰ reported by Gueguen et al. (2013) and Chernonozhkin et al. (2015).

Two aliquots of pure Ni NIST SRM 986 solution (no rock matrix) were passed through column chemistry to control the absence of potential isotopic fractionation effects during our procedure and measurement. The same process with two repeated Ni ion-exchange chromatography, as for the sample aliquots, was performed on two NIST SRM 986 2μg Ni aliquots. As NIST SRM 986 is the bracketing standard used for Ni isotopic analysis, its δ^{60}Ni by definition should be 0‰ if no fractionation was introduced during the column ion-exchange chromatography protocol. We obtain δ^{60}Ni of -0.005 ± 0.030‰ (n=3) and -0.017 ± 0.018‰ (n=3) respectively for the two processed NIST SRM 986 Ni. These values indicate that there is no fractionation during the Ni ion-exchange chromatography resolved outside the analytical precision for both measurements.

Two repeated analyses of samples B-S-11A and B-S-14 (same dissolution, different solution aliquots) were also carried out to account for the external reproducibility of our method between different ion-exchange chromatography column and mass spectrometric analysis sessions. Sample B-S-11A-1 has δ^{60}Ni of -0.17 ± 0.07‰ and its duplicate analysis has -0.18 ± 0.06‰. B-S-14-1 has δ^{60}Ni of 0.11 ± 0.02‰ and its duplicate analysis has δ^{60}Ni of 0.11 ± 0.04‰. The two duplicated sample measurements are thus in perfect agreement with each other within internal analytical error.

To summarize, the Ni isotopic analyses of international isotopic and rock standards and the sample duplicate tests together indicate that the chemistry protocol, double spike corrections, and mass spectrometric measurements provided results consistent with other laboratories and were also reproducible within our analytical errors associated with MC-ICPMS measurements. Our measurements are thus accurate and precise against the recent literature reported for Ni isotopic analyses, and reproducible between analytical sessions and rock sample matrices.

3.5.2   Samples

The detailed Ni isotopic data are provided in Table 11. Analyses of our samples show up to 1.3‰ variations in $\delta^{60}Ni$ (2SD) from 0.95 ± 0.11‰ for water (n=1 PH-W-2), 0.22 ±0.57‰ (n=4) for mineralized samples, -0.03 ± 0.99‰ (n=6) for bedrock, -0.17 ± 0.01‰ for a limonite soil (n=1), -0.19 ± 0.75‰ for saprolites (n=6), and -0.22 ± 0.34‰ for laterites (n=7) (all 2SD). The only river water sample has thus the heaviest Ni isotopic composition among all sample types.

Six unmineralized bedrock samples showed that Ni isotopic composition variation of 1.46‰ ranging from -0.99‰ (E-B-10C) to 0.48‰ (B-B-15B). The average Ni isotopic composition of bedrock samples is -0.03 ± 0.99‰ (2SD, n=6). Sample E-B-10C has a mineralogical composition of highly altered peridotite, while B-B-15B is a serpentinized fresh host rock. Samples E-B-10C and E-B-10D were collected from the bedrock zone of the same laterite profile, but E-B-10D ($\delta^{60}Ni = 0.12 ± 0.07‰$) showed a significant difference from E-B-10C ($\delta^{60}Ni = 0.99 ± 0.05‰$). Although E-B-10C and E-B-10D were from the sample profile, E-B-10D was less altered than 10C, which indicates that alteration reactions might decrease $\delta^{60}Ni$ value of bedrocks. Samples B-B-15A and B-B-15B were also collected from the same area, but B-B-15A was closer to the altered saprolite zone than B-B-15B.

Samples E-S-10B, B-S-11A, B-S-11B, and B-S-14 are from the saprolite zone which is the zone above the bedrock zone in the laterite profile. Their Ni isotopic analyses have a variation of ~1‰ ranging from -0.90‰ to 0.11‰, with an average of -0.19 ± 0.75‰ (2SD, n=6).

Samples G-L-3, G-L-4A, G-L-4B, M-L-6, M-L-8, E-L-10A and B-L-13 are from the limonitic laterite zone. Almost all of them are limonite, but B-L-13 is closer to the host rock peridotite, according to Dr. Schardt's description. They display a Ni variation of ~0.5‰ ranging from -0.56‰ to -0.09‰. The average value for limonite laterite zone of -0.22 ± 0.34‰ (2SD, n=7) is similar to the average value for underlying saprolite zone of -0.19 ± 0.75‰ (2SD, n=6), and displays a heavy Ni depletion. From the bedrock samples to the limonite samples, the depletion of heavier Ni isotopes from the solid phase, defined as $\Delta^{60}Ni_{\text{Limonite-Bedrock}}$ is up to -0.19 ± 0.32‰ (average $\delta^{60}Ni_{\text{Limonite}}$ = -0.22 ± 0.34‰; average $\delta^{60}Ni_{\text{Unmineralized bedrock}}$ = -0.03 ± 0.99‰).

The only topsoil sample (B-SO-12) belongs to the limonite zone. The Ni isotopic composition is $\delta^{60}Ni$=-0.17 ± 0.01‰, which is within the Ni isotopic composition range of limonite samples found in this study.

Sample G-M-1 is from the mineralization within the limonite zone, G-M-2, G-M-2A and M-M-5 are mineralization filling-in fractures of the peridotite bedrock. The mineralized products were garnierite and goethite. G-M-2 is the least altered sample. These samples have Ni isotopic compositions which vary by ~0.6‰ ranging from $\delta^{60}Ni_{\text{G-M-2}}$ = -0.06 ± 0.03‰ to $\delta^{60}Ni_{\text{M-M-5}}$ = 0.57 ± 0.06‰. The average $\delta^{60}Ni$ value for mineralized samples zone is -0.22 ± 0.57‰ (2SD, n=4).

Figure 17 presents the Ni isotopic data against Ni concentrations of the samples measured in the present study. River water sample, PH-W-2, displays the lowest Ni concentration (79 ppb) but the heaviest Ni isotope composition ($\delta^{60}Ni$ = 0.95 ± 0.10‰). Most bedrock samples show low Ni concentrations (0.12% to 0.32%) but positive $\delta^{60}Ni$ values (0.03 ± 0.07‰ to 0.47 ± 0.07‰). However, the bedrock sample E-B-10C shows high Ni concentration (3.13%) and negative $\delta^{60}Ni$ value of -0.99 ± 0.05‰.

Compared to bedrock samples, saprolite samples show high Ni concentration (1.35% to 2.06%) and light Ni isotope compositions ($\delta^{60}Ni$ = -0.90 ± 0.06‰ to 0.11 ± 0.04‰).

Laterite samples show intermediate Ni concentrations (0.55% to 1.75%) between bedrock and saprolite samples, and similar Ni isotope compositions ($\delta^{60}Ni$ = -0.56 ± 0.03‰ to -

0.09 ± 0.07‰) with saprolite samples. The only topsoil sample shows similar Ni concentration (0.63%) and Ni isotope compositions (δ^{60}Ni = -0.17 ± 0.01‰) similar to laterite samples.

The Ni concentrations of mineralized samples are various (0.24% to 3.46%) with a range of δ^{60}Ni values from -0.06 ± 0.03‰ to 0.57 ± 0.06‰ (Figure 17).
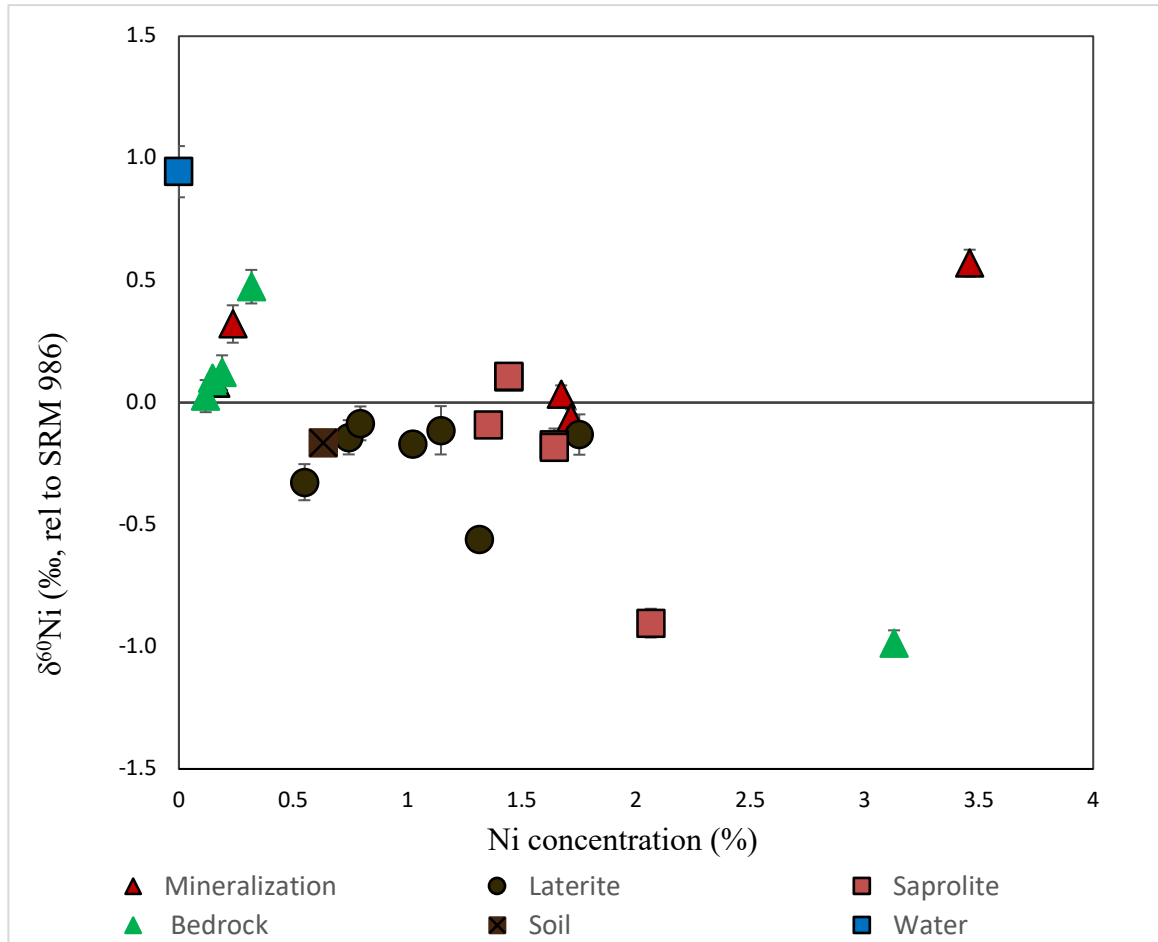
Figure 17 Ni concentrations and isotopic compositions (rel. to SRM 986) of water, bedrock, limonite laterite, saprolite, topsoil and mineralized bedrock samples of this study.

		$\delta^{60}Ni$ (‰)	# of repeat	2SD
Mineralization	G-M-1	0.04	3	0.03
	G-M-2	-0.06	3	0.03
	G-M-2A	0.32	4	0.08
	M-M-5	0.57	4	0.06
	Weighted average	0.22		0.57
Laterite	G-L-3	-0.14	3	0.07
	G-L-4A	-0.09	4	0.07
	G-L-4B	-0.11	4	0.10
	M-L-6	-0.13	3	0.08
	B-L-13	-0.56	3	0.03
	M-L-8	-0.33	4	0.07
	E-L-10A	-0.17	4	0.05
	Weighted average	-0.22		0.34
Bedrock	M-B-7	0.08	3	0.01
	E-B-9	0.03	3	0.07
	E-B-10C	-0.99	3	0.05
	E-B-10D	0.12	4	0.07
	B-B-15A	0.10	4	0.01
	B-B-15B	0.47	3	0.07
	Weighted average	-0.03		0.99
Saprolite	E-S-10B	-0.90	3	0.06
	B-S-11A	-0.17	4	0.07
	B-S-11A-dup	-0.18	3	0.05
	B-S-14-dup	0.11	4	0.04
	B-S-14	0.11	4	0.02
	B-S-11B	-0.09	3	0.03
	Weighted average	-0.19		0.75
Soil	B-SO-12	-0.17	3	0.01
All samples	Weighted average	-0.09		0.71
Water	PH-W-2	0.95	4	0.10
Rock Standards	BIR-1	0.17	3	0.02
	San Carlos Olivine	0.26	3	0.06
	BHVO-1	0.04	5	0.06
	DTS-1	-0.08	5	0.03

Table 11 Summary of Ni isotopic compositions of samples and standards. 2SD calculated from the number of repeated bracketed Ni isotopic measurements (see Methods for further details).

3.6 Fe isotopic data

3.6.1 Standards

The Fe isotopic data for USGS basalt Icelandic rock standard BIR-1 from this study are compared with measurements found in the literature which provide an average δ^{56}Fe of 0.08 ± 0.06 ‰ in Figure 18 (Poitrasson et al. 2004; Weyer et al. 2005; Dideriksen et al. 2006; Schoenberg and von Blanckenburg 2006; Schuessler et al. 2009; Liu et al. 2014; Barrat et al. 2015). We find δ^{56}Fe (relative to IRMM-14) of 0.08 ± 0.17‰ and 0.10 ± 0.09‰ (2SD) for our two duplicated measurements of BIR-1 (Figure 18). While the errors on repeated measurements are comparatively (and anomalously) large for this first session of MC-ICPMS measurements, the absolute values are nevertheless in good agreement with other laboratory values (Figure 18).
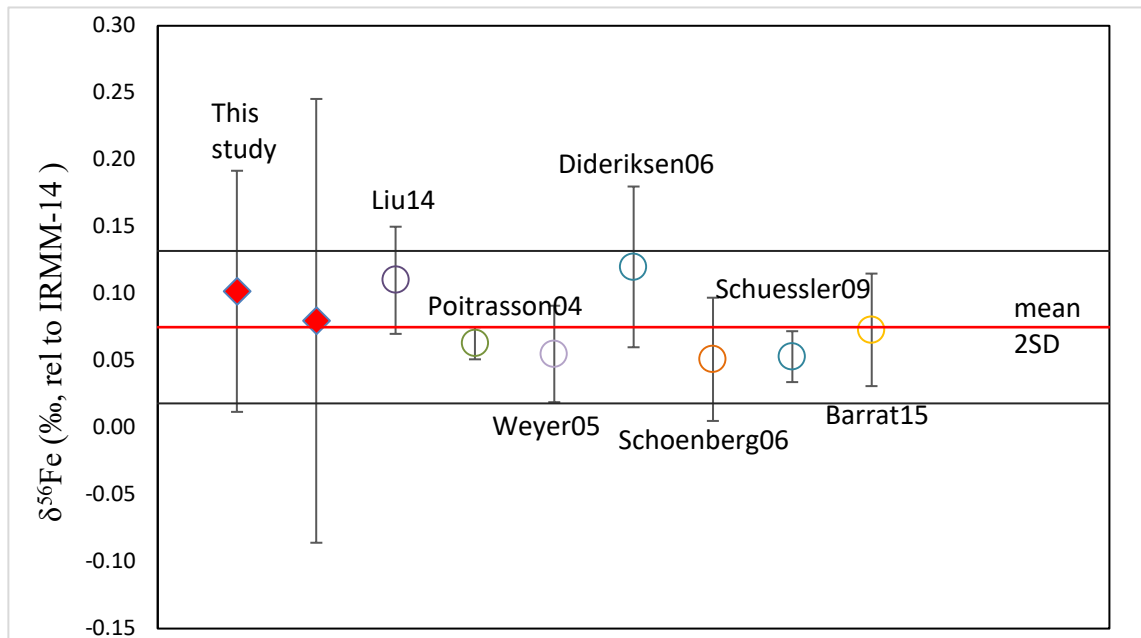
Figure 18 Fe isotopic compositions of rock standard BIR-1 from this study and literature. Red triangles are measurements of this study. Circles are literature data and reference sources (see details in text).

3.6.2   Samples

The Fe isotopic data of terrestrial samples are given in Table 12. The average and correlated error of the $\delta^{56}Fe$ composition relative to IRMM-14 is 0.03 ± 0.03‰ amongst all lithology groups. The absolute variations in $\delta^{56}Fe$ (2SD) range from -0.02 ± 0.10‰ for mineralized samples (n=2), 0.04 ± 0.05‰ (n=3) for laterite samples, 0.04 ± 0.05‰ (n=3) for bedrocks, 0.04 ± 0.08‰ for saprolite samples (n=2), and -0.03 ± 0.16‰ for the limonite soil (n=1). Unmineralized bedrock samples and mineralized samples have very low Fe concentrations (4.9% to 7.9%). Saprolite and laterite samples display similar Fe concentrations (13.2% to 43.6%; 23.7% to 53.1% respectively) which are higher than those of bedrock samples. Iron concentration of the topsoil sample (38.5%) is also within the laterite Fe concentration range.
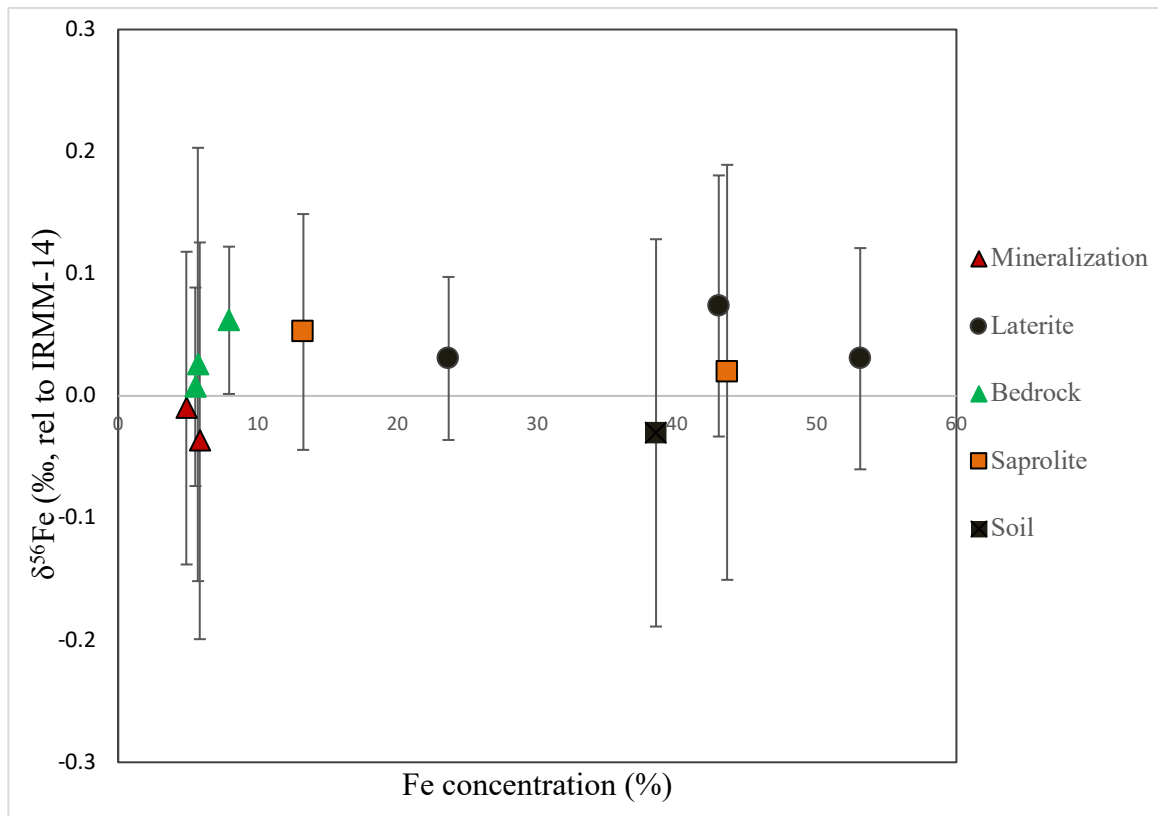
Figure 19 Fe isotopic compositions (rel. to IRMM-14) of selected bedrock, limonite laterite, saprolite, topsoil and mineralized bedrock samples of this study.

Sample type	Sample name	$\delta^{56}Fe$ (‰)	repeat #	2SD
Mineralization	G-M-2	-0.04	5	0.16
	G-M-2A	-0.01	4	0.13
	Weighted average	-0.02		0.10
Laterite	E-L-10A	0.07	5	0.11
	M-L-6	0.03	4	0.09
	B-L-13	0.03	4	0.07
	Weighted average	0.04		0.05
Bedrock	E-B-10C	0.06	4	0.06
	B-B-15A	0.01	5	0.08
	B-B-15B	0.03	5	0.18
	Weighted average	0.04		0.05
Saprolite	E-S-10B	0.05	4	0.1
	B-S-14	0.02	5	0.17
	Weighted average	0.04		0.08
Soil	B-SO-12	-0.03	5	0.16
All samples	Weighted average	0.03		0.03
Rock Standard	BIR-1	0.10	5	0.09
	BIR-1-duplicate	0.08	3	0.17
	Weighted average	0.10		0.08

Table 12 Summary of detailed Fe isotopic compositions analyze results samples and rock/mineral standards.

3.7   Iron meteorite analysis

The elemental composition of iron meteorites is dominated by Fe, Ni, and Co, which together comprise more than 95% of the meteorite mass. Iron meteorites are classified based on their chemical compositions for trace highly-siderophile elements.

3.7.1   Meteorites' elemental compositions

Most iron meteorites can be classified in one of 12 groups based on their chemical, mineralogical and structural properties. The groups are well-resolved on plots of Ni against trace elements, such as Ga, Ge and Ir (Scott et al. 1975). About 15% of iron meteorites do not fit the 12 classifications and are classified as ungrouped iron meteorites. Scott et al. suggested that there were two types with different histories: (1) IIAB, IIIAB, IVA, IIC, IID, IVB and possibly IC, IIIE, and IIIF group iron meteorites

show correlated properties and similar chemical and mineralogical trends; (2) IAB, IIICD, possibly IIE group iron meteorites show weak properties correlations and different chemical and mineralogical trends.

A new chip of the Lovina ungrouped iron meteorite was analyzed by qICPMS. Only INAA data were reported in the original report for classification of Lovina (Connelly et al. 2008). The analysis report was limited for some trace elements as not all HSE are well analyzed by INAA or due to higher detection limits than ICPMS. Several iron meteorites were recently classified at the Western Meteorite Collection and data are reported for comparison. Considering their reported elemental abundances, the 8 iron meteorites selected for this study are classified as listed below. All these meteorites were made available from the Western Meteorite Collection.

Sample ID	Group	Co (%)	Ni (%)
KE-MC 201709-01	Iron, IIIAB	0.47	7.0
KE-MC 201709-02	Iron, IIIAB	0.39	6.3
KE-MA 201709-03	Iron, IAB	0.37	5.3
KE-MA 201709-04	Iron, IIAB	0.38	5.7
KE-MA 201709-05	Iron, IIIAB	0.36	6.4
NWA 12881	Iron, IAB-MG	0.51	7.1
Lovina (Connelly et al. 2008)	Iron, ungrouped, ataxite	0.87	34.5
Gheriat 004 (Gattacceca et al. 2019)	IID	0.64	9.8

Table 13 Summary of major elemental compositions of meteorite samples from this study.

Sample ID	Ga	As	Ir	Au
	µg/g	µg/g	µg/g	µg/g
KE-MC 201709-01	22	6.0	6.7	1.9
KE-MC 201709-02	20	5.6	3.2	1.5
KE-MA 201709-03	88	10.9	2.2	3.7
KE-MA 201709-04	18	4.3	16.7	1.3
KE-MA 201709-05	17	6.1	0.3	1.4
NWA 12881	60	5.6	3.5	1.2
Lovina (Connelly et al. 2008)	22	5.6	0.252	0.07
Gheriat 004 (Gattacceca et al. 2019)	73	6.5	9.8	0.6

Table 14 Summary of selected highly siderophile elements (HSE) & Au qICPMS elemental analyze results of meteorite samples.

The concentrations of Au and Cr (ppm) against Ni (%) of Lovina are shown against literature data for iron meteorites (Rasmussen et al. 1987; Pernicka and Wasson 1987; Wasson et al. 1989; Gemelli et al. 2015; Lovering et al. 1957; Smales et al. 1967; Malvin et al. 1984; Petaev and Jacobsen 2004; Campbell and Humayun 2005) in Figures 20 and 21. Lovina has high Ni as it is an ataxite, low Au and high Cr concentrations compared with reported grouped iron meteorite data. It would be more similar to IVB iron meteorites.

Figure 20 Au (ppm) concentrations of Lovina against literature data (see details in text).
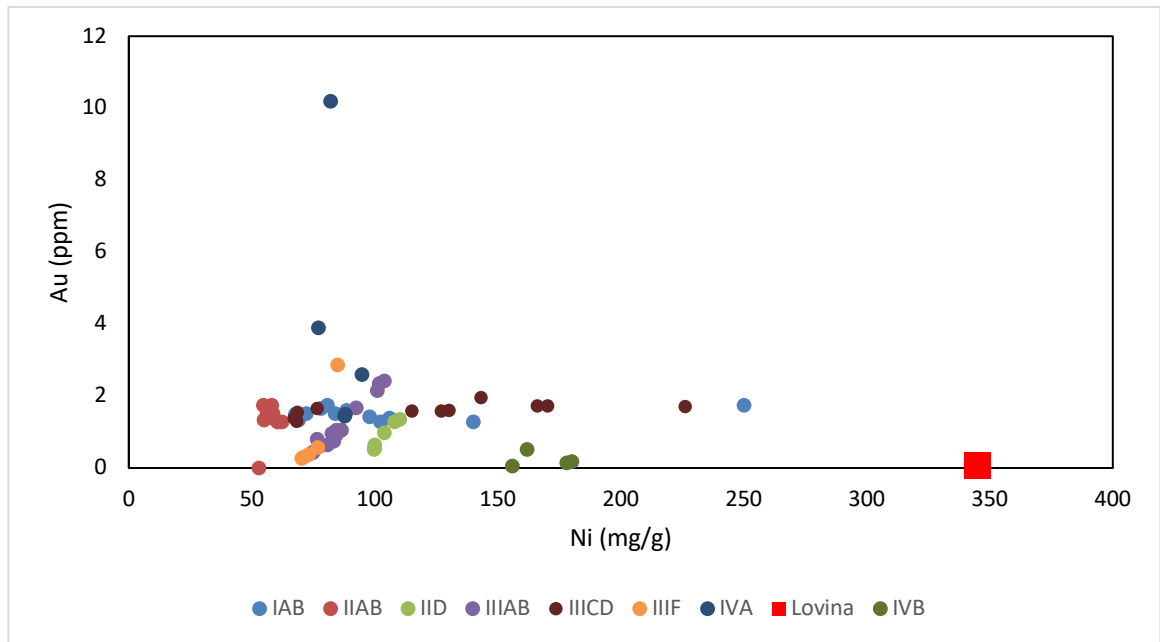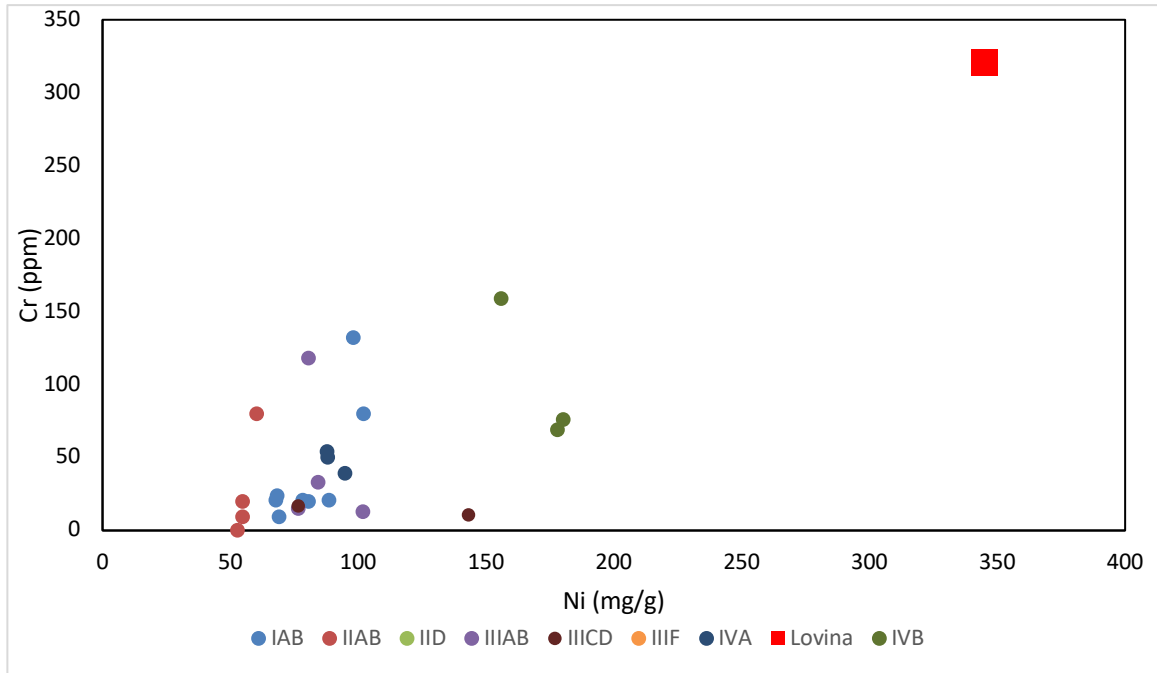
Figure 21 Cr (ppm) concentrations of Lovina against literature data. Literature data (see detail in text).

3.7.2　Meteorites' Fe isotope data

Measurements of the bracketing standard IRMM-14 were carried out at the beginning of analytical sessions and during sample measurements. During a second analytical session for Fe isotopes, we obtained better stability than for the first session (terrestrial samples)
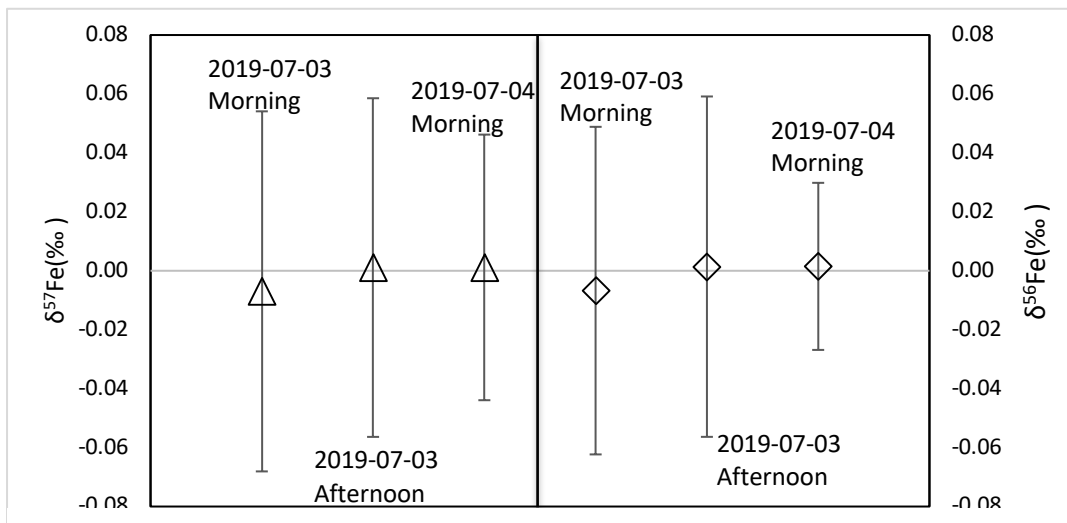
Figure 22 Daily average δ^{56}Fe and δ^{57}Fe of IRMM-14 with 2SD.

and an average $\delta^{56}Fe$ of -0.01± 0.06‰ (repeated measurements, n=12), 0.00 ± 0.06‰ (n=3), 0.00 ± 0.03‰ (n=5), separately. Also, we obtained $\delta^{57}Fe$ of -0.01± 0.06‰ (repeated measurements, n=12), 0.00 ± 0.06‰ (n=3), 0.00 ± 0.05‰ (n=5), separately (Figure 22).

Detailed Fe isotopic data are shown in Table 15. $\delta^{56}Fe$ and $\delta^{57}Fe$ (Figure 23) show deviation from the line with a slope of 0.59. This is indicating issues in the measurements. This study will continue to discuss $\delta^{57}Fe$ as there is not much ArO interference on measurement of $\delta^{57}Fe$ compared with ^{56}Fe.
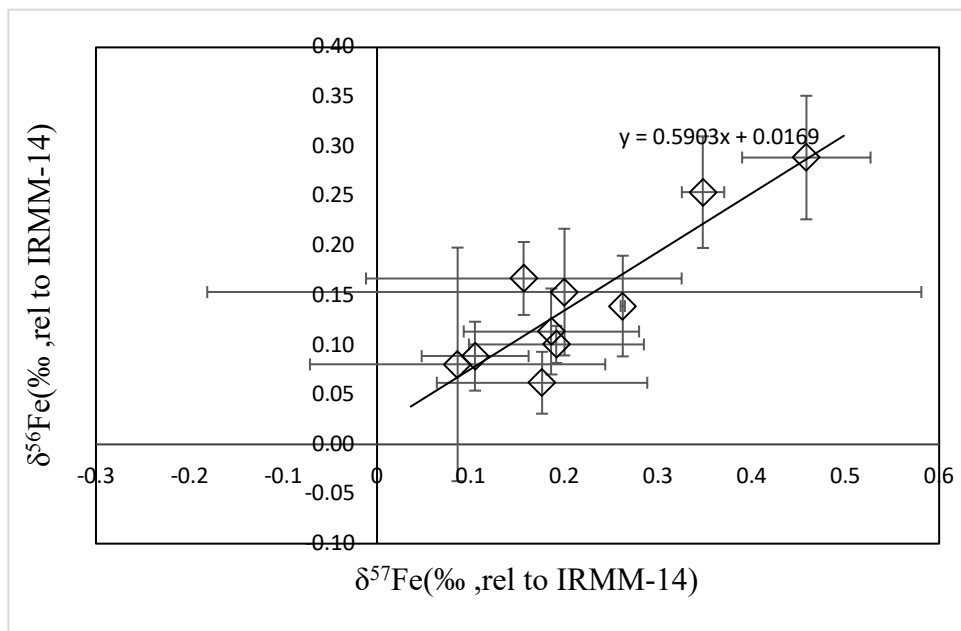
Figure 23 $\delta^{56}Fe$ against $\delta^{57}Fe$ measured by Nu 1700 MC-ICPMS at UBC for selected iron meteorites including Lovina

We obtain $\delta^{57}Fe$ values ranging from 0.09 ± 0.16‰ (KE-MC 201709-02, 2SD, n=3) to 0.20 ± 0.38‰ (Gheriat 004, 2SD, n=3). Two aliquots of Lovina were purified separately at Western and analyzed by MC-ICPMS at UBC during 2 analytical sessions. The $\delta^{57}Fe$ values of two Lovina analyses agree within analytical errors: $\delta^{57}Fe_{Lovina-1}$=0.35 ± 0.02‰ (average and error bars are 2SD calculated from n=2 repeated measurements) and $\delta^{57}Fe_{Lovina-2}$=0.46 ± 0.07‰ (2SD, n=3). Compared with those reported grouped iron meteorites, Lovina shows relatively heavy Ni isotope composition.

The composition of the Filomena individual stone (of the North Chile meteorite used as external matrix-matched and inter-laboratory standard for ICPMS elemental analyses) has δ^{57}Fe of 0.16 ± 0.17‰ (n=2). Poitrasson et al. (2005) reported δ^{57}Fe of 0.08 ± 0.10‰ for North Chile (but we do not know which individual stone was analyzed causing possible sample isotopic heterogeneities); thus, we consider that our data are in agreement within errors with those of Poitrasson et al. (2005).

	δ^{56}Fe		δ^{57}Fe	
	‰	2SD	‰	2SD
1	0.09	0.03	0.10	0.06
2	0.08	0.12	0.09	0.16
3	0.11	0.04	0.19	0.09
4	0.10	0.02	0.19	0.09
5	0.06	0.03	0.18	0.11
NWA 12881	0.14	0.05	0.26	0.00
Gheriat	0.15	0.06	0.20	0.38
Lovina-1	0.25	0.06	0.35	0.02
Lovina-2	0.29	0.06	0.46	0.07
Filomena	0.17	0.04	0.16	0.17

Table 15 A table showing Fe isotope compositions of 6 study meteorites and Lovina.

Chapter 4

4 Discussion

4.1 Comparison with literature studies

4.1.1 Ni concentration

The geochemistry of the rock, soil, and water samples is summarized in Table 7, Table 8 and Table 10 in Chapter 3. Figure 24 shows a comparison of Ni concentration data from literature and this study for different types of samples. ICPMS analysis indicates that the peridotite bedrock samples exhibit a consistent concentration range in Ni (0.12% ~ 0.32% with an exception of extremely high Ni content of 3.1%), and the average Ni concentration of all unmineralized bedrock samples is 0.68 ± 2.41% (2SD, n=6). In comparison with other studies, the Ni contents in peridotite bedrock samples are generally in agreement with those bedrocks studied by Gall et al. (2017) (0.25 ± 0.06%, n=3), Ratié et al. (2015) (0.26 ± 0.07%, n=4), Gueguen et al. (2013) (0.22 ± 0.01%, n=5), Estrade et al. (2015) (0.31 ± 0.15%, n=2).

Ultramafic (UM) soil is the soil derived from weathering of peridotite and serpentinites. The only UM soil sample collected from the top part of limonite zone in this study has a Ni concentration of 0.63%. Two literature studies (Ratié et al. 2015; 2019) have reported significantly higher Ni contents for soils collected from ultramafic complex in Brazil (1.0 ~ 1.9%) than our study based on samples from two ophiolite zones in the Philippines. However, Estrade et al. (2015) and Pedziwiatr et al. (2018) investigated samples collected from ultramafic soils in Albania and from Lower Silesia respectively and reported much lower Ni contents (0.1 ~ 0.4%; 0.08 ~ 0.2%, respectively). It might be because of the different weathering degrees.

Laterite samples which were collected from limonite zones from this study have Ni contents ranging from 0.55% to 1.8% with an average of 1.1 ± 0.8%. Gall et al. (2013) reported Ni concentration of 1.0% for a yellow laterite from a Columbia Ni-laterite mine. Spivak-Birndorf et al. (2018) also reported a yellow laterite Ni concentration of 0.86% for a laterite profile near Democrat, North Carolina, USA. Ratié et al. (2015) reported Ni

concentrations of 0.54% to 5.2% for Brazilian laterite zone samples. Our Philippine laterite samples have consistent Ni contents with these three published studies.

The Ni contents of the saprolite samples range from 1.4% to 2.1% with an average value of 1.6 ± 0.6% (2SD, n=4). Ratié et al. (2015) also analyzed Ni concentrations of samples collected from saprolite zones in Brazil, exhibiting a range between 1.7% and 2.6%. We find similar Ni contents of saprolite samples with Ratié et al. (2015).
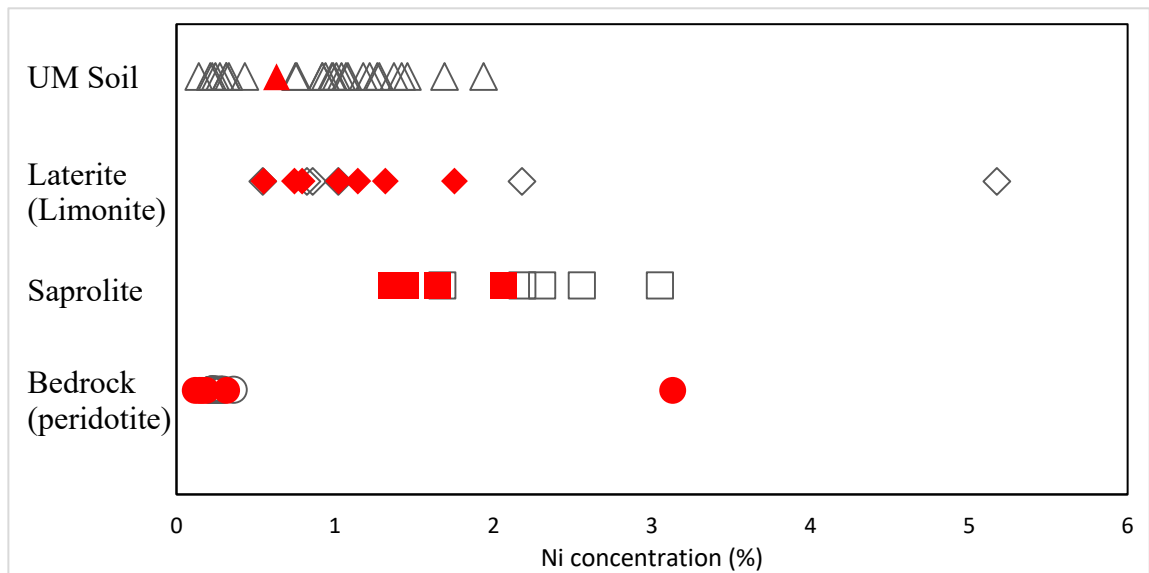
Figure 24 Comparison of Ni contents in soil, laterite, saprolite and bedrock samples from this study and literature. Data reported from this study are marked by red-filled symbols. Literature data are marked by open symbols. Literature data are compiled from Gall et al., 2013; 2017; Gueguen et al. 2013; Estrade et al., 2015; Ratié et al., 2015; 2019; Spivak-Birndorf et al. 2018; Pedziwiatr et al. 2018.

4.1.2   Ni isotope compositions

The six bedrock samples were taken from the bottom part of the weathering lateritic profile of four different Ni mining pits, where primary mineral structures were preserved. Several studies have reported δ^{60}Ni values of peridotites, such as -0.08 ± 0.07‰ for DTS-1, 0.15 ± 0.07‰ for NHM-1, 0.14 ± 0.06‰ for PCC-1 (Gall et al. 2017); -0.07 ± 0.05‰ for DTS-1, 0.12 ± 0.05‰ for PCC-1 (Gueguen et al. 2013); -0.07 ± 0.01‰ for DTS-1, 0.17 ± 0.05‰ for PCC-1 (Chernonozhkin et al. 2015); and 0.08 ± 0.06‰ for a

unweathered protolith collected from Cerro Matoso Ni-laterite mine, Colombia (Gall et al. 2013). Cameron et al. (2009) reported a relatively high delta value of Ni isotope composition of PCC-1, which is 0.34 ± 0.08‰. For the 6 peridotite bedrock samples, we obtain a range from -0.99 ± 0.05‰ to 0.48 ± 0.07‰ with an average value of -0.03 ± 0.99‰ (2SD, n=6). E-B-10C is the peridotite sample with lowest $\delta^{60}Ni$ value (-0.99 ± 0.05‰), and it is the most altered peridotite bedrock sample. Other peridotite bedrock samples with different degrees of alteration all show positive $\delta^{60}Ni$ values ranging from 0.03 ± 0.07‰ to 0.48 ± 0.07‰. The published $\delta^{60}Ni$ values for peridotite fall in the range of our samples. Nickel is hosted by goethite and serpentine group minerals in the peridotite. The wide Ni isotope composition range of peridotite bedrock samples in this study may be due to various alteration degrees.

In addition to peridotite data, Gall et al. (2013) reported Ni isotope compositions data of yellow laterite and green saprolite which were collected from the same pit with their peridotite. The yellow laterite sample showed $\delta^{60}Ni$ of -0.11 ± 0.09‰, whereas the green saprolite sample showed $\delta^{60}Ni$ of -0.30 ± 0.08‰. Another recent study reported a similar $\delta^{60}Ni$ with Gall et al. (2013) for yellow laterite, which is -0.12 ± 0.06‰ (Spivak-Birndorf et al. 2018). Our results also show all negative $\delta^{60}Ni$ values for laterite samples with a wide range from -0.56 ± 0.03‰ to -0.09 ± 0.07‰ with an average $\delta^{60}Ni$ of -0.22 ± 0.34‰ (2SD, n=7). For the saprolite samples, we obtain $\delta^{60}Ni$ values ranging from -0.90 ± 0.06‰ to 0.11 ± 0.02‰ with an $\delta^{60}Ni$ average value of -0.19 ± 0.75‰ (2SD, n=6). Our saprolite samples results indicated similar Ni isotope compositions with the reported data (Gall et al. 2013).
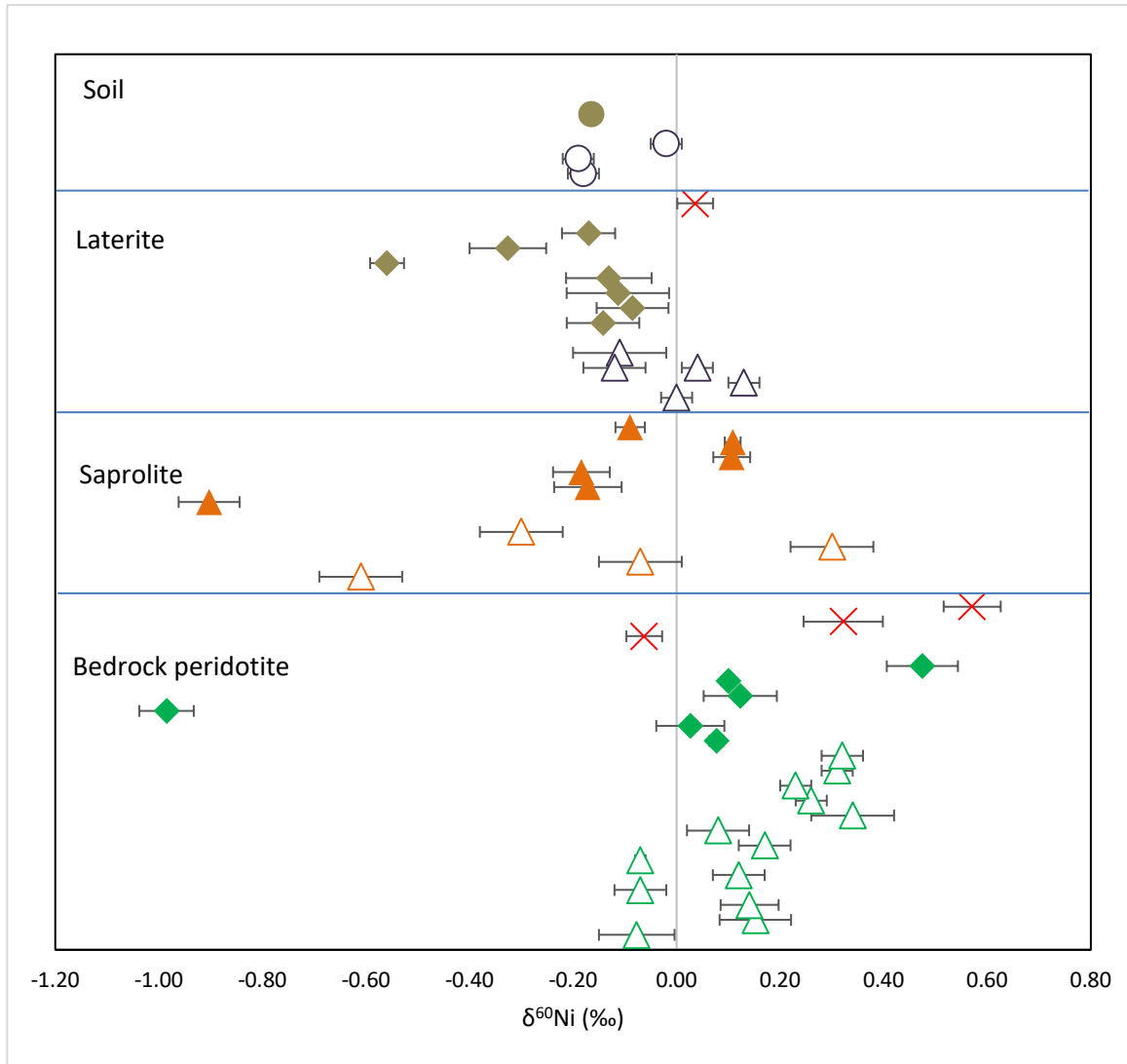
Figure 25 Ni isotope compositions in soil, laterite, saprolite, bedrock zones (closed color symbols) and mineralized samples (crossed symbols) from this study and literature (open symbols: Gall et al. 2013; 2017; Gueguen et al. 2013; Chernonozhkin et al. 2015; Cameron et al. 2009; Ratié et al. 2015; Li et al. 2017; Spivak-Birndorf et al. 2018). Error bars are 2SD.

4.1.3 Fe isotope compositions

Li et al. (2017) reported $\delta^{56}Fe$ of $-0.03 \pm 0.02‰$ for the peridotite sample from the Surigao profile, Philippines. They also reported $-0.03 \pm 0.02‰$ to $0.10 \pm 0.04‰$ with an average of $0.02 \pm 0.06‰$ (2SD, n=20) for other laterite samples collected from a

maximum depth of 6.8m. We obtained unmineralized peridotite δ^{56}Fe from 0.01 ± 0.08‰ to 0.03 ± 0.18‰ with an average of 0.03 ± 0.06‰ (2SD, n=3). The two Philippines saprolite samples show δ^{56}Fe of 0.02 ± 0.17‰ (B-S-14) and 0.05 ± 0.10‰ (E-S-10B). The δ^{56}Fe range of samples from laterite profile is very limited, and our values of both peridotite and saprolite samples are consistent with the values reported by Li et al. (2017) (Figure 26). Iron isotope compositions will be further discussed in section 4.3.5.
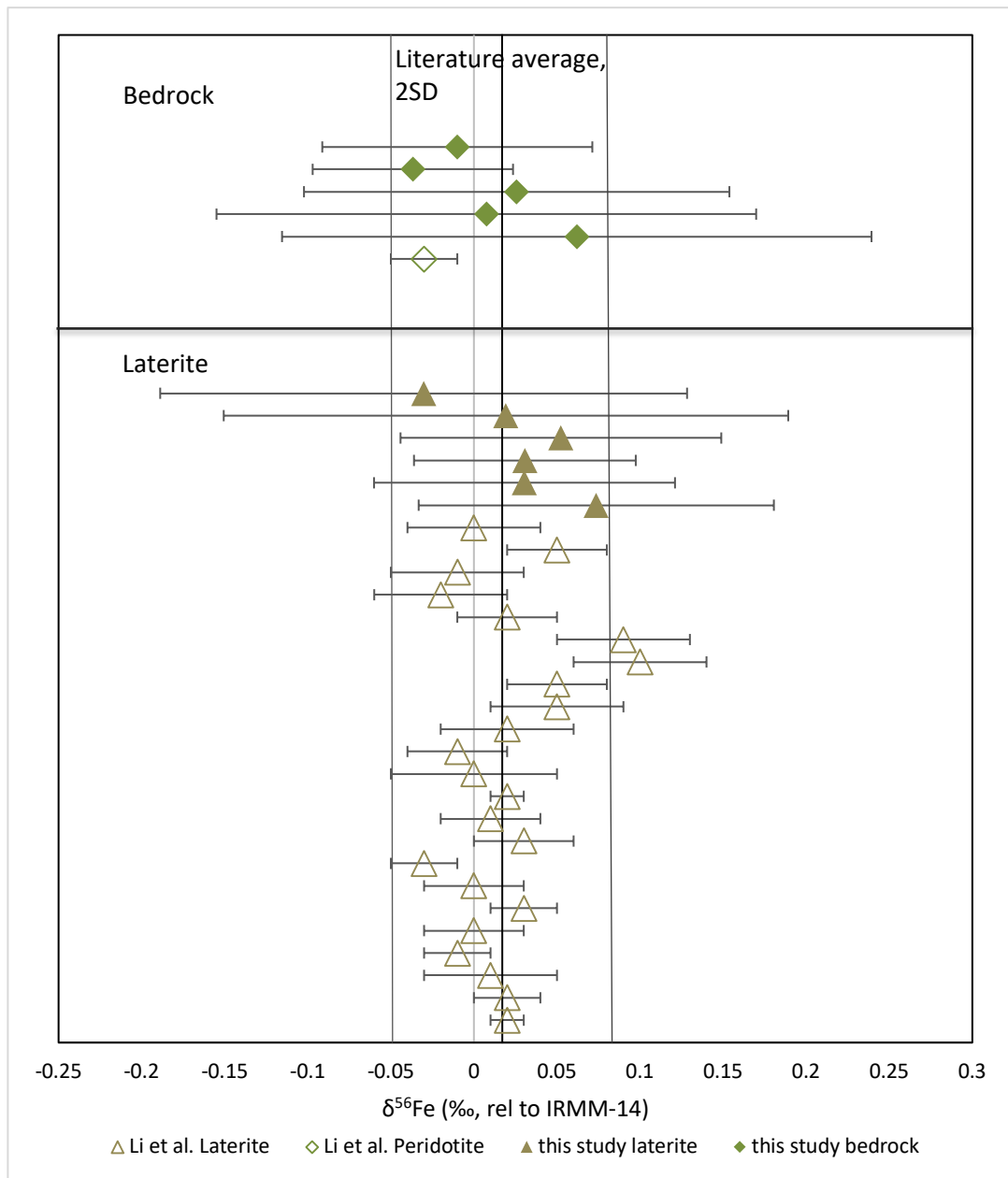
Figure 26 Fe isotope compositions in soil, laterite, saprolite and bedrock zones from this study (closed color symbols) and from Li et al. (2017) (open symbols). Error bars are 2SD.

4.2 Bulk elemental distribution

Peridotite bedrocks are the primary rock type of a laterite profile. Zones above bedrocks (e.g. saprolite zone, limonite zone, and topsoil zone) are the weathering products formed

at different stages. The higher the stratigraphy is located, the longer weathering the zone has experienced. Thus, the topsoil is the most weathered part among the laterite profile. The results showed that mineralized samples (1.77 ± 2.64%, 2SD, n=4), unmineralized saprolite (1.63 ± 0.63%, 2SD, n=4), laterite (1.05 ± 0.81%, 2SD, n=7), unmineralized bedrock (0.68 ± 2.41%, 2SD, n=6) and soil (0.63%, n=1) have decreasing Ni contents (Figure 27). We can assume that the groundwater released Ni from the primary minerals and brought Ni moving downward. Nickel was adsorbed to newly-formed minerals below the original elevation. Elias (2002) modelled a schematic laterite profile (Figure 5) developed for ultramafic rocks weathered under tropical climate highlighting typical changes in chemical compositions. The top zone, which is called 'ferricrete' zone, contains less than 0.6% Ni and less than 0.1% Cu; the underlain layer limonite zone contains Ni concentrations ranging from 0.8% to 1.5% and Cu concentrations ranging from 0.1% to 0.2%; the saprolite zone beneath has Ni concentrations from 1.5% to 3% and Cu concentrations from 0.02% to 0.1%; the least weathered zone bedrock contains Ni concentrations of ~0.3% and Cu concentrations of ~0.01%. The Ni concentrations of the samples of this study (see detail in Table 8 in Chapter 3) generally agreed with the model from Elias (2002). Ratié et al. (2015) also reported a 0.22% to 0.28% Ni concentrations for bedrock samples which were collected from an ultramafic complex of Barro Alto in Brazil. These Ni concentrations are similar to the number reported in Elias (2002), and they also fall in the range of data obtained in this study.

Our peridotite bedrock samples (with average Fe_2O_3 concentration of 8.32 ± 3.36%, 2SD, n=6) and mineralized samples (with average Fe_2O_3 concentration of 9.52 ± 8.64%, 2SD, n=4) are not enriched in Fe compared to saprolite (with average Fe_2O_3 concentration of 34.52 ± 45.15%, 2SD, n=4), laterite (limonite zone) (with average Fe_2O_3 concentration of 62.06 ± 25.41%, 2SD, n=7), and top soil samples (with an Fe_2O_3 concentration of 62.18%). This result is in agreement with the model established by Elias (2002). Similar to Fe, the Ni contents of bedrock zone samples are also very low. Cu is enriched in saprolite zone with an average Cu concentration of 181 ppm; however, Cu is poor in bedrock zone with an average of 26 ppm. Cu contents decrease in the sequence of saprolite zone, laterite (limonite) zone, topsoil, mineralized samples and bedrock samples. In addition to Ni, Fe and Cu, Cr and Mn are also very enriched in the laterite

profile. Cobalt and Mn mainly concentrated in the laterite (limonite) zone with an average concentration of 0.12% and 0.80% respectively.
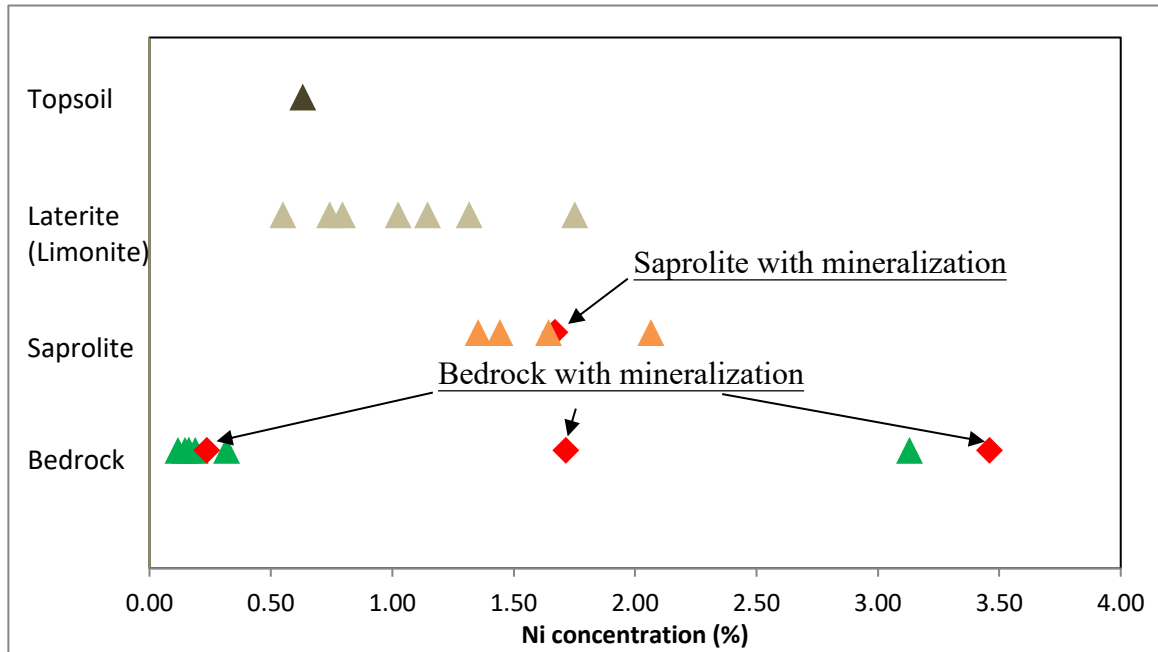
Figure 27 Ni concentrations of different sample types from this study. Red symbols represent mineralized samples (defined as with visible goethite or garnierite).

4.3 Links between mineralogy and isotope compositions

4.3.1 Ni fractionation during the adsorption to newly-formed minerals

Samples E-L-10A, E-S-10B, E-B-10C and E-B-10D were collected from the same laterite profile; thus, they can be used to study the fractionation processes along the laterization processes. Except for the unaltered bedrock, E-B-10D, other 3 samples show a pattern that Ni isotope compositions become lighter as depth increases. Because E-L-10A (with Ni concentration of 1.0%, δ^{60}Ni of -0.17 ± 0.05‰), E-S-10B (with Ni concentration of 2.1%, δ^{60}Ni of -0.90 ± 0.06‰) and E-B-10C (with Ni concentration of 3.1%, δ^{60}Ni of -0.99 ± 0.05‰) show increasing Ni contents and lighter Ni isotope compositions, we propose that Ni enrichment has a preference for light Ni in the solid phase as groundwater was transferred to further depth in the laterite profile. Thus, the possible explanation for the phenomena is that Ni adsorption preferred light Ni isotopes

to heavy isotopes during the laterization processes. Among all the samples analyzed in this study, the river water sample has the heaviest Ni isotope compositions ($\delta^{60}Ni_{water}$=0.95 ± 0.10‰). This may have suggested that the leaching process and Ni adsorption to Fe- and Mg-oxides minerals might be the controlling mechanisms of Ni fractionation during weathering processes in tropical area laterite profile. However, a recent research has ruled out olivine leaching process as a driving mechanism of Ni fractionation (Spivak-Birndorf et al. 2018). We thus instead infer that the Ni isotopic fractionation process takes place during the precipitation of Fe oxide (goethite) and replacement of Mg during serpentinization, when light Ni isotopes prefer to incorporate into newly-formed minerals, leaving the heavier Ni isotopes in groundwater.
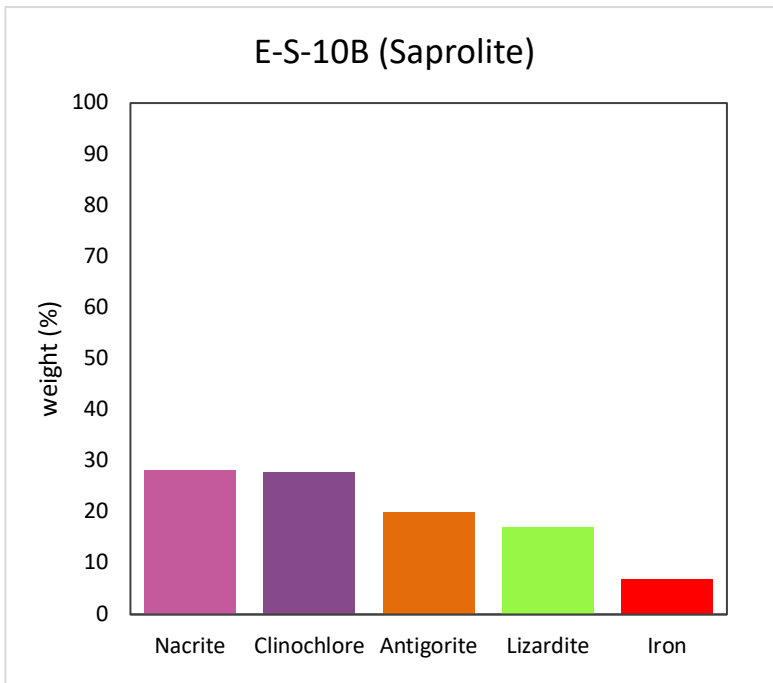
Figure 28 XRD results of E-S-10B (provided by Dr. Christian Schardt, phase proportions are determined by MDI JADE).
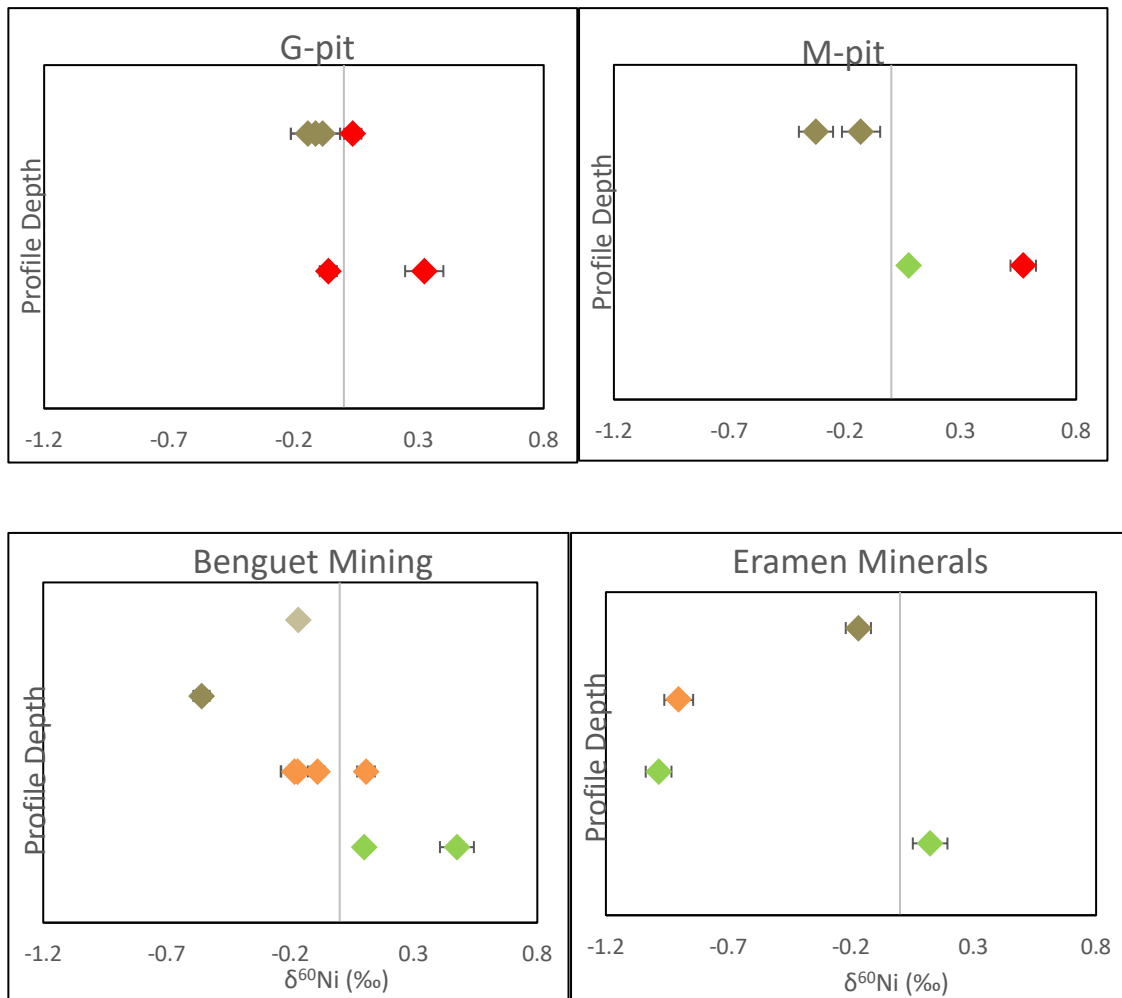
Figure 29 Figures showing stratigraphically Ni isotope variations of 4 mining areas in the Philippines. The light brown symbol represents soil; dark brown symbols represent laterite samples; orange symbols represent saprolite samples; green symbols represents bedrock samples; red symbols represent mineralized samples.

4.3.2 Ni enrichment during alteration of bedrocks

Several literature studies have reported Ni isotope compositions of ultramafic bedrocks, ranging from -0.08‰ to 0.34‰ (Gall et al. 2013; 2017; Gueguen et al. 2013; Chernonozhkin et al. 2015; Cameron et al. 2009; Ratié et al. 2015). Bulk silicate earth has the $\delta^{60}Ni$ value of 0.23 ± 0.06‰ (Gall et al. 2017). Having analyzed 6 bedrock samples collected from 4 different areas, we report a wide range of $\delta^{60}Ni$ values from 0.03 ± 0.07‰ to 0.47 ± 0.07‰ with an extremely low value of -0.99 ± 0.05‰ for

ultramafic bedrocks. E-B-10C is a highly altered bedrock, while other 3 bedrock samples are less altered. Samples E-B-10C and E-B-10D are from the same laterite profile. E-B-10C was collected at a higher location and experienced a higher degree of alteration than E-B-10D. E-B-10C (δ^{60}Ni = -0.99 ± 0.05‰) displays a significantly lighter Ni isotope composition than E-B-10D (δ^{60}Ni = 0.12 ± 0.07‰). We do not have the mineral assemblages of E-B-10C and E-B-10D to compare with the geochemical characteristics. However, Ni is enriched in E-B-10C (with a Ni content of 3.1%) compared to E-B-10D (with a Ni content of 0.19%). Thus, this result supports that Ni adsorption associated with the alteration of olivine preferentially captures light Ni isotopes from the groundwater to the new mineral lattice of the secondary phases formed.

4.3.3   Ni fractionation associated with bedrock mineralization

The Ni geochemistry and mineral assemblages of limonite and saprolite laterite ores from Pujada in the Philippines indicated that Ni is enriched in the limonite zone throughout substitution for Mn in the MnO_6 layers and replacement of Fe into goethite (Fan and Gerson 2011). In the saprolite zone, most Ni is associated with replacement of Mg in serpentine minerals, such as lizardite, and the remaining Ni is associated with vacancies occupation of Ni in the MnO_6 layers (Fan and Gerson 2011).

The XRD analysis of unmineralized bedrock sample B-B-15B and the mineralized bedrock sample M-M-5 (Figure 30), indicate that an extensive alteration happened which led to the formation of antigorite, a serpentine group mineral. δ^{60}Ni of mineralized bedrock sample, M-M-5, shows heavier Ni isotope composition (δ^{60}Ni = 0.57 ± 0.06‰) than that of the unmineralized bedrock sample collected from the same pit, M-B-7 (δ^{60}Ni = 0.08 ± 0.01‰), and the unmineralized bedrock sample, B-B-15B (δ^{60}Ni = 0.47 ± 0.07‰). M-M-5 also displays a significantly higher Ni concentration (3.46%) than M-B-7 (0.16%) and B-B-15B (0.32%). The formation of antigorite accompanying the enrichment in Ni demonstrates that serpentinization process occurred during mineralization processes, and that the replacement of Mg was preferentially associated with heavy Ni isotopes in the newly-formed serpentine group minerals (e.g., antigorite and lizardite). It could be the result of either serpentine group mineral prefers heavy Ni

isotopes during the precipitation, or heavy Ni isotope is enriched in groundwater from where the new minerals extract Ni.

The following reaction shows the replacement of Mg in the form of lizardite with Ni (Butt and Cluzel 2013):

$$Mg_3Si_2O_5(OH)_4 + 3\ Ni^{2+} = Ni_3Si_2O_5(OH)_4 + 3\ Mg^{2+}$$
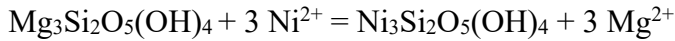
Lizardite   Ni-lizardite
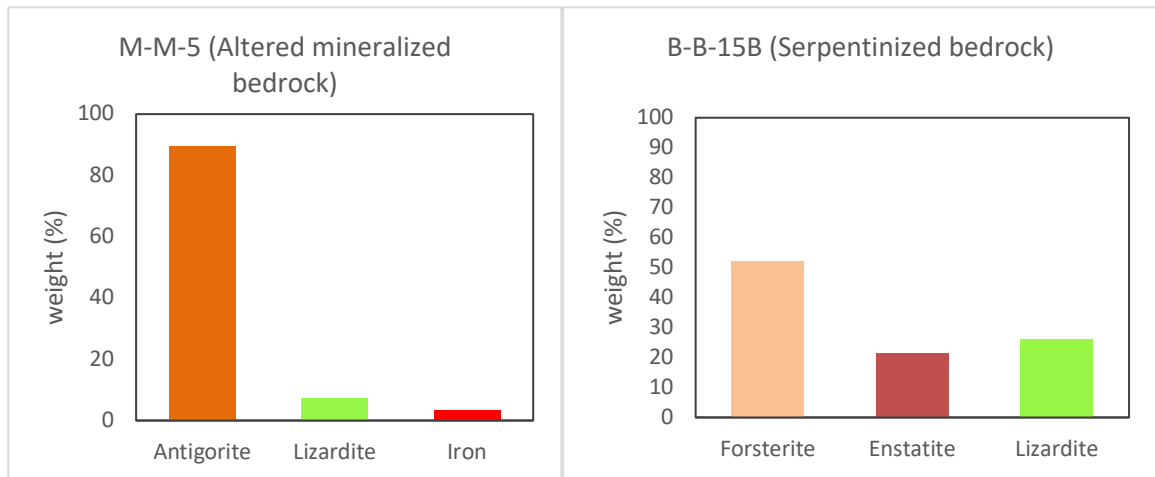
Figure 30 XRD results of M-M-5 and B-B-15B (provided by Dr. Christian Schardt, phase proportions are determined by MDI JADE).

4.3.4   Replacement of goethite by hematite

Samples E-L-10A and M-L-6 show replacement of goethite ($Fe(O)(OH)$) by hematite (Fe_2O_3) (Lemine 2014) with:

$$2\ Fe(O)(OH) = Fe_2O_3 + H_2O$$
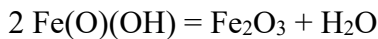
According to the model (Elias, 2002) described in Chapter 1, Ni is leached out from olivine, serpentinized olivine, and pyroxene to groundwater at the beginning stage. Then, Ni is adsorbed from groundwater to newly formed goethite, smectite and other Mn oxides. Limonite zone can be subdivided into two types, 'yellow limonite' for the lower part and 'red limonite' for the upper part. 'Red limonite' formed due to the replacement

73

of goethite by hematite. The transition to hematite usually involved loss of Ni as hematite cannot hold Ni anymore. Samples M-L-6 and E-L-10A contain different mineral assemblages even though both of them were from limonite zone (Figure 29). Up to 96.8% of goethite and 3.2% quartz in the M-L-6 demonstrate that nearly all primary and secondary minerals have been replaced by goethite which host Ni released from olivine and serpentinized olivine. Hematite is shown in E-L-10A which indicated that a portion of goethite was replaced by hematite. The bulk chemistry results also confirm the loss of Ni in E-L-10A with the fact that E-L-10A has lower Ni content (1.02%) than M-L-6 (1.75%). Thus, their Ni isotope composition is valuable for determining Ni fractionation during the hematite replacement process. The fact that E-L-10A (δ^{60}Ni = -0.17 ± 0.05‰) is in accordance with M-L-6 (δ^{60}Ni = -0.13 ± 0.08‰) within error indicates that Ni isotope fractionation is very small during goethite dehydration.
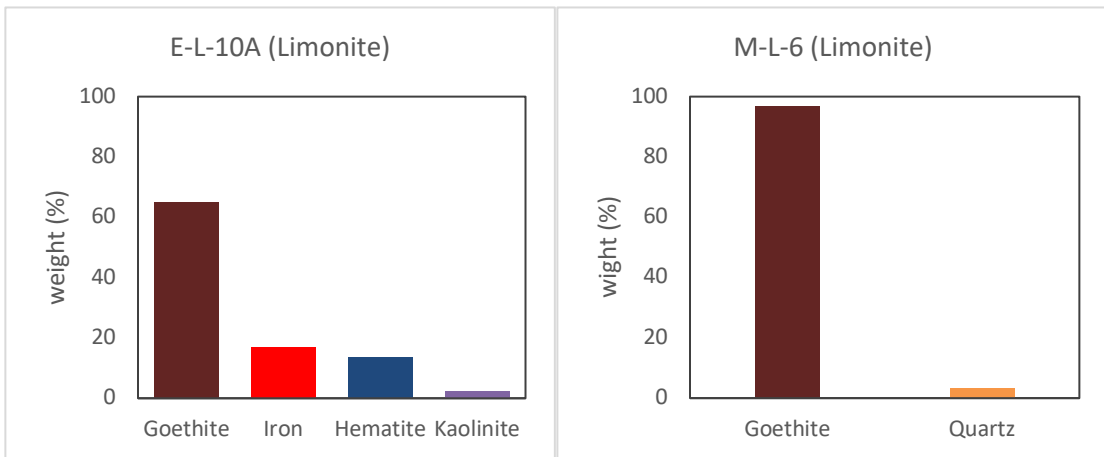
Figure 31 XRD results of E-L-10A and M-L-6 (provided by Dr. Christian Schardt, phase proportions are determined by MDI JADE).

4.3.5   Fe isotope compositions of laterite profile

As shown in Figure 32, Fe is enriched in upper layers (laterite, saprolite, and soil) than lower layers (mineralized and unmineralized bedrock) in a laterite profile. Despite the large individual internal errors of the measurements, there is no large δ^{56}Fe variation beyond 0.4‰. The average δ^{56}Fe of all selected samples is 0.02 ± 0.07‰ (2SD, n=11).

This is still an important, and surprising, result compared with the Ni systematics of the same samples. The dissolution of solids and sorption to particle surface should result in large Fe isotope fractionation (Yesavage et al. 2012). Also, many studies have found large Fe isotope fractionation effects in soils with $\delta^{56}Fe$ from $-0.62‰$ to $+0.72‰$ (Fantle and DePaolo 2004; Emmanuel et al. 2005; Thompson et al. 2007; Wiederhold et al. 2007; Yamaguchi et al. 2007). Poitrasson et al (2008) studied laterites formed from a granodiorite intrusion in Cameroon, and Li et al. (2017) investigated the laterite profile developed from the weathering of peridotites in south Philippines. Both of the studies found surprising limited Fe isotope fractionation developed with laterite profiles. This research had access to stratigraphic samples of four laterite profiles in the Philippines and achieved relatively comprehensive Fe isotopic data of laterite profiles. Unlike the lack of redox state changes for Ni, redox transformation and transportation of a portion of Fe should lead to significant Fe isotope fractionation. As discussed for Ni isotope fractionation effects above, replacements of Fe by Ni occurred along the laterite profile. It is not clear why Fe isotope fractionation is quite limited among all types of samples. Li et al. (2017) suggested that Fe should have experienced a complete and in situ oxidation before migration and Fe was transferred in the form of colloidal substances. A possible reason for this is that Fe remains in its oxidized form in laterite profiles without major redox changes (Poitrasson et al. 2008). Also, pH condition of groundwater is required to be very low to dissolve Fe^{3+}; thus, mobilization of Fe^{3+} is limited (Li et al. 2017). Studies which found large Fe isotope fractionation studied soils where Fe can be dissolved by water and organic acids or oxides were partially reduced (Emmanuel et al. 2005; Fantle and DePaolo 2004).
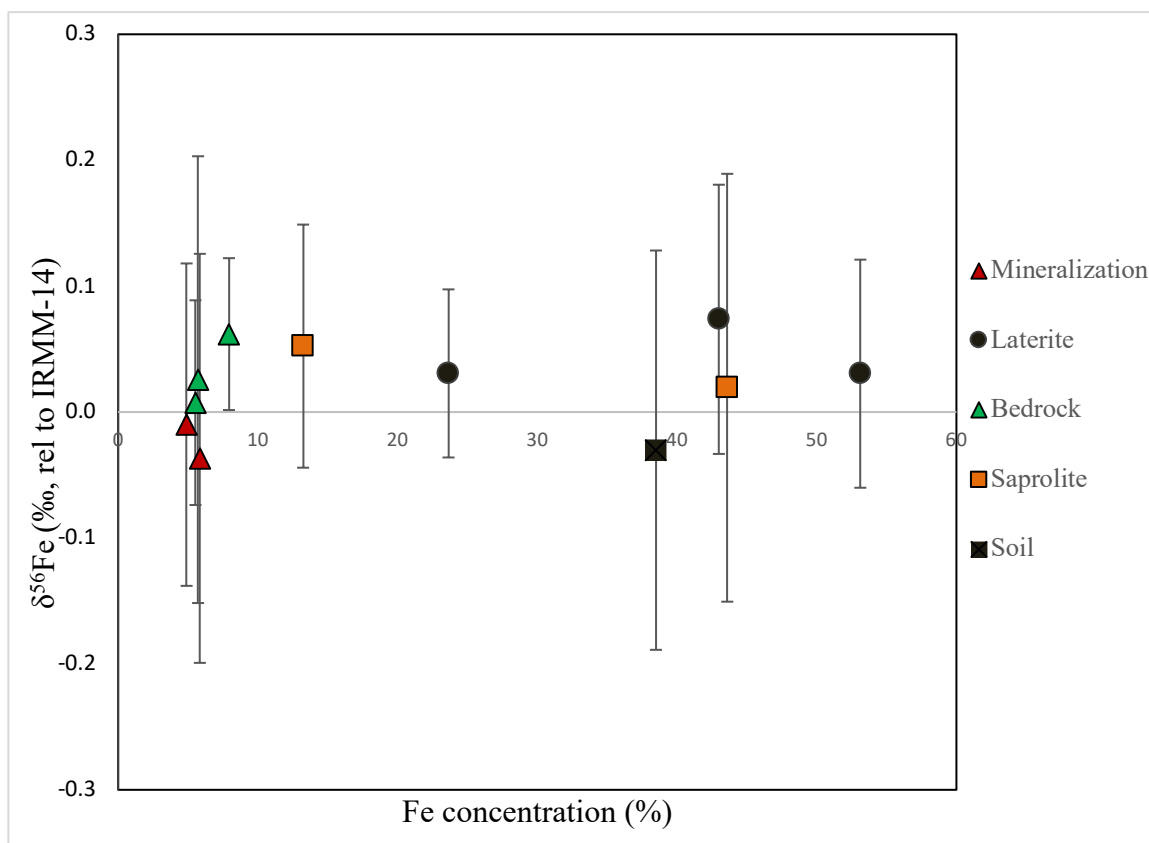
Figure 32 Fe isotopic compositions (rel. to IRMM-14) show the isotopic variation among water, bedrock, limonite laterite, saprolite, topsoil and mineralized bedrock samples.

4.4   Conclusions on weathered samples

Stratigraphic Ni elemental abundance and Ni isotope compositions of laterite profiles were measured combined with Fe isotopic systematics. Iron elemental abundance and Fe isotope compositions of selected samples from laterite profile in the Philippines were also obtained. Large Ni isotope fractionation was observed during the laterization processes, but Fe isotope fractionation was not detected within our analytical precision.

Measurements of geological rock and mineral standards, duplicated samples, and international isotopic standard indicate that the Ni and Fe elemental purification chemistry protocols, Ni double spike corrections and mass spectrometric measurements applied in this study are reliable and reproducible between different analytical sessions.

This research found that the Ni isotopic fractionation happened during the precipitation of Ni-enriched minerals (goethite and garnierite), when light Ni isotopes prefer to incorporate into newly-formed Fe-oxides, leaving heavy Ni isotopes in water. $\Delta^{60}Ni_{Limonite-Bedrock}$ is up to $-0.19 \pm 0.32‰$. In addition, Ni adsorption caused by alteration of olivine preferentially capture light Ni from groundwater into lattice as well. Also, this study found that Ni isotope fractionation during goethite dehydration process was very limited. However, mineralized samples show heavy Ni isotopes as groundwater where Ni comes from is enriched in heavy Ni isotopes. Having known that the heavy Ni isotopes prefer the dissolved phase and light Ni isotopes prefer the solid phase, Ni isotope analysis might be useful for Ni mining exploration in future as an indicator of Ni mobilization. This could also become a useful tool to detect evidence of past aqueous weathering processes on Earth or other planets.

4.5   Fe isotope and meteorites

The Fe isotopic compositions of iron meteorites obtained in this study are presented together with literature data (Poitrasson et al. 2005; Williams et al. 2006) in Figures 33. Detailed $\delta^{57}Fe$ values are listed in the Results chapter 3 (Table 15). Five KE meteorites, NWA 12881 and Gheriat 004 agree with the reported $\delta^{57}Fe$ values of corresponding group iron meteorites data (Figure 33). The composition of Lovina ataxite ungrouped iron meteorite is $\delta^{57}Fe_{Lovina} = 0.41 \pm 0.16‰$ (from 2 repeated individual sample processing and measurements; Table 15). Lovina has a much higher $\delta^{57}Fe$ value than any iron meteorites reported so far except IIAB. However, Lovina has much higher Ni concentration (34.5%) than IIAB group Fe meteorites (5.3 to 6.4%) (Figure 20 and Figure 21). The IVB group is the closest iron meteorite group to ataxites with very high Ni (>10% Ni) and similarly very low Au contents in iron meteorites (<0.5ppm), therefore the closest group to compare with the geochemistry and Fe isotopic composition of Lovina.

The micro-XRD analysis of Lovina reports (Connelly et al., 2008; Flemming et al., 2008) that there is taenite (Ni-rich alloy) but no kamacite (low-Ni alloy). Ni-rich awaruite (Ni_3Fe) was also observed together with taenite (Flemming et al., 2008). Besides, its bulk

geochemistry analysis result showed the high Ni, very low Au, high Cr and low W concentrations, which are quite unusual among iron meteorites (Connolly et al. 2008).

Pb-Pb isotopic analyses ($^{206}Pb/^{208}Pb$ and $^{207}Pb/^{206}Pb$ were measured) by LA-ICPMS of troilite nodules of Lovina indicate that it has a composition consistent with modern-terrestrial Pb (Stacey and Kramers, 1975), clearly distinct from the Pb isotopic composition of the Canyon Diablo (iron meteorite) Troilite (CDT) and troilites from other meteorites (Charles, 2013).

Further elemental analyses of highly siderophile element (HSE) coupled with Os isotopic data revealed that Lovina bears no resemblance to any magmatic or non-magmatic irons previously analyzed (Ash et al., 2014).

The concentrations of cosmogenic isotopes such as ^{10}Be, ^{26}Al and ^{36}Cl were measured at levels which are 3 to 4 orders-of-magnitude lower than normal iron meteorites (Nishiizumi and Caffee, 2011). The concentration detected for ^{36}Cl could also be explained by production on Earth if Lovina has been exposed for >100,000 years on the Earth's surface or throughout weathering by sea water in Bali, Indonesia where it was found (if true).

Based on its particular mineralogy, geochemistry, and now contrasted Fe isotopic composition compared to iron meteorites, we find that our results on Lovina also support a terrestrial origin. It may have formed as a result of the reduction process that occurs during serpentinization of terrestrial mantle peridotite. The presence of taenite and troilite in Lovina have been taken indicators of extraterrestrial origin (Flemming et al., 2008). However, troilite can be a native natural mineral on Earth. Also, other evidence of natural terrestrial Fe-Ni alloy is josephinite (terrestrial iron-nickel alloy, not an awerite) which has been found as pebbles formed during serpentinization of peridotites in the Josephine ophiolite in Oregon (Bird and Weathers, 1975). Noble gas isotopic signatures support the formation of josephinites near the Earth's surface. Noble gas data do not favor a deep mantle origin or a formation at the mantle-core boundary (Staudacher and Allègre 1990).
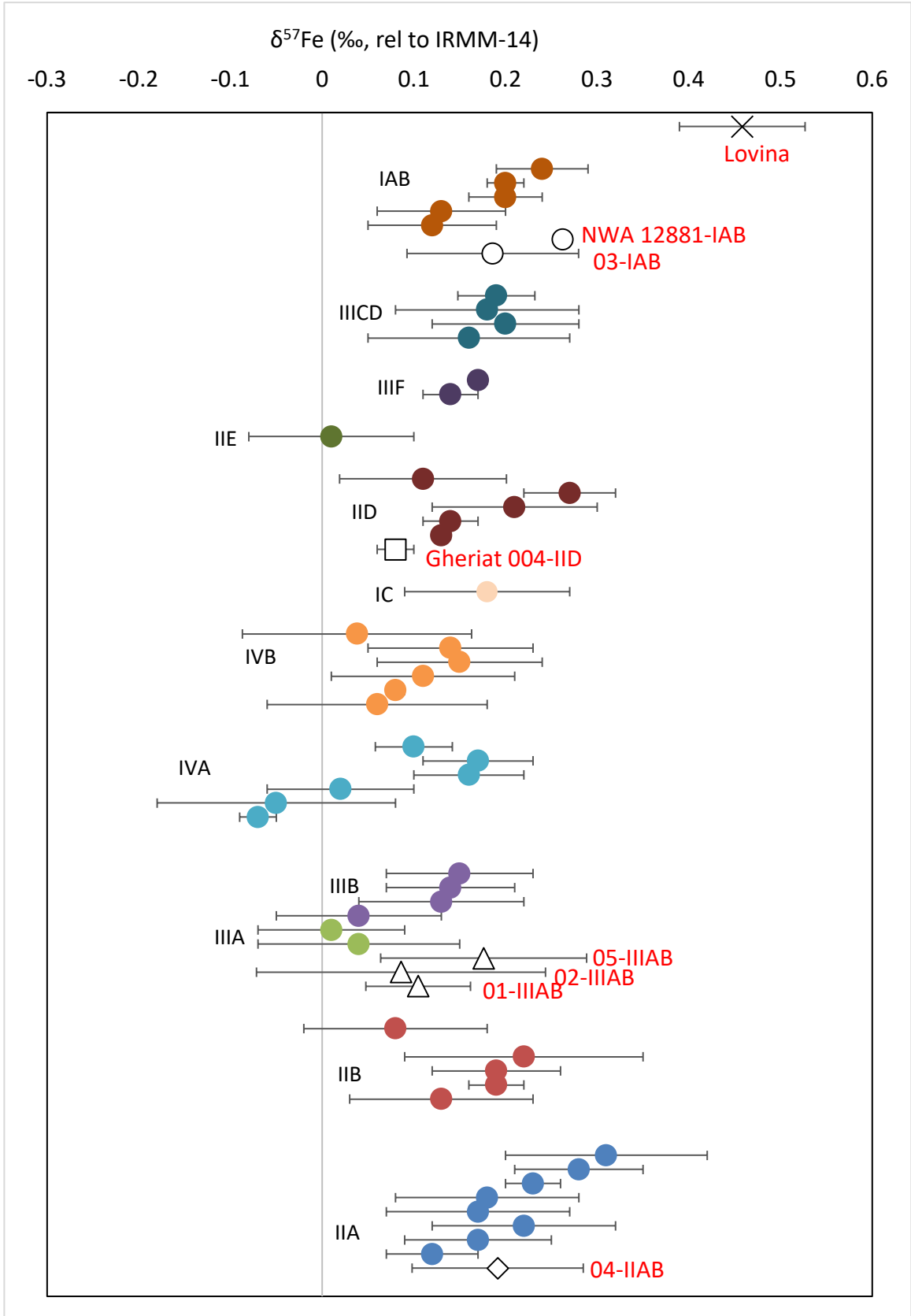
Figure 33 δ^{57}Fe of iron meteorites from this study and literature (Williams et al. 2006; Poitrasson et al. 2005). Literature data are represented by filled symbols, and data from this study are represented by open symbols. Average composition of Lovina from two analyses. Error bars are 2SD.

4.6   Conclusions on meteorite samples

We investigated the trace element compositions and Fe isotope compositions of 6 new iron meteorites, the Filomena stone of North Chile, and the Lovina ungrouped meteorite. Lovina is an unusual 8.2kg alloy which was classified as an ungrouped ataxite meteorite. Its meteoritical origin has been questioned and suggested by recent workers to be instead a terrestrial object (e.g., Nishiizumi and Caffee, 2011). Though its geochemistry pointed to an ungrouped iron meteorite with similarities IVB group meteorites (high Ni, low Au contents), its Fe isotopic composition is higher δ^{57}Fe value than any iron meteorites reported so far. Combining our results with other reported elemental and isotopic analyses, we propose to discredit Lovina as a meteorite. The formation of such large natural alloy on Earth is nevertheless enigmatic and worth further investigations to understand their formation.

References

Archer, C., and Vance, D. 2008. The isotopic signature of the global riverine molybdenum flux and anoxia in the ancient oceans. Nature Geoscience, **1**, 597–600.

Archer, C., Elliott, T., van den Boorn, S., and van Bergen, P. 2012. Mo and Ni isotope systematics in petroleum fluids across subsurface alteration gradients. Mineralogical Magazine, Abs. 1433.

Arndt, N.T., Lesher, C.M., and Czamanske, G.K. 2005. Mantle-derived magmas and magmatic Ni–Cu–(PGE) deposits. Economic Geology, 100th Anniv **5**, 23.

Asael, D., Matthews, A., Oszczepalski, S., Bar-Matthews, M., and Halicz, L. 2009. Fluid speciation controls of low temperature copper isotope fractionation applied to the Kupferschiefer and Timna ore deposits. Chemical Geology, **262**, 147-158.

Ash, R. D., Walker, R. J., Yamakawa, A., and Yin, Q. Z. 2014. New Insights into the Origin of Lovina, a Mystery Metal. In Lunar and Planetary Science Conference, **45**, 1434.

Bekker, A., Barley, M.E., Fiorentini, M.L., Rouxel, O.J., Rumble, D., and Beresford, S.W. 2009. Atmospheric sulfur in Archean komatiite-hosted nickel deposits. Science, **326**, 1086–1089.

Berglund, M., and Wieser, M. E. 2011. Isotopic Compositions of the Elements 2009 (IUPAC Technical Report). Pure and Applied Chemistry, **83**, 397−410.

Bird, J. M., and Weathers, M. S. 1975. Josephinite: specimens from the Earth's core?. Earth and Planetary Science Letters, **28**, 51-64.

Bleeker, W., and Macek, J.J. 1996. Evolution of the Thompson Nickel Belt, Manitoba: setting of Ni–Cu deposits in the western part of the circum Superior boundary zone. Fieldtrip Guidebook Geological Association of Canada Annual Meeting, Winnipeg, Manitoba.

Brand, N.W., Butt, C.R.M., and Elias, M. 1998. Nickel laterites: classification and features. AGSO Journal of Australian Geology & Geophysics, **17**, 81-88.

Butt, C. R., and Cluzel, D. 2013. Nickel Laterite Ore Deposits: Weathered Serpentinites. Elements, **9**, 123-128.

Cameron, V., Vance, D., Archer, C., and House, C.H. 2009. A biomarker based on the stable isotopes of nickel. Proceedings of the National Academy of Sciences, **106**, 10944–10948.

Campbell, A. J., and Humayun, M. 2005. Compositions of group IVB iron meteorites and their parent melt. Geochimica et Cosmochimica Acta, **69**, 4733-4744.

Chapman, J. B., Weiss, D. J., Shan, Y., and Lemburger, M. 2009. Iron isotope fractionation during leaching of granite and basalt by hydrochloric and oxalic acids. Geochimica et Cosmochimica Acta, **73**, 1312-1324.

Chapman, J., Mason, T., Weiss, D., Coles, B., and Wilkinson, J., 2006. Chemical separation and isotopic variations of Cu and Zn from five geological reference materials: Geostandards and Geoanalytical Research, **30**, 5–16.

Charles, C. R. 2013. Pb-Pb isotopic and X-ray tomographic constraints on the origin of chondrules. University of Toronto (Canada).

Chernonozhkin, S. M., Goderis, S., Lobo, L., Claeys, P., and Vanhaecke, F. 2015. Development of an isolation procedure and MC-ICP-MS measurement protocol for the study of stable isotope ratio variations of nickel. Journal of Analytical Atomic Spectrometry, **30**, 1518-1530.

Christoffersen, P. 2017. Stable Cu, Fe, and Ni Isotopic Systematics of the Sudbury Offset Dikes and Associated Rocks. Electronic Thesis and Dissertation Repository. 5179.

Compuesto, J. E. B. 2014. Geology of Southern Palawan (Doctoral dissertation, Faculty of National Institute of Geological Sciences, University of the Philippines, Diliman).

Connolly Jr, H. C., Smith, C., Benedix, G., Folco, L., Righter, K., Zipfel, J., Yamaguchi, A., and Aoudjehane, H. C. 2008. The Meteoritical Bulletin, No. 93, 2008 March. Meteoritics and Planetary Science, **43**, 571-632.

Cook D.L., Wadhwa M., Clayton R.N., Dauphas N., Janney P.E., and Davis A.M. 2007. Mass-dependent fractionation of nickel isotopes in meteoritic metal. Meteoritics and Planetary Science, **42**, 2067–2077.

Cook, D. L., Wadhwa, M., Janney, P. E., Dauphas, N., Clayton, R. N., and Davis, A. M. 2006. High precision measurements of non-mass-dependent effects in nickel isotopes in meteoritic metal via multicollector ICPMS. Analytical Chemistry, **78**, 8477-8484.

Dalvi A. D., Bacon W. G., and Osborne R. C. 2004. The past and the future of nickel laterites. PDAC 2004 International Convention, Trade Show & Investors Exchange, 1–27.

Dauphas, N., John, S. G., and Rouxel, O. 2017. Iron isotope systematics. Reviews in Mineralogy and Geochemistry, **82**, 415-510.

Dauphas, N., Teng, F. Z., and Arndt, N. T. 2010. Magnesium and iron isotopes in 2.7 Ga Alexo komatiites: mantle signatures, no evidence for Soret diffusion, and identification of diffusive transport in zoned olivine. Geochimica et Cosmochimica Acta, **74**, 3274-3291.

Dideriksen, K., Baker, J. A., and Stipp, S. L. S. 2006. Iron isotopes in natural carbonate minerals determined by MC-ICP-MS with a 58Fe–54Fe double spike. Geochimica et Cosmochimica Acta, **70**, 118-132.

Dimalanta, C. B., Salapare, R. C., Faustino-Eslava, D. V., Ramos, N. T., Queaño, K. L., Yumul Jr, G. P., and Yang, T. F. 2015. Post-emplacement history of the Zambales

Ophiolite Complex: Insights from petrography, geochronology and geochemistry of Neogene clastic rocks. Journal of Asian Earth Sciences, **104**, 215-227.

Dreyfus, S., Pécheyran, C., Magnier, C., Prinzhofer, A., Lienemann, C., and Donard, O. 2005. Direct Trace and Ultra-Trace Metals Determination in Crude Oil and Fractions by Inductively Coupled Plasma Mass Spectrometry. Journal of American Society for Testing and Materials International, **2**, 1-8.

Ehrlich, S., Butler, I., Halicz, L., Rickard, D., Oldroyd, A., and Matthews, A. 2004. Experimental study of copper isotope fractionation between aqueous Cu (II) and covellite, CuS. Chemical Geology, **209**, 259–269.

Elias, M. 2002. Nickel laterite deposits – a geological overview, resources and exploitation. Centre for Ore Deposit Research, University of Tasmania, Hobart, Special Publication, **4**, 205-220.

Elliott, T., and Steele, R. C. J. 2017. The Isotope Geochemistry of Ni. In Reviews in Mineralogy and Geochemistry. Edited by F. Z. Teng, J. Watkins and N. Dauphas. 511-542.

Emmanuel, S., Erel, Y., Matthews, A., and Teutsch, N., 2005. A preliminary mixing model for Fe isotopes in soils. Chemical Geology, **222**, 23–34.

Encarnación, J., and Mukasa, S.B., 1997. Age and geochemistry of an 'anorogenic' crustal melt and implications for I-type granite petrogenesis. Lithos, **42**, 1–13.

Encarnación, J., Essene, E.J., Mukasa, S.B., and Hall, C. 1995. High pressure and temperature subophiolitic kyanite-garnet amphibolites generated during initiation of mid-tertiary subduction, Palawan, Philippines. Journal of Petrology, **36**, 1481–1503.

Estrade, N., Cloquet, C., Echevarria, G., Sterckeman, T., Deng, T., Tang, Y., and Morel, J.L. 2015. Weathering and vegetation controls on nickel isotope fractionation in surface ultramafic environments (Albania). Earth and Planetary Science Letters, **423**, 24–35.

Fan, R., and Gerson, A. R. 2011. Nickel geochemistry of a Philippine laterite examined by bulk and microprobe synchrotron analyses. Geochimica et Cosmochimica Acta, **75**, 6400-6415.

Fantle, M. S., and DePaolo, D. J. 2004. Iron isotopic fractionation during continental weathering. Earth and Planetary Science Letters, **228**, 547–562.

Fekiacova, Z., Pichat, S., Cornu, S., and Balesdent, J. 2013. Inferences from the vertical distribution of Fe isotopic compositions on pedogenetic processes in soils. Geoderma, **209**, 110-118.

Flemming, R. L., McCausland, P. J. A., Kissin, S. A., Corcoran, P. L., and Biesinger, M. C. 2008. Lovina, a New Ataxite: Examination by μXRD, Petrography, SEM and INAA. In Lunar and Planetary Science Conference, **39**, 2412.

Flemming, R. L., McCausland, P. J., Kissin, S. A., Corcoran, P. L., Biesinger, M. C., McIntyre, N. S., Fuller, M. L. and Feng, R. 2009. May. The unusual Lovina Ataxite: Examination of Meteoritic Microstructures and Terrestrial Weathering by muXRD, Petrography, SEM, INAA and sXRF. In AGU Spring Meeting Abstracts.

Fourie, P., Ferreira, D., and Mapleson, D. 2009. NI43-101 Technical Report, May 2009, Alpha Nickel Project, Palawan Island, Philippines.

Gall, L., Williams, H. M., Halliday, A. N., and Kerr, A. C. 2017. Nickel isotopic composition of the mantle. Geochimica et Cosmochimica Acta, **199**, 196-209.

Gall, L., Williams, H. M., Siebert, C., Halliday, A. N., Herrington, R. J., and Hein, J. R. 2013. Nickel isotopic compositions of ferromanganese crusts and the constancy of deep ocean inputs and continental weathering effects over the Cenozoic. Earth and Planetary Science Letters, **375**, 148-155.

Gall, L., Williams, H., Siebert, C., and Halliday, A. 2012. Determination of mass-dependent variations in nickel isotope compositions using double spiking and MC-ICPMS. Journal of Analytical Atomic Spectrometry, **27**, 137-145.

Gattacceca, J., Bouvier, A., Grossman, J., Metzler, K., and Uehara, M. 2019. The
Meteoritical Bulletin, No. 106. Meteoritics & Planetary Science, **54**, 469-471.

Golightly, J.P. 1981. Nickeliferous laterite deposits. Economic Geology, 75th
Anniversary Volume. 710-735.

Goss, C. J. 1987. The kinetics and reaction mechanism of the goethite to hematite
transformation. Mineralogical Magazine, **51**, 437-451.

Gramlich, J. W., Machlan, L. A., Barnes, I. L., and Paulsen, P. J. 1989. Absolute isotopic
abundance ratios and atomic weight of a reference sample of nickel. Journal of
Research of the National Institute of Standards and Technology, **94**, 347.

Gueguen, B., Rouxel, O., Ponzevra, E., Bekker, A., and Fouquet, Y. 2013. Nickel isotope
variations in terrestrial silicate rocks and geological reference materials measured
by MC-ICP-MS. Geostandards and Geoanalytical Research, **37**, 297–317.

Hawkins, J. W., and Evans, C. A. 1983. Geology of the Zambales Range, Luzon,
Philippine Islands: Ophiolite derived from an island arc-back arc basin pair. The
Tectonic and Geologic Evolution of Southeast Asian Seas and Islands: Part 2
Geophysical Monograph Series, 95-123.

Hofmann, A., Bekker, A., Dirks, P., Gueguen, B., Rumble, D., and Rouxel, O.J. 2014.
Comparing orthomagmatic and hydrothermal mineralization models for
komatiite-hosted nickel deposits in Zimbabwe using multiple-sulfur iron and
nickel isotope data. Mineralium Deposita, **49**, 75–100.

Holloway, N. 1982. North Palawan block, Philippines: its relation to Asian mainland and
role in evolution of the South China Sea. American Association of Petroleum
Geologists Bullin, **66**, 1355-83.

Huppert, H.E., Sparks, R.S.J., Turner, J.S., and Arndt, N.T. 1984. Emplacement and
cooling of komatiite lavas. Nature, **309**, 19–22.

Keays, R.R. 1995. The role of komatiitic and picritic magmatism and Ssaturation in the formation of ore deposits. Lithos, **34**,1–18.

Kesler, S. E., Simon, A. C., and Simon, A. F. 2015. Mineral resources, economics and the environment. Cambridge University Press.

Larson, P. B., Maher, K., Ramos, F. C., Chang, Z., Gaspar, M., and Meinert, L. D. 2003. Copper isotope ratios in magmatic and hydrothermal ore-forming environments. Chemical Geology, **201**, 337-350.

Lazar, C., Young, E.D., and Manning, C.E. 2012. Experimental determination of equilibrium nickel isotope fractionation between metal and silicate from 500 °C to 950 °C. Geochimica et Cosmochimica Acta, **86**, 276–295.

Lemine, O. M. 2014. Transformation of goethite to hematite nanocrystallines by high energy ball milling. Advances in Materials Science and Engineering, 2014.

Lesher, C. M. 1989. Komatiite-associated nickel sulfide deposits. Reviews in Economic Geology, **4**, 45–101.

Lesher, C. M. 2019. Up, Down, or Sideways: Emplacement of Magmatic Ni-Cu-(PGE) Sulfide Melts in Large Igneous Provinces. Canadian Journal of Earth Sciences.

Lesher, C.M., and Burnham, O.M. 2001. Multicomponent elemental and isotopic mixing in Ni–Cu–(PGE) ores at Kambalda, Western Australia. The Canadian Mineralogist, **39**, 421–446.

Li, M., He, Y. S., Kang, J. T., Yang, X. Y., He, Z. W., Yu, H. M., and Huang, F. 2017. Why was iron lost without significant isotope fractionation during the lateritic process in tropical environments?. Geoderma, **290**, 1-9.

Liu, S. A., Li, D., Li, S., Teng, F. Z., Ke, S., He, Y., and Lu, Y. 2014. High-precision copper and iron isotope analysis of igneous rock standards by MC-ICP-MS. Journal of Analytical Atomic Spectrometry, **29**, 122-133.

Liu, S. A., Teng, F. Z., Li, S., Wei, G. J., Ma, J. L., and Li, D. 2014. Copper and iron isotope fractionation during weathering and pedogenesis: insights from saprolite profiles. Geochimica et Cosmochimica Acta, **146**, 59-75.

Loss, R. D., Rosman, K. J. R., and De Laeter, J. R. 1990. The isotopic composition of zinc, palladium, silver, cadmium, tin, and tellurium in acid-etched residues of the Allende meteorite. Geochimica et Cosmochimica Acta, **54**, 3525-3536

Manceau A., Schlegel M. L., Musso M., Sole V. A., Gauthier C., Petit P. E., and Trolard F. 2000. Crystal chemistry of trace elements in natural and synthetic goethite. Geochimica et Cosmochimica Acta, **64**, 3643–3661.

Maréchal, C. N., Télouk, P., and Albarède, F. 1999. Precise analysis of copper and zinc isotopic compositions by plasma-source mass spectrometry. Chemical Geology, **156**, 251-273.

Markl, G., Lahaye, Y., and Schwinn, G. 2006. Copper isotopes as monitors of redox processes in hydrothermal mineralization. Geochimica et Cosmochimica Acta, **70**, 4215-4228.

Mathur, R., Ruiz, J., Titley, S., Liermann, L., Buss, H., and Brantley, S. 2005. Cu isotopic fractionation in the supergene environment with and without bacteria. Geochimica et Cosmochimica Acta, **69**, 5233-5246.

McDonough, W. F., and Sun, S. S. 1995. The composition of the Earth. Chemical Geology, **120**, 223-253.

Moynier, F., Blichert-Toft, J., Telouk, P., Luck, J. M., and Albarède, F. 2007. Comparative stable isotope geochemistry of Ni, Cu, Zn, and Fe in chondrites and iron meteorites. Geochimica et Cosmochimica Acta, **71,** 4365-4379.

Naldrett, A. J. 2004. Magmatic sulfide deposits: geology, geochemistry, and exploration. Springer, Berlin.

Naldrett, A.J. 1989. Magmatic sulfide deposits. Oxford University Press, Oxford.

Naldrett, A.J., 1979. Partitioning of Fe, Co, Ni, and Cu between sulfide liquid and basaltic melts and the composition of of Ni-Cu sulfide deposits. Economic Geology, **74**, 1520-1528.

Norrish, K. and Hutton, J. T. 1969. An accurate X-ray spectrographic method for the analysis of a wide range of geological samples. Geochimica et Cosmochimica Acta, **33**, 431-453.

Nishiizumi, K., and Caffee, M. W. 2011. Lovina: Is this a Meteorite?. Meteoritics and Planetary Science Supplement, 74.

Ober, J. A. 2018. Mineral commodity summaries 2018. US Geological Survey. 112-113.

Pędziwiatr, A., Kierczak, J., Waroszewski, J., Ratié, G., Quantin, C., and Ponzevera, E., 2018. Rock-type control of Ni, Cr, and Co phytoavailability in ultramafic soils. Plant Soil, **423**, 339–362.

Pelletier, B. 1996. Serpentine in nickel silicate ore from New Caledonia. Nickel'96: Mineral to Market, 197-205.

Petaev, M. I., and Jacobsen, S. B. 2004. Differentiation of metal-rich meteoritic parent bodies: I. Measurements of PGEs, Re, Mo, W, and Au in meteoritic Fe-Ni metal. Meteoritics & Planetary Science, **39**, 1685-1697.

Poitrasson, F., Halliday, A. N., Lee, D. C., Levasseur, S., and Teutsch, N. 2004. Iron isotope differences between Earth, Moon, Mars and Vesta as possible records of contrasted accretion mechanisms. Earth and Planetary Science Letters, **223**, 253-266.

Poitrasson, F., Viers, J., Martin, F., and Braun, J. J. 2008. Limited iron isotope variations in recent lateritic soils from Nsimi, Cameroon: implications for the global Fe geochemical cycle. Chemical Geology, **253**, 54-63.

Raschka, H., Nacario, E., Rammlmair, D., Samonte, C., and Steiner, L. 1985. Geology of the ophiolite of central Palawan Island, Philippines. Ofioliti, **10**, 375–390.

Ratié, G., Jouvin, D., Garnier, J., Rouxel, O., Miska, S., Guimarães, E., Cruz Vieira, L., Sivry, Y., Zelano, I., Montarges-Pelletier, E., Thil, F., and Quantin, C. 2015. Nickel isotope fractionation during tropical weathering of ultramafic rocks. Chemical Geology, **402**, 68-76.

Ratié, G., Quantin, C., De Freitas, A. M., Echevarria, G., Ponzevera, E., and Garnier, J. 2019. The behavior of nickel isotopes at the biogeochemical interface between ultramafic soils and Ni accumulator species. Journal of Geochemical Exploration, **196**, 182-191.

Ratié, G., Quantin, C., Jouvin, D., Calmels, D., Ettler, V., Sivry, Y., Cruz Vieira, L., Ponzevera, E., and Garnier, J. 2016. Nickel isotope fractionation during laterite Ni ore smelting and refining: Implications for tracing the sources of Ni in smelter-affected soils. Applied Geochemistry, **64**, 136-145.

Roskill Information Services 1981. The economics of nickel (3d edition): London, Roskill Information Services, 498.

Rossman, D., Castañada, G., and Bacuta, G. 1989. Geology of the Zambales ophiolite, Luzon, Philippines. Tectonophysics, **168**, 1-22.

Saunders, N. 2018. Nickel stable isotope fractionation in planetary materials (Doctoral dissertation, University of Oxford).

Saunders, N., Barling, J., Halliday, A., Harvey, J., and Fitton, G. (2018) Goldschmidt Abstracts, 2018, 2235.

Schoenberg, R., and von Blanckenburg, F. 2006. Modes of planetary-scale Fe isotope fractionation. Earth and Planetary Science Letters, **252**, 342-359.

Schuessler, J. A., Schoenberg, R., and Sigmarsson, O. 2009. Iron and lithium isotope systematics of the Hekla volcano, Iceland—evidence for Fe isotope fractionation during magma differentiation. Chemical Geology, **258**, 78-91.

Schweller, W.J., Karig, D.E., and Bachman, S.B., 1983. Original setting and emplacement history of the Zambales ophiolite, Luzon, Philippines, from stratigraphic evidence. In: D. Hayes (Editor), The Tectonics and Geologic Evolution of Southeast Asian Seas and Islands, Part 2. Washington DC American Geophysical Union Geophysical Monograph Series, **27**, 124-136.

Sherman, D. M. 2013. Equilibrium isotopic fractionation of copper during oxidation/reduction, aqueous complexation and ore-forming processes: Predictions from hybrid density functional theory. Geochimica et Cosmochimica Acta, **118**, 85-97.

Shields, W. R., Murphy, T. J., and Garner, E. L. 1964. Absolute isotopic abundance ratio and the atomic weight of a reference sample of copper. Journal of Research of the National Bureau of Standards, **68**, 589–592.

Šillerová, H., Chrastný, V., Vítková, M., Francová, A., Jehlička, J., Gutsch, M.R., Kocourková, J., Aspholm, P.E., Nilsson, L.O., Berglen, T.F., and Jensen, H.K., 2017. Stable isotope tracing of Ni and Cu pollution in North-East Norway: Potentials and drawbacks. Environmental Pollution, **228**, 149-157.

Smythe, D.J., Wood, B.J., and Kiseeva, E.S. 2017. The S content of silicate melts at sulfide saturation: new experiments and a model incorporating the effects of sulfide composition. American Mineralogist, **102**, 795–803.

Snyder, R.L., and Hubbard, C.R. 1988. RIR - measurement and use in quantitative XRD. Powder Diffraction, **3**, 74-77

Spivak-Birndorf, L. J., Wang, S. J., Bish, D. L., and Wasylenki, L. E. 2018. Nickel isotope fractionation during continental weathering. Chemical Geology, **476**, 316-326.

Staudacher, T., and Allègre, C. J. 1990. The origin of josephinites: a new noble gas study. Earth and Planetary Science Letters, **98**, 380-389.

Steele, R. C., Coath, C. D., Regelous, M., Russell, S., and Elliott, T. 2012. Neutron-poor nickel isotope anomalies in meteorites. The Astrophysical Journal, **758**, 59.

Steele, R.C.J., Elliott, T., Coath, C.D., and Regelous, M. 2011. Confirmation of mass-independent Ni isotopic variability in iron meteorites. Geochimica et Cosmochimica Acta, **75**, 7906–7925.

Teplyakova, S. N. 2011. Evolution of molten material in iron cores of small planets. Solar System Research, **45**, 515-522.

Thompson, A., Ruiz, J., Chadwick, O.A., Titus, M., and Chorover, J., 2007. Rayleigh fractionation of iron isotopes during pedogenesis along a climate sequence of Hawaiian basalt. Chemical Geology, **238**, 72–83.

US Geological Survey. 2019. Mineral Commodity Summaries, 2019. Government Printing Office.

Vance, D., Archer, C., Bermin, J., Perkins, J., Statham, P. J., Lohan, M. C., Ellwood, M. J., and Mills, R. A. 2008. The copper isotope geochemistry of rivers and the oceans. Earth and Planetary Science Letters, **274**, 204-213.

Ventura, G. T., Gall, L., Siebert, C., Prytulak, J., Szatmari, P., Hürlimann, M., and Halliday, A. N. 2015. The stable isotope composition of vanadium, nickel, and molybdenum in crude oils. Applied Geochemistry, **59**, 104-117.

Wasylenki, L.E., Howe, H.D., Spivak-Birndorf, L., and Bish, D.L. 2015. Ni isotope fractionation during sorption to ferrihydrite: implications for Ni in banded iron formations. Chemical Geology, **400**, 56–64.

Weyer, S., Anbar, A. D., Brey, G. P., Münker, C., Mezger, K., and Woodland, A. B. 2005. Iron isotope fractionation during planetary differentiation. Earth and Planetary Science Letters, **240**, 251-264.

Wiederhold, J.G., Teutsch, N., Kraemer, S.M., Halliday, A.N., and Kretzschmar, R. 2007. Iron isotope fractionation in oxic soils bymineral weathering and podzolization. Geochimica et Cosmochimica Acta, **71**, 5821–5833.

Wiederhold, J.G., Teutsch, N., Kraemer, S.M., Halliday, A.N., and Kretzschmar, R. 2007. Iron isotope fractionation during pedogenesis in redoximorphic soils. Soil Science Society of America Journal, **71**, 1840–1850.

Yamaguchi, K. E., Johnson, C. M., Beard, B. L., Beukes, N. J., Gutzmer, J., and Ohmoto, H. 2007. Isotopic evidence for iron mobilization during Paleoproterozoic lateritization of the Hekpoort paleosol profile from Gaborone, Botswana. Earth and Planetary Science Letters, **256**, 577-587.

Yesavage, T., Fantle, M. S., Vervoort, J., Mathur, R., Jin, L., Liermann, L. J., and Brantley, S. L. 2012. Fe cycling in the Shale Hills Critical Zone Observatory, Pennsylvania: an analysis of biogeochemical weathering and Fe isotope fractionation. Geochimica et Cosmochimica Acta, **99**, 18-38.

Yumul, G. P., Dimalanta, C. B., and Tamayo, R. A. 2005. Indenter-tectonics in the Philippines: Example from the Palawan Microcontinental Block-Philippine Mobile Belt Collision. Resource Geology, **55**, 189-198.

Yumul, G. P., Dimalanta, C. B., Marquez, E. J., and Queaño, K. L. 2009. Onland signatures of the Palawan microcontinental block and Philippine mobile belt collision and crustal growth process: A review. Journal of Asian Earth Sciences, **34**, 610-623.

Yumul, G., and Dimalanta, C. 1997. Geology of the Southern Zambales Ophiolite Complex, (Philippines): juxtaposed terranes of diverse origin. Journal of Asian Earth Sciences, **15**, 413-421.

Zhou, M., Yumul, G. P., Malpas, J., and Sun, M. 2000. Comparative study of platinum-group elements in the Coto and Acoje blocks of the Zambales Ophiolite Complex, Philippines. Island Arc, **9**, 556-564.

Zhu, X. K., O'Nions, R. K., Guo, Y., Belshaw, N. S., and Rickard, D. 2000.
Determination of natural Cu-isotope variation by plasma-source mass
spectrometry: implications for use as geochemical tracers. Chemical Geology,
163, 139-149.

Curriculum Vitae

Name:	Congxi Zhu
Post-secondary Education and Degrees:	University of Waterloo Waterloo, Ontario, Canada 2015-2017 B.Sc. The University of Western Ontario London, Ontario, Canada 2017-2019 M.Sc.
Honours and Awards:	Dean's Honour List 2017
Related Work Experience	Teaching Assistant The University of Western Ontario 2017-2019 Research Assistant The University of Western Ontario 2017-2019